Comparison of Energy Storage Technologies for applications of Unmanned Electrical Aerial Vehicles

INEGI

André Filipe Rosário de Brito Lhamas

Relatório do Projecto Final / Dissertação do MIEM

Orientador no INEGI: Dr. Nuno Correia; Eng. João Barbosa

Orientador na FEUP: Prof. Dr. António Torres Marques

Faculdade de Engenharia da Universidade do Porto

Mestrado Integrado em Engenharia Mecânica

Julho 2013

Aos meus Pais.

Comparação de tecnologias de armazenamento de energia para aplicações de veículos aéreos não tripulados eléctricos (UEAV)

Resumo

O trabalho relatado nesta dissertação visou projectar a redução de massa numa célula de combustível de membrana de permuta iónica (PEM FC) através do uso de materiais compósitos nas placas terminais (end plates), como alternativa ao metal. Uma vez que as placas de terminais, assim como outros componentes de fixação, representam uma fracção significativa da massa global do sistema, esta redução resulta numa maior potência e energia específicas, podendo possivelmente tornar os sistemas PEM FC mais interessantes em aplicações onde o peso se apresenta como um factor crítico. Além da redução de massa, é também discutida a deformação na placa. Foi demonstrado na literatura que grandes deformações nas placas de terminais podem levar a influências negativas no desempenho da célula de combustível. Esta dissertação perspectiva soluções construtivas alternativas que são capazes de reduzir significativamente o peso, assim como alcançar valores de deformação mais baixos do que as placas de fim metálicas, aumentando assim a eficiência global do sistema.

O sistema de célula de combustível foi estudado para o caso de uma aeronave com 210 kg de peso máximo de descolagem (MTOW), possuindo um requisito de cerca de 20 kW de potência máxima. Neste caso, a massa disponível para o sistema propulsivo foi de 70 kg.

Através do uso de uma análise por elementos finitos, o conceito com o melhor desempenho entre os conceitos sugeridos foi seleccionado. Posteriormente, foram realizados cálculos com vista à determinação da energia específica do sistema resultante. Dessa forma, tornou-se possível uma comparação com os conceitos de placas de fim actualmente usados. Além disso, foi também efectuada a comparação dos sistemas referidos com um sistema propulsivo convencional, compreendendo um motor de combustão interna (ICE).

O novo conceito de placa de fim permitiu um aumento significativo na energia específica (28,3%), ainda que tenha sido também provado a incapacidade actual de as células de combustível igualarem sistemas ICE convencionais, mesmo que, tal como é demonstrado, ter também provado que existe espaço amplo para melhoria.

Abstract

The work reported by this dissertation aimed to engineer a reduction in mass in a proton exchange membrane fuel cell (PEM FC) by using composite materials as an alternative to metals in the end plate. Since end plates, along with other fixation components, account for a significant fraction of the global system weight, this reduction results in increased specific power and specific energy, possibly making PEM FC systems more interesting in applications where weight is critical. Besides mass reduction, plate deformation is discussed. Large strains in the end plate have been shown to negatively influence fuel cell performance. This dissertation reports insights into alternative construction solutions that are able to significantly reduce weight, as well as achieve lower strain values than metal end plates, increasing overall system efficiency.

The fuel cell system was studied for the case of a 210 kg maximum take-off weight (MTOW) airplane with a maximum power requirement of c. 20kW for take-off. In this case the available mass for the propulsive system was 70 kg.

Through the use of a finite element analysis, the best performing amongst the suggested concepts was selected. Thereafter, calculations for determining specific energy of the resulting system were accomplished, making a comparison with the currently used end plate concepts possible, as well as a comparison with a conventional propulsive system, comprising an internal combustion engine (ICE).

The new endplate concept allowed a significant increase in specific energy (28,3%), albeit also proving that fuel cells are not yet capable of matching conventional ICE systems, even if, as is shown, there is ample room for improvement.

Agradecimentos

Agradeço ao meu Orientador Professor Doutor António Torres Marques toda a disponibilidade, assistência e sugestões ao longo do projecto. Além disso, agradeço a sua promoção de contactos que teve resultados muito positivos para o trabalho.

Agradeço ao meu Orientador Doutor Nuno Correia toda a disponibilidade, amizade e apoio demonstrados no decorrer do trabalho, apesar das exigências da sua profissão. De referir que, muitas das sugestões conceptuais presentes neste trabalho foram sua sugestão, sendo que lhe fico por isso muito grato.

Agradeço ao meu Orientador Engenheiro João Barbosa por toda a disponibilidade, companheirismo, e ânimo dado no decorrer da dissertação, assim como por me ter amavelmente mostrado a componente prática de construção aeronáutica.

Agradeço toda a orientação dada pelo Professor Doutor José Esteves e pela sua total disponibilidade na resolução das mais diversas dúvidas que lhe fui apresentando.

Agradeço ao Doutor António Melro e ao Engenheiro José Cerqueira do INEGI pelo esclarecimento de dúvidas e sugestões dadas.

Agradeço ao Cristiano as largas horas que passou comigo a resolver problemas críticos no software Abaqus, assim como todas as cruciais sugestões que fez. Agradeço-lhe também o seu companheirismo e boa disposição no decorrer do meu estágio no INEGI.

Um enorme obrigado à minha família e amigos, pela motivação ao longo de todo este percurso académico.

Agradeço aos meus colegas da FEUP e do INEGI toda a amizade e bons momentos vividos no decorrer deste semestre.

Um obrigado a todos aqueles que de alguma forma contribuíram para a realização deste estudo.

Table of Contents

Table of Figures

Table of Tables

List of Acronyms

AFC	Alkaline Fuel Cell
AUV	Autonomous Underwater Vehicle
BoP	Balance of Plant
CFRP	Carbon Fibre Reinforced Polymer
CHP	Combined Heat and Power
CVT	Continuously Variable Transmission
DMFC	Direct Methanol Fuel Cell
DOE	Department of Energy
EM	Electric Motor
EP	End Plate
FC	Fuel Cell
FW	Filament Winding
GDL	Gas Diffusion Layer
GFRP	Glass Fibre Reinforced Polymer
ICE	Internal Combustion Engine
IST	Instituto Superior Técnico
LAETA	Laboratório Associado para Energia, Transportes e Aeronáutica
MCFC	Molten Carbonate Fuel Cell
MEA	Membrane Electrode Assembly
MTOW	Maximum Take-off Weight
NATO	North Atlantic Treaty Organization
PAFC	Phosphoric Acid Fuel Cell
PEM	Proton Exchange Membrane
PM	Proton Motor
PV	Photovoltaic
RTM	Resin Transfer Moulding
SOFC	Solid Oxide Fuel Cell
UAV	Unmanned Aerial Vehicle
UAS	Unmanned Aerial System
UBI	Universidade da Beira Interior
UV	Unmanned Vehicle

1. Introduction

1.1 INEGI

INEGI was originally formed by the Department of Mechanical Engineering of the Faculty of Engineering of the University of Porto (FEUP) in 1986 and it still holds that connection to the departments of Mechanical Engineering and of Industrial Engineering and Management that constitute its strongest links to scientific and technical knowledge and training and expertise. In its 26 year existence INEGI developed and consolidated a strong partnership with the Industry in Research, Development and Innovation (R&D+I) projects. Today INEGI's R&D+I projects under contract with the Industry account for more than 60% of its turnover.

As a private non-profit association and a public service entity (*Entidade de Utilidade Pública*) INEGI is positioned as an agent with responsibilities for the development of the Economy and Society contributing towards the development and consolidation of a competitive model based on knowledge and technological density in-and-of products, processes and technological based innovation. Currently the Institute has 62 Associated Institutions that represent all spheres of activity from the University of Porto to Industrial Associations in relevant fields of INEGI's activity as well as Private Companies and Public Institutions.

INEGI is governed by a board which is formed by three representatives from private industrial associates and two representatives from the University of Porto thereby ensuring its positioning as an institution oriented towards the economic and social valorisation of R&D results, knowledge and technology. The Board reports to the General Assembly of the Private and Public Associates.

INEGI's organizational structure relies on around three pillars of activity in different technology readiness levels, maintaining a strong competence matrix element:

- Research
- Innovation and Technology Transfer (ITT)
- Consulting and Services

At its base, INEGI's structure is formed by different scientifically and technologically specialized Units which support research activity, ITT and consulting. Most significantly ITT and Consulting are especially directed towards the development of solutions for private companies. This organizational structure is specialized in the development and innovation projects of high technological complexity that require the integration of multidisciplinary knowledge and competences.

INEGI is part of a Research Unit of the Associated Laboratory for Energy, Transportation and Aeronautics (LAETA), which also counts as members the Mechanical Engineering Institute – IST, the Mechanical Engineering Institute - FEUP, the Centre for Aerospace Sciences – IST,

the Industrial Aerodynamics Institute at the University of Coimbra and the Aeronautics and Astronautics Research Center of the University of Beira Interior.

INEGI owns a diverse set of facilities and equipment in order to support its activity, namely laboratories (some of which are accredited laboratories), experimental and development laboratories (capable of producing components and pre-series) and an extensive engineering software catalogue. Software available at INEGI ranges from CAD (including CATIA), FEM (including ABAQUS), CAM, casting simulation, sheet metal forming, as well as other tools that support INEGI's work on Wind Energy consulting, such as WAsP and WindFarmer for atmospheric studies and GIS (ArcGis).

INEGI's staff is composed of 170 people, 80% of whom are graduates or post-graduates. This number is complemented with *c.* 50 academic researchers from the Faculty of Engineering of the University of Porto.

1.2 The Electric Long Endurance UAV Project and the NATO Unmanned Vehicle Study Group

This dissertation was carried out in the context of an internship that took place at INEGI, within the scope of the "Electric Long Endurance Unmanned Aerial Vehicle (ELE-UAV)" project jointly proposed by IST, UBI and INEGI teams of Laboratório Associado para a Energia, Transportes e Aeronáutica (LAETA) for the development of a small sized aircraft intended for civilian applications.

The multidisciplinary project aims to put together the special skills of each participating member in a broad range of fields of study concerning subjects such as Aerodynamics, Propulsion, Mechanical Project, Structures & Materials, Non-Destructive Inspection, Aerodynamic Project, Optimization, Avionics, Aerial Control and Transportation, among others. Those areas are expected to experience sustained development, so that a sharing network of research, skills, and knowledge can be created within the LAETA.

The sharing of knowledge and technical expertise is expected to enable scientific research, within its own specific time and budget limitations, as well as solving of actual practical problems that come up during its implementation.

Furthermore, INEGI is currently participating in a NATO study group for the implementation of fuel cell systems in Unmanned Vehicles (UVs), being that INEGI is solely focused on the Unmanned Aerial Vehicles (UAV) part. This dissertation also contributed to solving problems in the on-going work of that study group.

The initial objectives of this project were to provide with a State-of-the-Art gathering of electrical propulsive technologies for high endurance, followed by a proper analysis and comparison of each, as well as a practical assignment of physically collaboration in the multidisciplinary construction of the aforementioned aircraft.

1.3 Report Organization and Dissertation Objectives

1.3.1 Report Organization

Chapter 1 provides with an introduction to the work, along with the initial general objectives for the dissertation.

Chapter 2 states and compares possible propulsive systems that can be implemented in a UAV, starting with a modelling/comparison of the efficiencies of different Conversion Processes, with a special focus on fuel cell systems.

Chapter 3 provides a description of the path taken to conceptual development, explaining the motivation behind every concept that came up, along with the necessary assumptions made.

Chapter 4 contains all of the necessary information regarding the construction of the numerical modelling, and the achieved results.

Chapter 5 includes a discussion of the numerical model results, and provides with the necessary calculations to specific energy of each system, so as to provide a comparison between them.

Lastly, an analysis and comment of the preceding chapters, along with the conclusions to the project are made in chapter 6. Furthermore, a suggestion of possible future studies and work, that are required if *de facto* implementation of the suggested concepts is eventually intended. Furthermore, a suggestion of an alternative approach to stack fixations is also included.

The final annexes of this report include the references of the consulted and cited sources, as well as attachments.

1.3.2 Dissertation Objectives

Unmanned aerial vehicles/systems are aircrafts without the presence of a human pilot. The aircraft is controlled either remotely by a pilot on the ground or autonomously through a computerized system. The absence of human presence, with its inherent flexibility (physiological limitations), allows this type of aircraft systems to perform missions ranging from dull to life threatening scenarios, in fact, they are commonly categorized as "dull, dirty and dangerous", [1]. Furthermore, the inexistence of life-support systems and the possibility of being built on a smaller scale lead to decreased construction and operational cost, as well as lower fuel consumption.

The working principle of a fuel cell was discovered back in the 19th Century; however they have only recently been the target of significant research and development, and interest of energy consuming devices manufacturers. Its working principle, although extremely complex, can be very basically explained as the inverse principle of the water electrolysis. Being a non-pollutant (depending on FC type and manner to which fuel is obtained), and noiseless power source makes them particularly attractive in some applications, and such is the case of unmanned aerial vehicles. This report will focus on polymer electrolyte membrane (PEM), also known as proton exchange membrane fuel cells. PEM FC have gathered significant attention due to advantages such as low-temperature operation, rapid start-up and high power density, which makes them particularly applicable to transportation systems, [2].

Composite fibre reinforced materials are nowadays widely used in a broad range of applications, in particular in the aeronautical and defence industries. Their high specific

strength and stiffness, along with the possibility of providing the required mechanical properties in the necessary directions, taking into account the predicted loads beforehand, poses as an edge over other more conventional materials, and has led to increased usage in the past years. Another important characteristic is their ability of improving chemical resistance according to the working environment, leading to high chemical attack strength.

This dissertation was first set out to be an analysis of the possible propulsive systems of an UAV. A state of the art gathering of the possible propulsion systems for an unmanned aerial vehicle was accomplished, with a special focus to fuel cell systems. Yet, the objective of the dissertation changed and focused itself on an important matter regarding fuel cell viability in UAVs.

This paper intends to demonstrate a way to introduce a fuel cell system in a UAV as a feasible and viable propulsion system. Not considering cost, the greatest limitation that a FC system faces in its introduction in aerial vehicles is perhaps its Specific Energy (Wh/kg). If significant and sufficient mass reduction were to be achieved, then its specific power and energy would be increased, along with an edge over other propulsive systems.

The End Plates, along with the necessary fixation components (screws, bolts, etc.), account for a considerable part (36%, according to [3]) in the total system weight. Commonly used materials for end plates are steel ($mass\ density, \rho = 7800\ kg/m^3$) and aluminium ($\rho = 2700\ kg/m^3$). This paper proposes an overall system weight reduction through the replacement with Composite Materials, in particular Carbon Fibre Reinforced Polymer (CFRP) ($\rho = 1600\ kg/m^3$).

Another challenge that is intended to be resolved through this suggested material replacement is End Plate deformation. A High Modulus CFRP with high stiffness properties is expected to have smaller deflection in the End Plate, and consequently smaller deflection in the Bipolar Plate, even leading to possible lesser mass requirement in the Bipolar Plate and subsequent potential increase in fuel cell reliability. It has been shown that Plate deformation, and a consequent non-uniform pressure over the Bipolar Plates, leads to decreased system performance, [2],[4]. It is therefore possible to say that higher specific power and energy can be directly or indirectly achieved if the End Plate can provide lesser deflection. Several articles [5], [6], [7] suggest the introduction of lighter materials in the bipolar plates is bound to occur. If that turns out to be true in the future, than the End Plates, along with the required fixation components will also be expected to have a bigger part in the total system weight, making a mass reduction in the End Plate increasingly more interesting.

From the outcome combination of the stress-strain uniform state, along with decrease in overall system mass, the determination of the specific energy of the FC system prior and after the implemented changes will be performed. As means of comparison, the difference between the two will be the achieved gain in specific energy and contained available energy. Furthermore, that gain in specific energy will also be compared with a conventional internal combustion engine (ICE) system, in order to ascertain the viability of the fuel cell when compared with currently used systems.

2. Literature review

This section is an extended summary containing all the gathered information from several reliable sources throughout the work period, as well as the required skills and tools to the accomplishment of the proposed goal. It poses as an essential part to the dissertation, for not only it would not have been possible to have accomplished the proposed work, but also because it stands as a state-of-the-art gathering of several important matters regarding UAV propulsion, which can hopefully prove its usefulness in the future.

As stated before, the objectives for this dissertation have changed considerably throughout the work period. Study over very interesting and relevant fields of study to the UAV propulsive system, such as Photovoltaic Cells, Kinetic Energy Systems and Basic Aeronautics, was carried out, however they were not found suitable regarding this dissertation's ultimate objective. For that matter, they are not present in this section. However, they can be found as annexes in the hindmost pages of this report (see Annexe E).

2.1 Introduction to Conversion Processes

According to John H. Scott [8], there are fundamentally two means of modelling the conversion of chemical bond energy into electricity: the Carnot theory (based on heat engine conversion analogies) and electrochemistry (related to direct chemical-electrical conversion) see Figure 1.

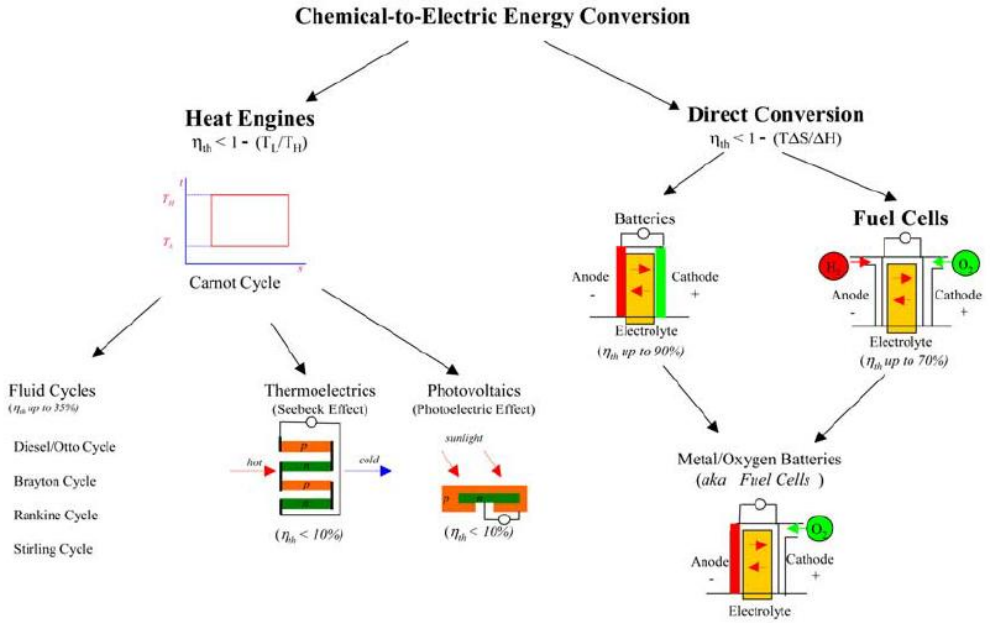

Figure 1: Chemical-to-electric energy conversion. Heat engine conversion and direct conversion have fundamentally different ideal limits on thermodynamic efficiency, [8]

2.1.1 Heat Conversion

Heat conversion engines based on fluid cycles are currently the most commonly used [8]. Their working principle comprises four stages in which the working: is compressed, heated through chemical reaction, and expanded (whereby one obtains mechanical work), and finally cooled.

The formalization of a model for this idealized heat engine was proposed by Carnot in the Carnot cycle, see Figure 2. This model allows the understanding of how the laws of thermodynamics limit the idealized maximum efficiency of a heat engine through a relation between the temperature at which heat is added to the system, the "topping" temperature, T_H, and the temperature at which waste heat is rejected from the system, the "bottoming" temperature, T_L.

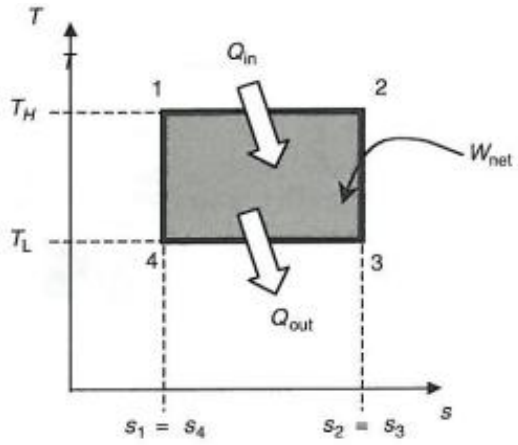

Figure 2: The Carnot cycle shown on a T-s diagram, [9]

The actual efficiencies with practical heat engines are, however, much lower than that of an ideal Carnot cycle operating between the same T_H and T_L. This is due to the fact that the construction of engines with isothermal processes at the topping and bottoming temperatures is impractical because it is impossible to build a thermodynamically reversible engine, i.e., a system without the production of entropy (dissipation of energy).

In order to overcome these difficulties, the following fluid cycle heat engines are commonly in use, with examples of operation in brackets:

- The Diesel/Otto cycle (e.g., the automotive internal combustion);
- The Brayton cycle (e.g., jet engines and gas turbines);
- The Rankine cycle (e.g., reciprocating steam engines and steam turbines);
- The Stirling cycle (e.g., currently used in small high-efficiency refrigerators).

The thermoelectrical and photovoltaic energy conversion systems, characterized by their relatively low efficiencies, can also see their efficiency modelled through the Carnot theory.

The thermoelectric conversion based on the Seebeck effect, comprises the direct conversion of differences in temperature to electric voltage and vice-versa and without the presence of any moving parts. The Electromotive Force (EMF) of a thermocouple is defined by the theory of thermoelectricity as the difference in the absolute thermoelectric power, S, between two metals or alloys that constitute the thermocouple. The temperature gradient throughout the two arms, consisting of two metals, A and B, of the thermocouple results in the generation of voltage, ΔU, and is calculated through the integration limits of temperature at junction 1, T_1, and at junction 2, T_2, as in Equation 2.1.

$$\Delta U = \int_{x_1}^{x_2} (S_A - S_B) \nabla T \, dx = \int_{T_1}^{T_2} (S_A - S_B) \, dT \qquad \text{Equation 2.1}$$

Where S_A and S_B are the thermoelectric power of metals A and B, respectively.

There is no general equation for absolute thermoelectric power of a metal. Since copper and lead have plenty and accurate experimental data, these two metals are reference materials in thermoelectricity. As seen in Figure 3, the thermoelectric power for both metals is negative at low temperatures, beneath $50K$. That of lead, however, remains negative over the whole temperature range.

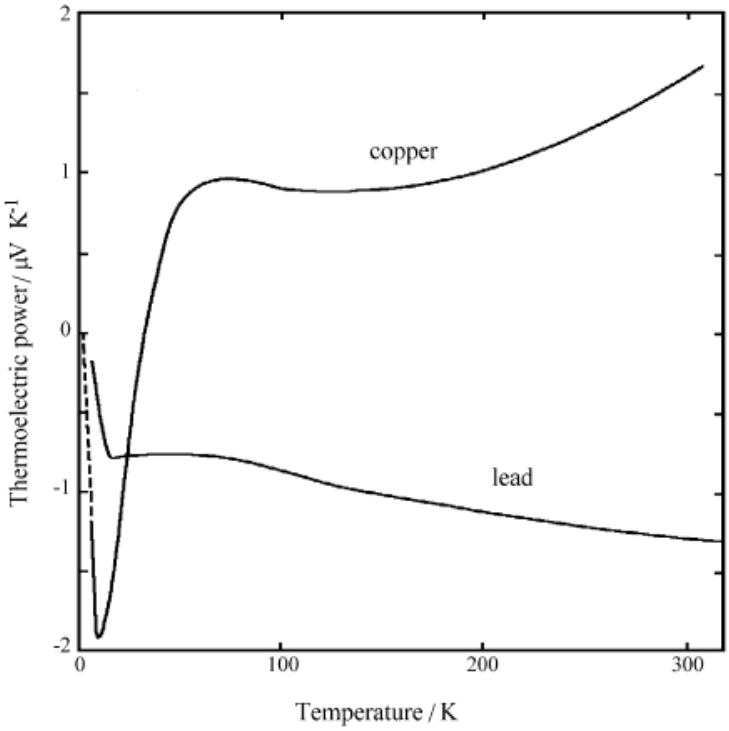

Figure 3: Low-temperature absolute thermoelectric power for copper and lead, [10]

For practical industrial applications, however, alloys are used as thermocouples rather than pure metals. Figure 4 shows the absolute thermoelectric power for some alloys (chromel and alumel) and pure metals (platinum and copper) that are commonly used in thermocouples in different combinations and with other metals and alloys, being platinum the third reference material in thermoelectricity. Also, since thermoelectric power for platinum and alumel is negative, their curves are shown as $-S(T)$.

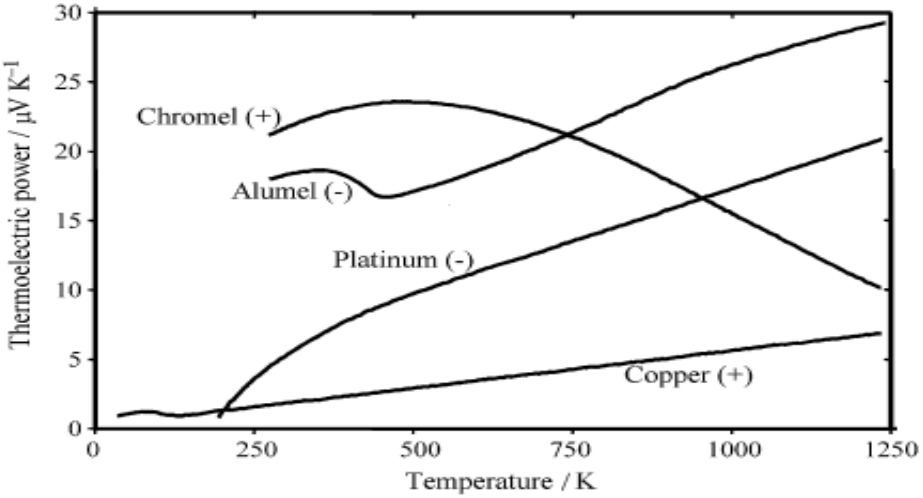

Figure 4: High-temperature absolute thermoelectric power for copper, platinum, chromel and alumel, [10]

As for the photovoltaic conversion, it is a technology that has experienced a fast development and growing usage over the past few years and has proven to be a practical and viable method for conversion of the solar electromagnetic energy to electricity. Even though this type of conversion cannot be strictly considered a heat engine, its efficiency can be modelled using

the Carnot theory, which will not be addressed in this report. Further discussion over this technology is available in the annexes (see Annexe E).

2.1.2 Direct Conversion

Direct conversion systems are based on the direct conversion of chemical energy to electrical energy. These energy conversion systems cannot see their efficiency modelled through the Carnot theory, since they do not comprise the step of heat release previously seen for Heat conversion engines.

As seen from Figure 1, these systems are categorized into batteries and fuel cells. The principle of operation of batteries, the most common and widely used direct conversion system, is based upon the oxidation/reduction reactions that take place within the device which leads to the degradation of the electrodes. They can be further divided into primary and secondary. In the first, the electrodes are consumed irreversibly, making them discarded after use. In the latter, however, the electrode materials are regenerated during recharging. It is possible to make infinite combinations of fuel and oxidants as electrode material for battery. The total available energy for both kinds of batteries is, therefore, proportional to the amount of electrode material contained in the device.

The electrodes in Fuel cell systems are, however, not consumed. Instead they provide the site in which the chemical reactions between fuel, oxidant and transported ions, driven by catalysers, will take place as long as the reacting chemicals, i.e., fuels and oxidants, are fed. The total energy available in a fuel cell system is related to the amount of reactant stored in such a system, a feature than can be compared to an Internal Combustion Engine (ICE).

2.2 Efficiencies of Conversion Processes

2.2.1 Heat Engines and the Carnot Cycle efficiency limitation

As previously mentioned, a heat engine is defined by the four requirements below. It should be noted that, although it is possible to model the efficiency of the Photovoltaic and Seebeck effects through the Carnot Theory, they are not considered heat engines.

1. Receives heat from a high-temperature source (e.g., coal furnace, nuclear reactor);
2. Converts part of this heat to work (e.g., by a turbine);
3. Rejects the remaining waste heat to a low-temperature sink (e.g., atmosphere, river);
4. Operates on a thermodynamic cycle.

Some heat engines do not follow the requirement of operating on a thermodynamic cycle. Such is the example of internal combustion engines and gas turbines, for instance, since the employed working fluid is continuously replaced, the resulting combustion gases are exhausted and the input of new volume of air takes place to prepare the following cycle. The steam power plant however follows perfectly the mentioned requirements, since it receives heat from an external combustion chamber, extracts work through a turbine and rejects the heat to a condenser.

Since for a cyclic process, the initial and final states are identical, the First Law relation involves only the heat input and work output terms, as in Equation 2.2.

$$Q - W = \Delta E = 0 \qquad \text{Equation 2.2}$$

Thusly, one can conclude that the net work performed by the system equals the net heat flow that enters it, see Equation 2.3.

$$W = Q \qquad \text{Equation 2.3}$$

Since at least two thermal reservoirs are involved in the cycle of a heat engine, with heat entering the system from the high-temperature reservoir and heat exiting the system to the low-temperature reservoir, one can define that the net work, W_{net}, in Equation 2.4 is the difference between the heat input, Q_{in}, and heat output,Q_{out}, of the system.

$$W_{net} = Q_{in} - Q_{out} \qquad \text{Equation 2.4}$$

The thermal efficiency, η_{th}, of a heat engine is determined by the amount of work converted from the amount of energy input into the system, as in Equation 2.5.

$$\eta_{th} = \frac{W_{net}}{Q_{in}} \qquad \text{Equation 2.5}$$

Combining Equation 2.4 and Equation 2.5, one can reach the following conclusion regarding thermal efficiency, as in Equation 2.6.

$$\eta_{th} = \frac{W_{net}}{Q_{in}} = \frac{Q_{in} - Q_{out}}{Q_{in}} = 1 - \frac{Q_{out}}{Q_{in}} \qquad \text{Equation 2.6}$$

The conclusion drawn from the previous equation is that the smaller the ratio between the heat output and the heat input, the higher the efficiency.

The Carnot cycle involves four reversible processes, as depicted in Figure 5 with a piston in a cylinder. The idealized cycle of Carnot deemed all the processes to be conducted in a

reversible manner, since that would be the way to achieve the maximum possible work in a heat engine.

The four stages of the reversible Carnot cycle:

- (1-2): isothermal expansion
- (2-3): adiabatic expansion
- (3-4): isothermal compression
- (4-1): adiabatic compression

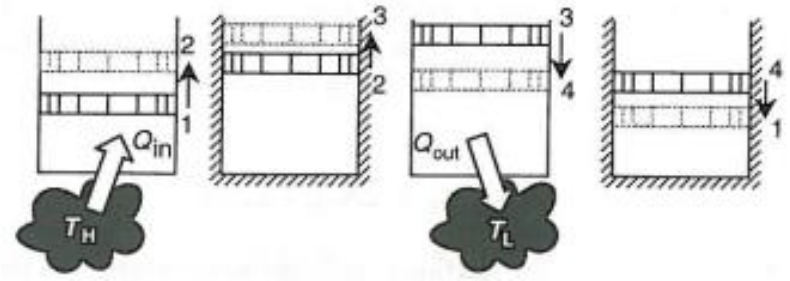

Figure 5: The four stages of the reversible Carnot cycle, [9]

Since heat addition and heat rejection are performed reversibly and isothermally, and considering Equation 2.7, Equation 2.8 can be used to determine the efficiency of the cycle.

$$\Delta S = \frac{Q}{T} \qquad \text{Equation 2.7}$$

$$Q_{rev} = T_0 \Delta S \qquad \text{Equation 2.8}$$

Equation 2.9 is the heat addition step (1-2), and Equation 2.10 is the heat rejection step (3-4).

$$Q_{in} = {}_1Q_2 = T_H(S_2 - S_1) \qquad \text{Equation 2.9}$$

$$Q_{out} = -{}_3Q_4 = T_L(S_3 - S_4) \qquad \text{Equation 2.10}$$

One observes from Figure 2 that during the reversible adiabatic processes, steps (2-3) and (4-1), the entropy remains the same. The shaded area in the figure representing the net work, W_{net}, is shown to be the difference between the heat input, Q_{in}, and the heat output, Q_{out}.

Since the entropy terms in Equation 2.9 and Equation 2.10 are identical, i.e.:

$$S_2 - S_1 = S_3 - S_4 \qquad \text{Equation 2.11}$$

Equation 2.12 is the result of the substitution of Equation 2.11 into Equation 2.6, the thermal efficiency of the Carnot cycle and the maximum possible conversion efficiency for any heat engine, since all of the processes are reversible.

$$\eta_{th,\ Carnot} = 1 - \frac{T_L}{T_H} \qquad \text{Equation 2.12}$$

It is then determined that the maximum thermal efficiency of a thermodynamically reversible heat engine depends upon the ratio of low (T_L) and high (T_H) temperatures in the thermodynamic cycle. Since the low temperature is usually fixed (ambient temperature), the efficiency is determined by the highest temperature in the cycle: the higher the temperature, the higher the efficiency.

2.2.2 Conversion efficiency of Direct Conversion systems

The efficiency of a Fuel cell can be determined according to two definitions. The first, based on the First Law of Thermodynamics, can be used as ground of comparison with thermal heat engines. Like in the previously demonstrated Carnot efficiency, it compares the work produced by the cell with the fuel's heating value.

The second, based on the Second Law of Thermodynamics, compares the cell's actual performance with the maximum work it could develop. To make an analogy with Heat engines, it would be as comparing the actual work of the engine with its Carnot efficiency.

First Law Efficiency

In an electrochemical cell, the system operates at constant temperature (isothermal process), i.e., the products of the reaction leave at the same temperature as the reactants, assuring that more of the chemical energy of the reactants is converted to electrical energy, instead of being consumed to raise the temperature of the products. Since the process is isothermal, the Carnot efficiency cannot be applied. Instead, the maximum work for an electrochemical cell, $W_{max,cell}$, is equal to the change in the Gibbs function (or Gibbs energy), ΔG, between products and reactants (see Equation 2.13).

$$W_{max,cell} = -\Delta G \qquad \text{Equation 2.13}$$

In this case, the work is performed by the movement of electrons through a difference in electrical potential, W_{cell}, and is related to the charge, $n_e F$, of the electrons moving through a potential difference, E, resulting in Equation 2.14.

$$W_{cell} = n_e F E \qquad \text{Equation 2.14}$$

In the previous equation, n_e is the number of electrons transferred per mole of fuel and F is the charge carried by a mole of electrons, which is Faraday's number ($96{,}485\ C \cdot mole^{-1}$).

The First Law efficiency, i.e., the maximum thermal efficiency of an electrochemical cell is, as in heat engines, a ratio relating the net work of the system, yet the heat input, Q_{in}, is substituted for the higher heating value (HHV), resulting in Equation 2.15.

$$\eta_{first\ law} = \eta_{th,cell,max} = \frac{W_{cell}}{HHV} = \frac{n_e F E}{HHV} \qquad \text{Equation 2.15}$$

It is in the equilibrium condition in which no current is being drawn from the cell, the open circuit voltage, $E°$, that the maximum thermal efficiency of an electrochemical cell is obtained. For a hydrogen-oxygen fuel cell, the value of the open-circuit voltage, at 25°C and 1 atm, equals $E° = 1{,}23\ V$ (this value can be determined by relating Equation 2.13 and Equation 2.14 and by using the tabulated Gibbs energy data). Substituting the value of $E°$ results in the maximum thermal efficiency for the previously mentioned conditions (see Equation 2.16).

$$\eta_{th} = \frac{2 \times 96{,}485 \times 1{,}23}{285{,}840} = 0{,}83 \qquad \text{Equation 2.16}$$

The inefficiency's cause is related to the entropy generated from the chemical reactions.

Taking into account an ambient temperature of 25℃, the value of the high temperature in the Carnot cycle would have to be 1480℃ to match the 83% efficiency of Equation 2.16, as demonstrated in Equation 2.17:

$$\eta_{th,\ Carnot} = 1 - \frac{25 + 273{,}15}{T_H + 273{,}15} = 0{,}83 \Leftrightarrow T_H = 1480{,}7℃ \qquad \text{Equation 2.17}$$

The reversible work for an electrochemical cell that uses hydrogen and oxygen is compared to the reversible work of a heat engine in Figure 6. The change in the Gibbs energy of the reaction decreases with the rise of temperature. Analysing Equation 2.13, one is able to see that that situation will result in a decrease in the maximum work output of the fuel cell with the rise of temperature.

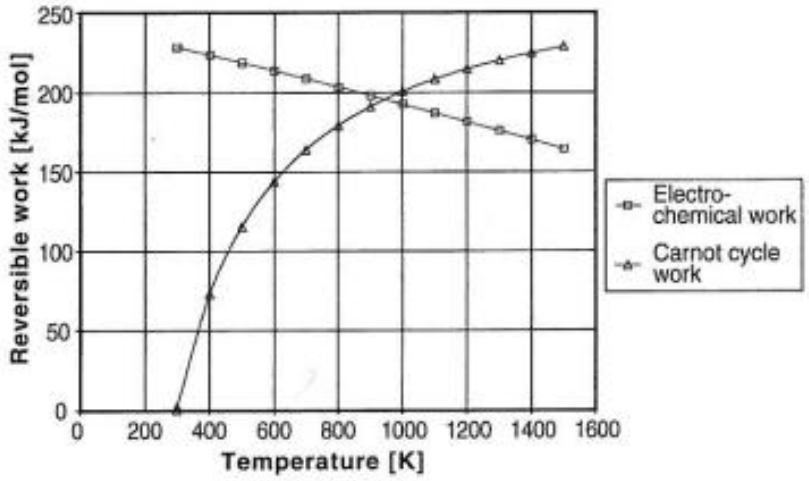

Figure 6: The reversible work produced by a H2/O2 fuel cell is greater than that of a Carnot engine at temperatures below 950 K. At higher temperatures, the Carnot engine is able to convert more of the HHV of H2 (285,840 kJ/mol) into work, [9]

The Gibbs energy of the formation of water vapour is $-228{,}582\ kJ/mol$ at the previously mentioned conditions ($25℃ - 298{,}15\ K$ and $1\ atm$) and decreases to $-164{,}429\ kJ/mol$ at $1500\ K$. As seen from Figure 6, the reversible work of the heat engine, using the HHV of hydrogen as the source of heat, increases with temperature. That is due to the fact that the Carnot cycle efficiency increases as well. The minimum temperature for which more reversible work is drawn from the combustion of hydrogen in a heat engine, rather than by direct conversion via fuel cell is, as seen in Figure 6, $950\ K$ (676,85℃).

Thermal efficiency of car engines is usually calculated in terms of power, meaning the heat input written as a rate according to the flow rate of fuel. An attempt to do the same in the calculation of the efficiency of a fuel cell, leads to the appearance in the equation of a factor related to the completeness of the combustion of fuel consumed to produce an electrical current. The analogous concept to completeness of combustion in direct conversion systems is fuel utilization, a measure of the fuel consumed to produce an electrical current, leading to the equation of the electrical efficiency, detailed in Equation 2.18.

$$\eta_I = \frac{I}{-n_e F N_{fuel}} = \frac{1}{fuel\ stoichiometry} \qquad \text{Equation 2.18}$$

In Equation 2.18, I is the current in *Amperes* and N_{fuel} is the flow rate of fuel in mol/sec. As seen from the previously mentioned equation, the inverse of the electrical efficiency is the

fuel stoichiometry. The fuel stoichiometry is in fact the relation between the amount of fuel fed and the amount required by the cell to provide the demanded electrons.

If hydrogen is in fact used as fuel, resulting in a current efficiency of 83% and considering that one mole of hydrogen contains two moles of electrons ($n_e = 2$), that means that 83% of the hydrogen is converted to electricity, while the remaining 17% either leave the cell without reacting or having reacted non-electrochemically, i.e., not contributing its electrons to the cell current).

Second Law Efficiency

"The Second Law efficiency, η_{2nd}, of an energy conversion device indicates its degree of reversibility, comparing the actual work against the maximum work potential", [9] (see Equation 2.19). The performance of an actual heat engine, for instance, would be the actual work performed by the engine divided by the work produced by a Carnot cycle engine. In a way, it is like comparing the actual work of an engine with the maximum it could provide.

$$\eta_{2nd,heat\ engine} = \frac{W_{act}}{W_{rev}} = \frac{W_{act}}{W_{Carnot}}$$ Equation 2.19

Considering that, in a fuel cell, the thermal efficiency becomes voltage efficiency, as in Equation 2.20.

$$\eta_{2nd,heat\ engine} = \frac{W_{act}}{W_{rev}} = \frac{nFE}{nFE^o} = \frac{E}{E^o}$$ Equation 2.20

The latter equation shows voltage efficiency to be a comparison between the actual voltage, E, with the maximum possible voltage, E^o. The actual meaning of this inefficiency applied to a Fuel cell represent is its losses (polarization) due to irreversibility. These phenomena will be further discussed in Section 2.3.4.

2.3 Fuel Cell

The basic principle of operation of a fuel cell consists in reversing water electrolysis to generate energy (electricity and heat) and water from hydrogen and oxygen. It was first discovered in 1839 by William Grove and remains unchanged until today.

"A fuel cell is an electrochemical "device" that continuously converts chemical energy into electric energy (and some heat) for as long as fuel and oxidant are supplied.", [9]

Like mentioned previously, fuel cells, unlike batteries, continuously generate electricity, as long as fuel is supplied. The fuel, like previously demonstrated, does not go through any type of combustion, resulting in a quiet process, pollution free (again, depending on FC type and manner to which fuel is obtained) and increased efficiency when compared with combustion processes.

The theoretical specific energy of hydrogen and oxygen combined in an electrochemical reaction is $3{,}6\ kWh/kg$ [11]. However, when the mass of fuel and oxidant storage tanks, as well as the mass of the fuel cell itself is taken into account, the overall specific energy density is reduced to values no greater than $1{,}0\ kWh/kg$ - still several times higher than that of a battery.

According to the *Manwearable Study Group Report [12]*, there are three main markets for fuel cell technology: stationary power, transportation power and portable power.

2.3.1 Types of fuel cells

The primary classification of a fuel cell is related to the kind of electrolyte used. That classification leads to the knowledge of the kind of chemical reactions that take place in the cell and other factors, such as, [13]:

- the kind of catalysts required;
- the temperature range in which the cell operates;
- the fuel required;
- other.

2.3.1.1 Reactant type

Fuel

As the reducing agent, fuel cells are able to use hydrogen, methanol, methane, carbon monoxide (CO), and other organic substances, as well as some inorganic reducing agents (e.g., hydrogen sulphide, hydrazine)

Oxidizing agent

As the oxidizing agent, fuel cells can use pure oxygen, air oxygen, hydrogen peroxide and chlorine. Versions with other exotic reactants have also been proposed, [12].

2.3.1.2 Electrolyte type

Fuel cells can use liquid electrolytes and solid electrolytes. Within the liquid electrolytes one can distinguish aqueous solutions of acids, alkalis and salts, and molten salts. The most common solid electrolytes are ionically conducting organic polymers, and inorganic oxide compounds.

Besides serving as separators, i.e., keeping reactants from reaching the wrong electrode space, solid electrolytes also have the advantage of reducing the danger of leakage of liquids from the cell. A liquid leakage in a fuel cell device may be a serious problem, since it may lead to corrosive interaction with the construction materials.

2.3.1.3 Working temperature

One distinguishes low-temperature fuel cells, those having a working temperature of no more than 250°C; and high-temperature fuel cells, over 650°C. Low-temperature fuel cells include membrane-type fuel cells, alkaline fuel cells and phosphoric acid electrolyte. High-temperature fuel cells include fuel cells with molten carbonate (working temperature 600 to 700°C) and solid-oxide fuel cells (working temperature above 900°C). In recent years, interim-temperature fuel cells with a working temperature in the range 200 to 650°C have been introduced. These include certain varieties of solid-oxide fuel cells developed more recently. The temperature ranges are stated conditionally.

The following table compares the different features between low temperature and high temperature fuel cells:

Table 1: Features of low and high temperature fuel, [12]

Low temperature FC	**High temperature FC**
Generally incorporate precious metal electrocatalysis to improve performance	Increased operating temperature reduces the need for expensive electrocatalysts
Require a relatively pure supply of hydrogen as a fuel (e.g. PEM catalysts are poisoned by carbon monoxide; AFCs damaged by carbon dioxide). This usually means that a fuel processor is required to convert primary fuels such as natural gas	Fuel flexibility: can be operated on a range of hydrocarbon fuels; Benefits in Combined Heat and Power (CHP) generation
Exhibit fast dynamic response and short start-up times	Exhibit long start-up times and are sensitive to thermal transients
Available commercially	May require expensive and exotic construction materials to withstand the operating temperature, particularly in the balance of plant (piping, heat exchangers, etc.) Reliability and durability may be a concern

2.3.2 Overall Comparison

Below is compiled a table resuming the main features of the different types of fuel cells previously discussed.

Table 2: Fuel cell Type Comparison, [14]

Fuel cell Type	Common Electrolyte	Operating Temperature	Typical Stack Size	Efficiency	Applications	Advantages	Disadvantages
Alkaline (AFC)	Aqueous solution of potassium hydroxide soaked in a matrix	$90-100℃$	10-100 kW	60%	Military Space	Cathode reaction faster in alkaline electrolyte, leads to high performance Low cost components	Sensitive to CO2 in fuel and air Electrolyte management
Polymer Electrolyte Membrane (PEM)	Perfluoro sulfonic acid	$50-100℃$, Typically $80℃$	< 1 kW-100 kW	60% transportation	Backup power Portable power Distributed generation Transportation Specialty vehicles	Solid electrolyte reduces corrosion & electrolyte management problems Low temperature Quick Start-up	Expensive catalysts Sensitive to fuel impurities Low temperature waste heat
Phosphoric Acid (PAFC)	Phosphoric acid soaked in a matrix	$150-200℃$	400kW 100 kW module	40%	Distributed generation	Higher temperature enables CHP Increased tolerance to fuel impurities	Pt catalyst Long start up time Low current and power
Molten Carbonate (MCFC)	Solution of lithium, sodium, and/or potassium carbonates, soaked in a matrix	$600-700℃$		45-50%	Electric utility Distributed generation	High efficiency Fuel flexibility Can use a variety of catalysts Suitable for CHP	High temperature corrosion and breakdown of cell components Long start up time Low power density
Solid Oxide (SOFC)	Ytrria stabilized zirconia	$700-1000℃$	1kW-2MW	60%	Auxiliary power Electric utility Distributed generation	High efficiency Fuel flexibility Can use a variety of catalysts Solid electrolyte Suitable for CHP & CHHP Hybrid/GR cycle	High temperature corrosion and breakdown of cell components High temperature operation requires long start up time and limits
Direct Methanol (DMFC)	Nafion	$50-120℃$		<40%	Portable electronic systems of low power, running for long times	Technical maturity High energy density Fast start-up Commercially available Easy to carry and handle Simple to use	Toxic fuel Higher MEA cost (may limit cost reduction facing other technologies) Limited power density Exhaust moisture

2.3.3 PEM Fuel Cell

This work performed in this dissertation focused solely on PEM type FC, for that matter, there will be a detailed description of this particular FC system, while leaving the remaining studied types available as annexes (see Annexe E).

Firstly developed by General Electric in the 1960s for use in space exploration by NASA, the PEMFC, also called solid polymer fuel cell (SPFC), has known commercialization over the past few years and is currently the focus of several engineering studies, especially for applications in the automobile industry.

The low working temperature of the polymer electrolyte makes it easy for the PEMFC to start quickly. The fact that the system does not contain any corrosive fluid combined with the ability of working in any orientation makes it particularly suitable for portable applications, such as vehicles.

A disadvantage shared with the Alkaline FC (see Annexe E) is that liquid water also forms at the cathode at the operating temperatures. Again, the humidity of the reactant gases must be controlled in order to avoid dry-out or flooding of the cell. While neither of which leads to cell destruction, either of which may lead to efficiency decrease and shortened operating life. Below are some advantages and disadvantages regarding PEM FC systems.

Advantages:

- Highest power density within the range of fuel cells;
- Simplest fuel cell in the range;
- Has the potential to be used for vehicle applications;
- Low temperature signature is dependent upon the ability to manage the heat output;
- Can work in reversible mode.

Disadvantages:

- Pure Hydrogen as fuel;
- Cost of fuel cell;
- Water management difficult;
- Need for expensive catalysts.

Reactions

Anode: $H_2 \rightarrow 2H^+ + 2e^-$

Cathode: $1/2O_2 + 2H^+ + 2e^- \rightarrow H_2O$

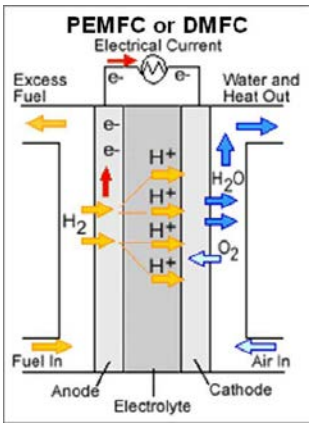

Figure 7: Schematic of a PEMFC operation, [14]

PEM Fuel Cell System Description

This sub-section provides a brief insight on the composition of a PEM FC system.

As seen in Figure 8, a PEMFC comprises the following components:

- Bipolar plates: conventionally graphite plates with machined gas flow-field channels. They provide a separation between the individual fuel cells and conduct current from cell to cell. The selected bulk material should have low electrical resistance, as well as low interfacial contact resistance between the GDL's and the bipolar plates, in order to improve fuel cell performance.
- End Plates: The two outermost components placed on the extremities of the fuel cell stack. They are usually made of stainless steel or aluminium and are a part of the clamping system. Its major role is to provide a uniform pressure distribution between various components of the fuel cell stack and consequently reducing contact resistance between them, thus unitizing them.
- Membrane electrode assemblies (MEAs): comprises the ion conducting electrode, a cathode and an anode, the primary components of the Fuel Cell, often referred to as the MEA, or simply a single-cell fuel cell. The most commonly used electrolyte in PEMFC is Nafion, [15]
- Gas diffusion layers (GDLs): transports gases and ions to and from the rest of the MEA.
- Gaskets: have a critical function, within the operation of a fuel cell, guaranteeing the sealing of the stack, while subjected to acidic liquid solution, humid air and hydrogen, as well as considerable mechanical stress. The durability of a fuel cell system is therefore greatly dependent on the durability and stability of gasket material, [16]

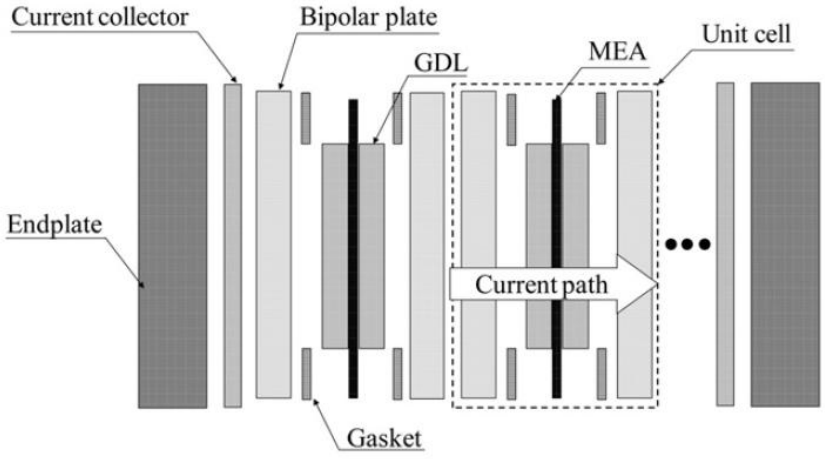

Figure 8: Schematic diagram of a PEMFC stack, [17]

The overall efficiency of the fuel cell depends on the performance of the bipolar/end plates in the fuel cell stack.

Figure 9 shows the relative weight of some stack components.

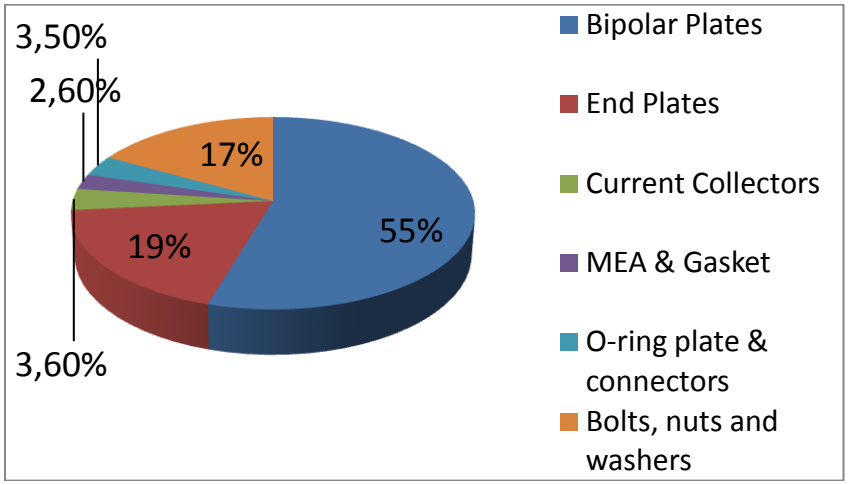

Figure 9: Relative weight components of a PEMFC using graphite bipolar plate, [3]

End Plates

As previously mentioned, the End Plates' main goal is to provide a compressive clamping force to the remaining stack components, in order to ensure good electrical contact (low Ohmic resistance) between the multiple layers within the stack. Adequate pressure is fundamental, for there are risks associated with too low and too high pressure. Low pressure will result in voltage drop, due to high contact resistance between gas diffusion backing and the bipolar plates, as well as possible leakage, both resulting in diminished system performance. Excessive or uneven pressure, however, will result in non-uniform current density and heat generation distribution which may cause hot spot formation in the MEA and finally its failure, as well as a change in the porosity ratio of the GDL, damaging it, and possible fracture of the bipolar plates, [2]

Figure 10 depicts the deflection of the end plates caused by the clamping force.

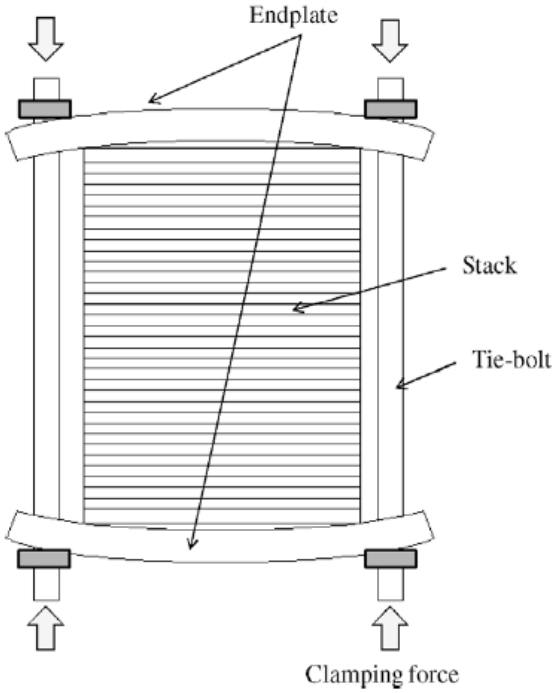

Figure 10: Deflection of End Plates of a Fuel Cell by clamping force, [18]

To clarify, main implications related with current End Plate use are, [4]:

- Deformation of end plates has an influence on fuel cell performance and is difficult to control;
- End Plates are typically bulky and heavy, as compared to the fuel cell stacks;
- Tie rods tend to loosen up during service. This may cause leakage, bad electrical contacts and deteriorated performance of the fuel cell stacks;
- Repeatability in pressure distribution can hardly be realized among the fuel cell stacks.

"The optimum pressure value is achieved throughout the fuel cell active area, but in reality it can only be achieved in a very small portion of the area because of the structure in the conventional end plates. Therefore, the most relevant shortcoming of the existing end plate design is the difficulty of achieving a uniform pressure distribution over the fuel cell active area.", [4]

There has been much research on how to improve fuel cell performance, however very little of it has been focused on the end plates, and the pressure distribution between the fuel cell stacks, [18]

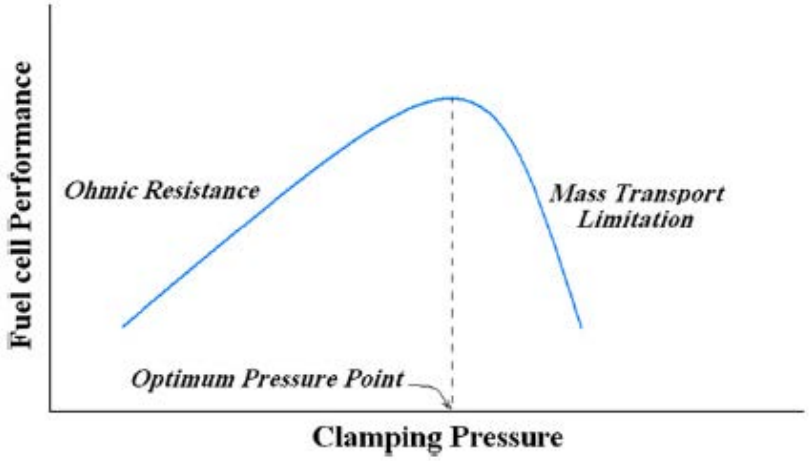

Figure 11: Effect of clamping pressure on the fuel cell performance, [2]

2.3.4 Ideal Performance and available energy measurement of a fuel cell

An important issue when dealing with this kind of energy storage technology is the need to have a general understanding of the effect of the stored reactant's conditions (pressure and temperature) on the electrical energy production. Such a relation is made through the Nernst equation.

The Nernst equation relates the ideal standard potential, E^o, at $25℃; 1\,atm$ for the cell reaction with the ideal equilibrium potential, E, at other temperatures and partial pressures of reactants and products. In fact, the value of E represents the theoretical limit of cell voltage and thus the highest efficiency that laws of thermodynamics will allow for a fuel cell with a given reactant pressure and temperature.

Table 3: Fuel Cell Reactions and the Corresponding Nernst Equations, [19]

Fuel Cell	Cell Reactions	Nernst Equation
Proton Exchange Membrane and Phosphoric Acid	$H_2 + 1/2O_2 \rightarrow H_2O$	$E = E^o + \left(\frac{RT}{2F}\right) ln\left[\frac{P_{H_2}}{P_{H_2O}}\right] + \left(\frac{RT}{2F}\right) \ln[P_{O_2}^{1/2}]$
Alkaline	$H_2 + 1/2O_2 + CO_{2\,(c)} \rightarrow H_2O + CO_{2\,(a)}$	$E = E^o + \left(\frac{RT}{2F}\right) ln\left[\frac{P_{H_2}}{P_{H_2O}(P_{CO_2})_{(a)}}\right] + \left(\frac{RT}{2F}\right) \ln[P_{O_2}^{\frac{1}{2}}(P_{CO_2})_{(c)}]$
Molten Carbonate	$CO + 1/2O_2 \rightarrow CO_2$	$E = E^o + \left(\frac{RT}{2F}\right) ln\left[\frac{P_{CO}}{P_{CO_2}}\right] + \left(\frac{RT}{2F}\right) \ln[P_{O_2}^{1/2}]$
Solid Oxide	$CH_4 + 2O_2 \rightarrow 2H_2O + CO_2$	$E = E^o + \left(\frac{RT}{8F}\right) ln\left[\frac{P_{CH_4}}{P_{H_2O}^2 P_{CO_2}}\right] + \left(\frac{RT}{8F}\right) \ln[P_{O_2}^2]$

(a) - anode

(c) - cathode

E - equilibrium potential

F - Faraday's constant

P - gas pressure

R - universal gas constant

T - temperature (absolute)

As seen from Table 3, the higher the pressure of the fuel, the higher will the cell potential at a given temperature be.

The impact of temperature on the ideal voltage, E, for the oxidation of hydrogen is shown in Table 4.

Table 4: Ideal Voltage as a function of Cell Temperature, [19]

Temperature	80℃ (353 K)	100℃ (373 K)	205℃ (478 K)	650℃ (923 K)	800℃ (1073 K)	1100℃ (1373 K)
Cell Type	PEMFC	AFC	PAFC	MCFC	ITSOFC	SOFC
Ideal Voltage (V)	1,17		1,14	1,03		0,91

There are however irreversible losses that decrease the ideal cell voltage and must be accounted for. The losses, which are often called polarization, overpotential, or overvoltage, originate primarily from three sources:

1. activation polarization
2. ohmic polarization
3. concentration polarization

The actual voltage of the cell, V, is then the ideal potential subtracted by the mentioned losses, as in Equation 2.21.

$$V = E - Losses$$ Equation 2.21

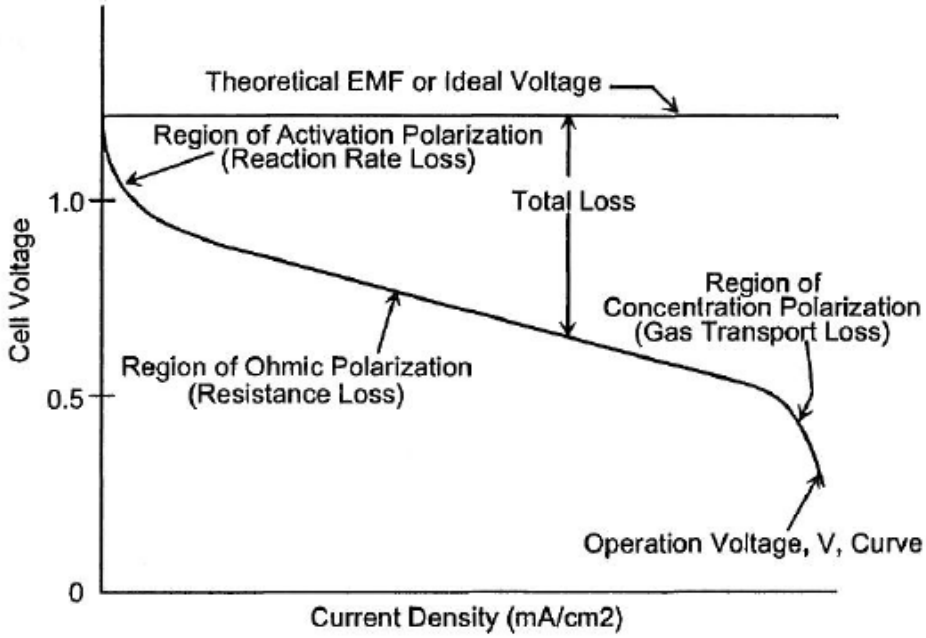

Figure 12: Ideal and Actual Fuel Cell Voltage/Current characteristic, [19]

As seen in Figure 12, the activation polarization occurs at low current density. Its physical significance is similar to that of the static friction and represents the limiting effects of the oxidation/reduction kinetics. In a way, they are the electronic barriers that have to be overcome prior to current and ion flow takes place.

Ohmic polarization increases linearly with the increase in current, since cell resistance is essentially constant.

Concentration losses come as the result of starvation at certain reaction sites, as a consequence of fluid flow resistance. This type of losses takes place over the entire range of current density, however it becomes more prominent at high limiting currents when there is a inability of the surrounding material to maintain the initial condition of the bulk fluid.

1. **activation polarization**

$$\eta_{act} = \frac{RT}{\alpha\, n\, F} ln \frac{i}{i_0}$$ Equation 2.22

Where α is the electron transfer coefficient of the reaction at the electrode being addressed, and i_0 is the exchange current density.

2. **ohmic polarization**

$$\eta_{ohm} = iR$$ Equation 2.23

Where i is the current flowing through the cell, and R is the total cell resistance, which includes electronic, ionic, and contact resistance.

3. **concentration polarization**

$$\eta_{conc} = \frac{RT}{n\,F} \ln\left(1 - \frac{\mathrm{i}}{\mathrm{i_L}}\right)$$ Equation 2.24

Where $\mathrm{i_L}$ is the limiting current.

The available cell voltage is the difference between the available potential in the cathode with the one at the anode, subtracted by resistance losses, as in the following equation.

$$V_{cell} = V_{cathode} - V_{anode} - iR$$ Equation 2.25

One must then have to take into account the other two mentioned losses occurring separately in both anode and cathode. The total polarization at the electrodes is the sum of activation, η_{act}, and concentration polarization, η_{conc}, as demonstrated in the following equations:

$$\eta_{anode} = \eta_{act,a} + \eta_{conc,a}$$ Equation 2.26

$$\eta_{cathode} = \eta_{act,c} + \eta_{conc,c}$$ Equation 2.27

The effect of polarization is to shift the potential of the electrode ($E_{electrode}$) to a new value ($V_{electrode}$):

$$V_{electrode} = E_{electrode} \pm |\eta_{electrode}|$$ Equation 2.28

For the anode (Equation 2.29) and cathode (Equation 2.30):

$$V_{anode} = E_{anode} + |\eta_{anode}|$$ Equation 2.29

$$V_{cathode} = E_{cathode} - |\eta_{cathode}|$$ Equation 2.30

Substituting Equation 2.29 and Equation 2.30 into Equation 2.25:

$$V_{cell} = E_{cathode} - |\eta_{cathode}| - (E_{anode} + |\eta_{anode}|) - iR$$ Equation 2.31

Or, since $\Delta E_e = E_{cathode} - E_{anode}$, then:

$$V_{cell} = \Delta E_e - |\eta_{cathode}| - |\eta_{anode}| - iR$$ Equation 2.32

From the equation above, it is possible to observe the decrease in cell voltage with the increase in current due to losses by electrode and ohmic polarizations. Ideal is that V_{cell} approaches ΔE_e as best as possible. That aim can be reached either by modifications in fuel cell design, such as improvement in electrode structures, better electrocatalysts, more conductive electrolyte, thinner cell components, etc., or by modifying the fuel cell operating conditions, i.e., higher gas pressure, higher temperature, change in gas composition to lower the gas impurity concentration. Nevertheless, complications regarding stability and durability arise within a fuel cell system when operating at higher temperature or pressure. Any modification in operation conditions must have the basic limitations of the working type into account.

2.3.5 Fuel Cell Performance Variables

By analyzing the changes in the Gibbs free energy caused by variations in temperature and pressure, it is possible to know the effect of the variation of the mentioned parameters on the ideal potential, E.

$$\left(\frac{\partial E}{\partial T}\right)_P = \frac{\Delta S}{n\,F} \qquad \text{Equation 2.33}$$

$$\left(\frac{\partial E}{\partial P}\right)_T = \frac{-\Delta V}{n\,F} \qquad \text{Equation 2.34}$$

The reversible potential of the H_2/O_2 fuel cell decreases with an increase in temperature by 0,84 mV/ºC (*Fuel Cell Handbook*), since the entropy change for the H_2/O_2 reaction is negative (assuming reaction product is liquid water). However, for the same reaction, the reversible potential increases with an increase in pressure, since the volume change is negative.

Figure 13 shows the practical effect of temperature on the voltage of some types of early life fuel cells, along with the variation of the reversible potential of H_2/O_2 fuel cells.

The cell voltages of PEMFCs, PAFCs and MCFCs show a strong dependence on temperature, with the PEMFC exhibiting a maximum, but also PAFCs, MCFCs and PAFC show an increase in operating voltages, while the reversible potential decreases with increasing temperature.

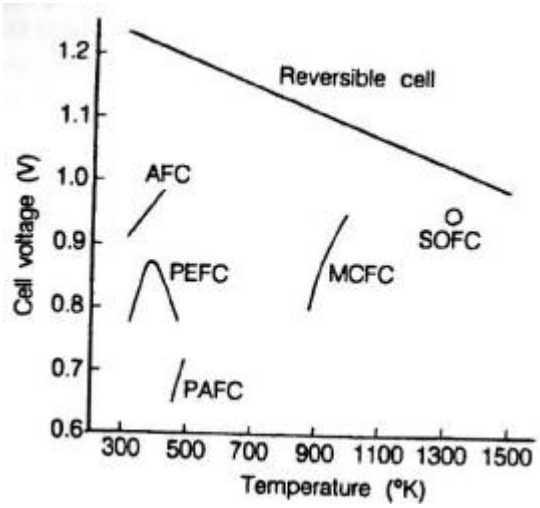

Figure 13: Dependence of the Initial Operating Cell Voltage of Typical Fuel Cells on Temperature, [19]

2.3.6 Balance of Plant

The Balance of Plant (BoP) comprises all remaining infrastructural systems, components and structures necessary for the fuel cell operation. Since this is such a vast field of discussion and mentioning all necessary components for all the possible types of a fuel cell system would result in a large workload, [12] defines five functional areas within the BoP, as seen in Diagram 1.

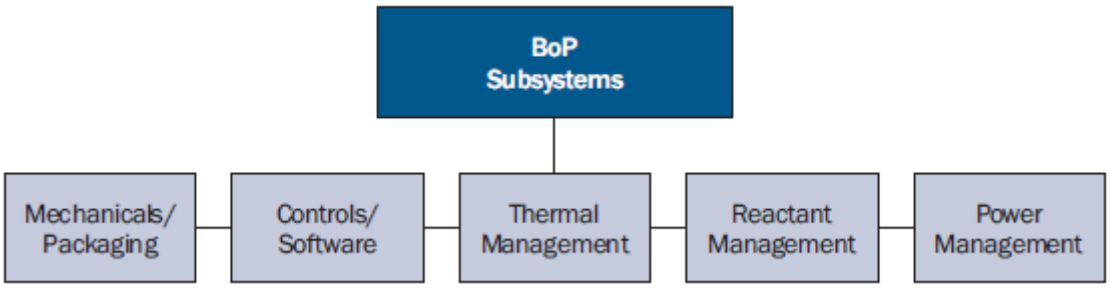

Diagram 1: BoP subsystems, [12]

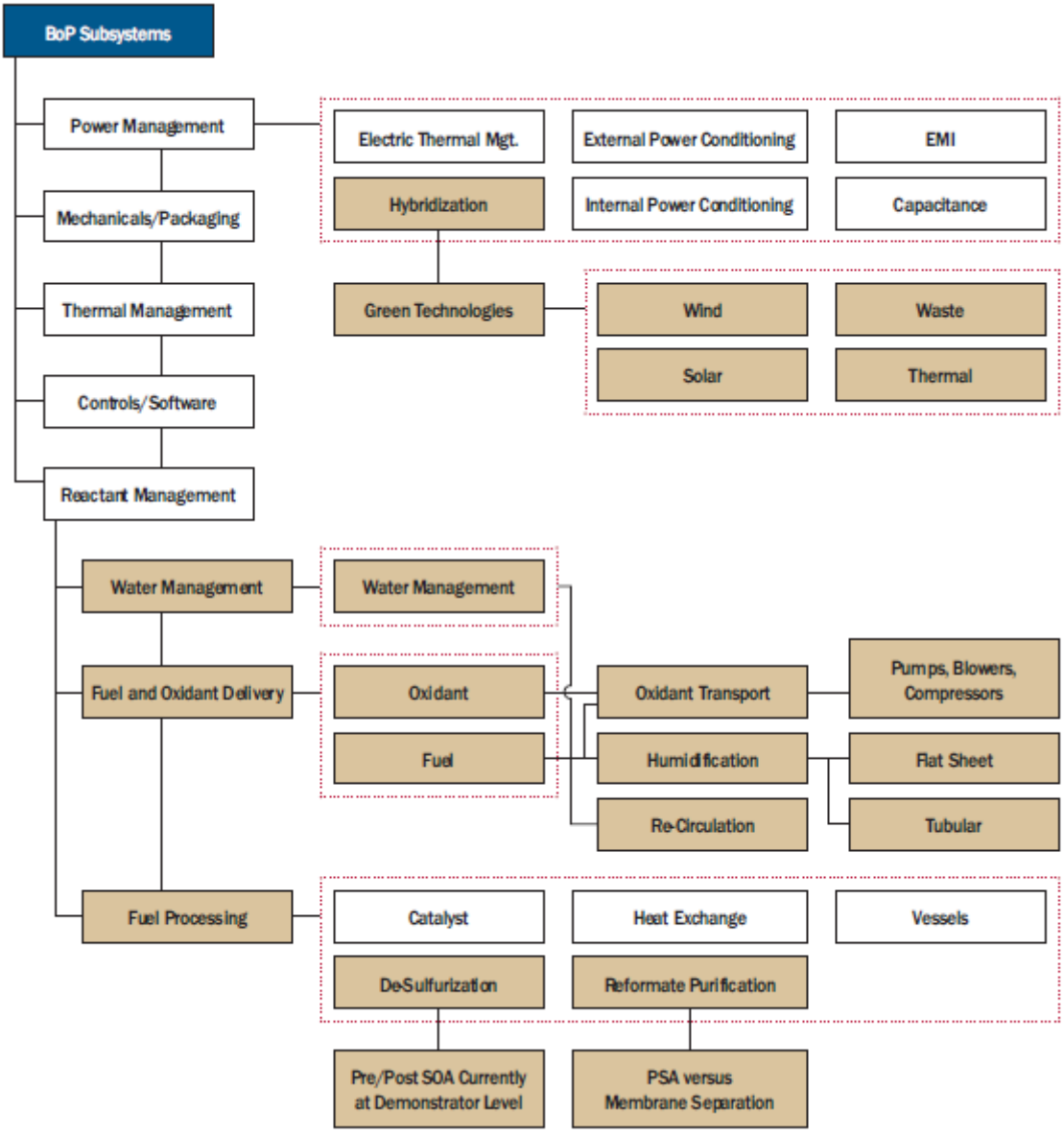

Diagram 2: BoP subsystems expanded, [12]

According to [20], significant BoP components include a primary pressure regulator, solenoid control valves, fill tube/port, and pressure gauge/transducer. A schematic for an automotive application based on the requirements defined in the draft European regulation "Hydrogen Vehicles: On-board Storage Systems" and US Patent 6.041.762 is given in Figure 14.

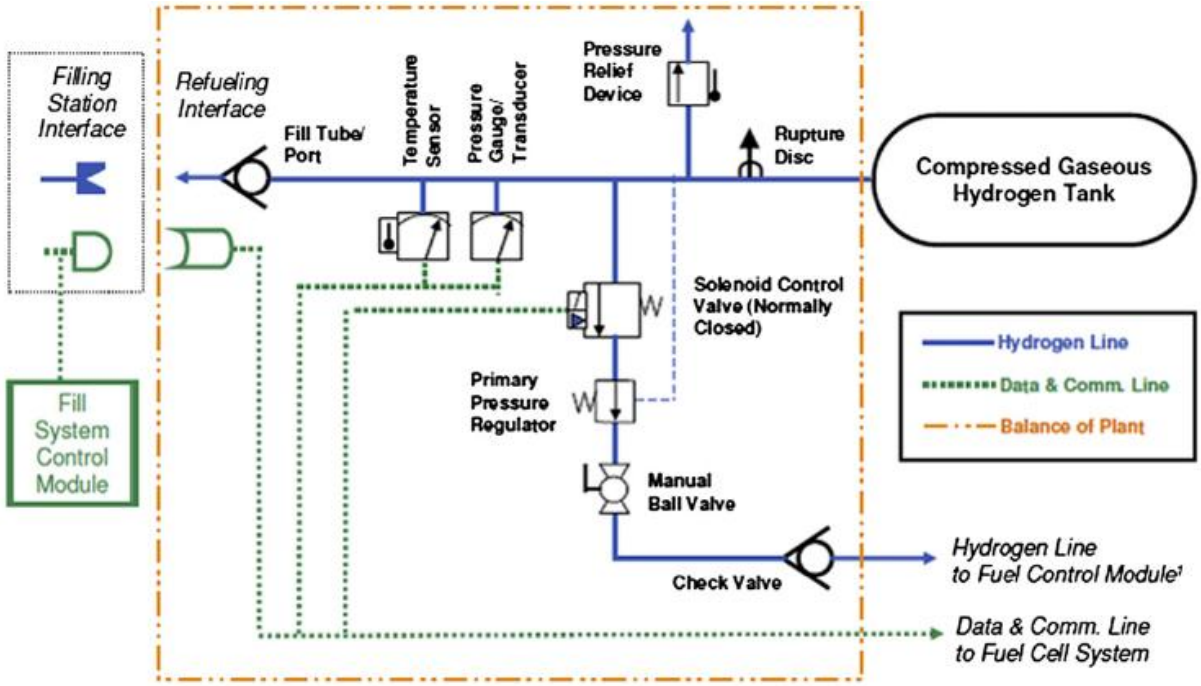

Figure 14: On-board compressed hydrogen storage system schematic, [20]

2.3.7 Fuel and Oxygen Storage

An area fundamental to a FC system is the fuel and oxygen storage. The fuel storage issue is fundamental to the objective at hand. For that matter this will be properly discussed, while the oxygen storage will only be briefly discussed in the following sections.

Fuel Storage

According to [21], there are three leading options:

1. Compressed hydrogen gas storage: this system comprises storing compressed pure hydrogen as a compressed gas in a high-pressure cylinder. The gas can be stored at ambient temperature, not requiring costly thermal insulation.
2. Metal hydride storage: Hydrides are reversible hydrogen compounds formed by the absorption of hydrogen under moderate pressures and low temperatures. The storage tank contains powdered metals that absorb hydrogen and release heat when the hydrogen is forced into the tank under pressure. The hydrogen is released from the compound when the pressure is reduced and heat is applied.
3. Onboard methanol reformer system: This fuel storage type required the vehicle to have a methanol storage tank, a steam reformer to produce hydrogen gas and the rest of the components are the same as hydrogen powered fuel cell vehicles.
4. Cryogenic storage: although not considered in [21], there is the possibility of cooling the hydrogen to extremely low temperatures (-253ºC; 6-350 bar), thus liquefying the hydrogen. In a liquid state, hydrogen is denser, thus containing more stored energy, however tank insulation required to prevent hydrogen loss considerably increases weight, [22].

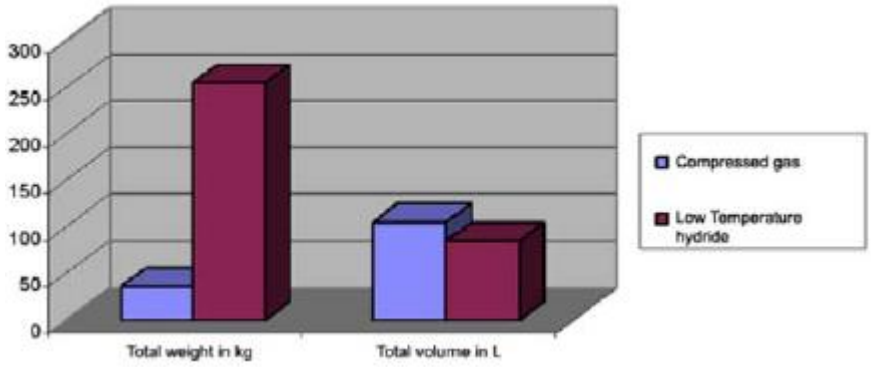

Figure 15: Comparison of compressed gas vs. metal hydride options, [23]

Development on Compressed Hydrogen Storage Tanks

According to [24], there are four categories into which high-pressure tanks can be classified:

- Type I: all metal tanks;
- Type II: metal tanks (metal liner hoop) wrapped with resin-impregnated filament winding in a circumferential direction;
- Type III: tanks are made of composite materials (fibreglass; carbon fibre) with a metal liner (aluminium; steel), i.e., the inside facing acting as H_2 barrier.
- Type IV: Composite tanks with a polymer liner (mostly thermoplastic polymers, of the polyethylene or polyamide families).

As seen from Figure 16, Type III and IV storage tanks with composite material composition can withstand higher pressure per mass, and thus store more Hydrogen. Filament winding is the used process for Types II, III and IV storage tanks, for it offers the best fibre/matrix interface and therefore the best stiffness/weight ratios, [25]. The process comprises the placement of fibre bundle onto a rotating removable mandrel in the same orientation as the load that it is intended to withstand. Composite parts for axisymetric structures, such as high pressure storage tanks, can be highly optimized through the use of this process, resulting in a greater performance factor, as seen from Figure 16.

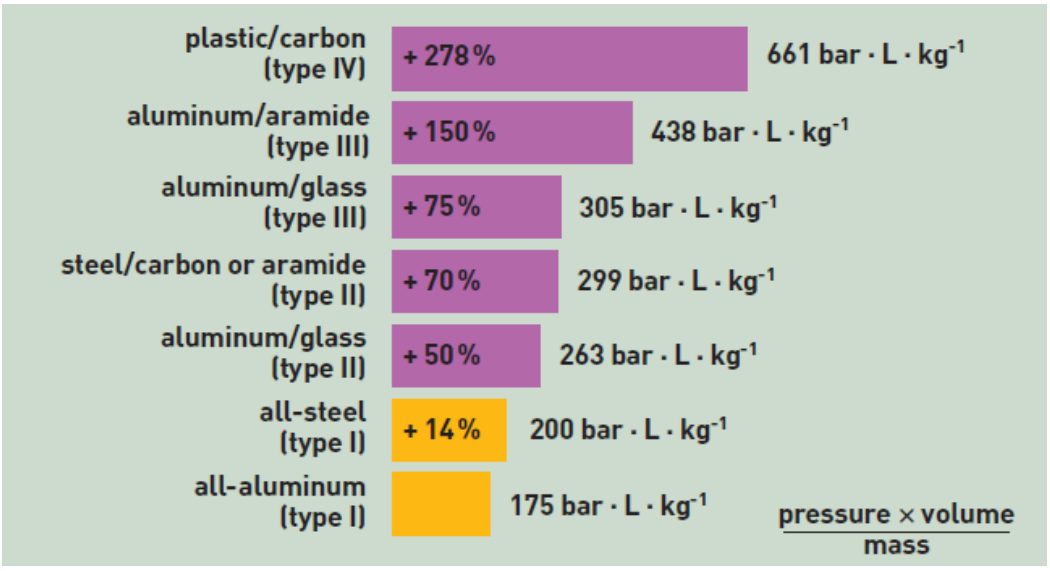

Figure 16: Comparative analysis of the performance factor ($pressure \times volume/mass$) of various tank types, [24]

Compressed Hydrogen storage tank systems assessment

A technical assessment of compressed hydrogen storage tank systems for automotive applications was conducted by [20]. The study comprised the study of storage systems with design pressures of 350 bar ($350 \times 1.05 \times 10^5\ Pa$) and 700 bar ($700 \times 1.05 \times 10^5\ Pa$) for Type III and IV storage systems with single- and dual tank systems and compares each parameter result with the Department of Energy (DOE) 2010 and 2015 targets. The summary results of the assessment are given in Table 5.

Table 5: Summary results of the assessment for Type III (T3) and Type IV (T4) single and dual-tank compressed hydrogen storage systems, [20]

Performance and cost metric	Units	cH2 350-T3	cH2 350-T3	cH2 350-T4	cH2 350-T4	cH2 700-T3	cH2 700-T3	cH2 700-T4	cH2 700-T4	2010 Targets	2015 Targets	Ultimate Targets
Tank		1-Tank	2-Tank	1-Tank	2-Tank	1-Tank	2-Tank	1-Tank	2-Tank			
Total storage capacity	kg-H_2	6.0	6.0	6.0	6.0	5.8	5.8	5.8	5.8			
Usable storage capacity	kg-H_2	5.6	5.6	5.6	5.6	5.6	5.6	5.6	5.6			
System gravimetric capacity	wt%	4.2	4.0	5.5	5.0	3.6	3.5	5.2	4.8	4.5	5.5	7.5
System volumetric capacity	kg-H_2/m^3	17.4	17.2	17.6	17.2	25.0	24.7	26.3	25.6	28	40	70
Storage system cost	$/kWh	16.8	16.9	15.4	15.8	21.2	21.4	18.7	19.2	4	2	TBD
Fuel cost	$/gge	4.2	4.2	4.2	4.2	4.3	4.3	4.3	4.3	2–3	2–3	2–3
Cycle life (1/4 tank to full)	Cycles	5500	5500	NA	NA	5500	5500	NA	NA	1000	1500	1500
Minimum delivery pressure, FC/ICE	atm	4	4	4	4	4	4	4	4	4/35	3/35	3/35
WTT efficiency	%	56.5	56.5	56.5	56.5	54.2	54.2	54.2	54.2	60	60	60
GHG emissions (CO2 eq.)	kg/kg-H_2	14.2	14.2	14.2	14.2	14.8	14.8	14.8	14.8			
Ownership cost	$/mile	0.13	0.13	0.13	0.13	0.15	0.15	0.14	0.14			

Since this assessment is intended for an automotive application, the two most important parameters that can be extracted from this table are the System gravimetric capacity, $wt\%$ (weight of usable hydrogen divided by total onboard tank system weight), and System volumetric capacity in mass of H_2 per system cubic meter (kg/m^3). Since this assessment was made for automotive applications, the mentioned cost parameters are only used for means of comparison, for they do would have to be recalculated if a UAV application is being considered.

Regarding $wt\%$ and the system volumetric capacity, the first conclusion drawn from this assessment is that the one-tank solution is more attractive than the two-tank solution regarding the two mentioned parameters, having identical Ownership and Fuel cost. Furthermore, the 2010 $wt\%$ target of 4,5% is reached in Type IV tanks for both pressures (350 bar and 700 bar) and for both tank systems (single- and dual-tank), while the 5,5% 2015 target for the same parameter is only reached for the Type IV, 350 bar, one-tank solution. Regarding System volumetric capacity, however, assessment shows the parameter's failure in reaching both 2010 and 2015 targets in all given system possibilities.

Oxygen Storage

As previously mentioned, there are some types of FC applications that require the storage of oxygen for the system operation, whether it is because the system requires pure oxygen or because it leads to increased system efficiency. From [23], the available options for an autonomous underwater vehicle (AUV) that can be transposed to UAV are:

- Compressed gas vessel;
- Low-temperature liquid oxygen tank;
- Hydrogen peroxide storage.

Figure 17 provides with a comparison of the required weight and volume of the storage system, so as to store 16,7 kg of oxygen.

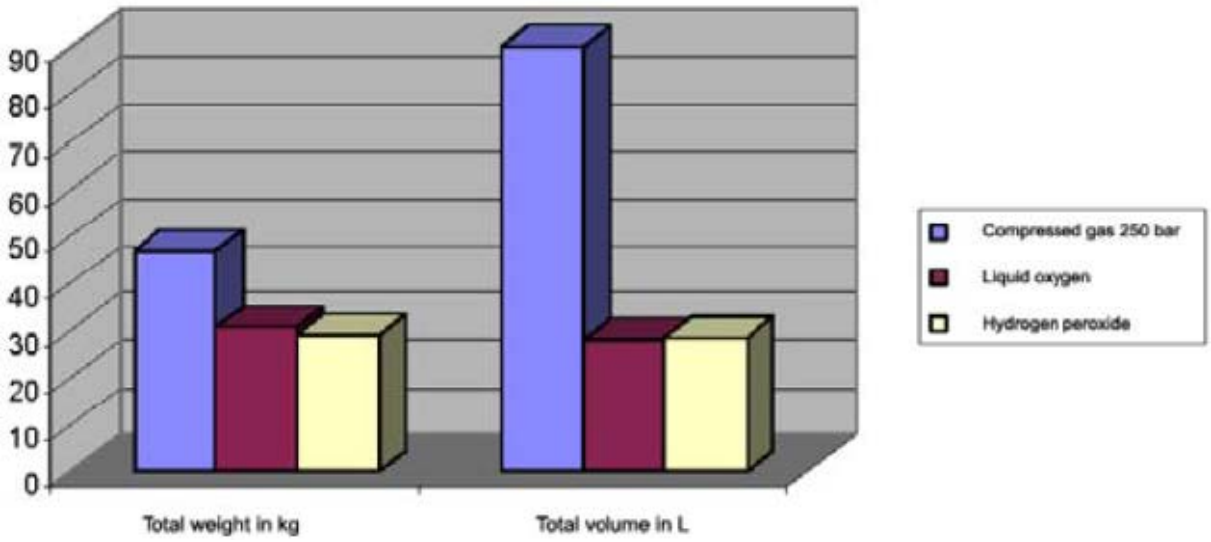

Figure 17: Comparison of oxygen storage options (16,7 kg Oxygen), [23]

There is also a possibility for UAVs that cannot be transposed to AUV, which is the use of a compressor. Since PEM FC systems do not require a feed of pure oxygen, a compressor may be a suitable manner of providing oxygen at the required pressure to the system, without having to be concerned with heavy storage unit systems.

2.4 Internal Combustion Engine

Internal combustion engines distinguish themselves for the high specific energy of its hydrocarbon and hydrogen fuels. Especially when compared with other energy storage systems, such as batteries. Despite having low thermal efficiencies as previously demonstrated (sometimes as low as 5%), the specific energy of hydrocarbon fuels can be as high as 11 000 Wh/kg, and about as 8 000 Wh/kg considering the required system mass, [26]. If this is compared to the 160 and 330 Wh/kg for alkaline and lithium batteries, respectively, one reaches the conclusion that ICEs can still be far superior to battery-motor electrical systems in many applications. Figure 18 compares the pure and system specific energy of some storage systems, such as compressed hydrogen at 700 bar and gasoline.

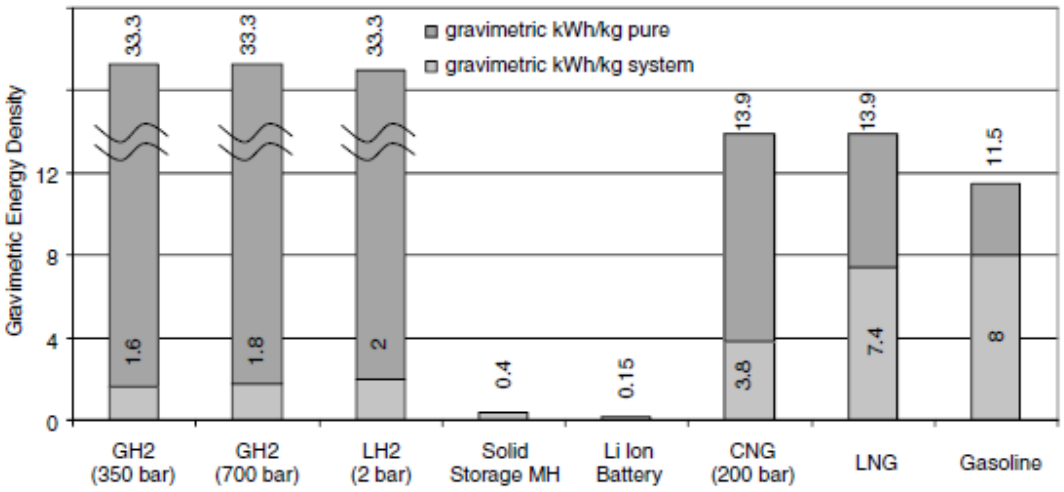

Figure 18: Pure and System Specific Energy of storage systems, [26]

Taking into account the flight consumption pattern of an UAV, a combination of ICE with an electric motor (EM), i.e., a hybrid system would be interesting. The hybrid system configurations that follow can also be thought of for applications where the Fuel Cell is used as the main propulsive system. For that matter, this issue will be further discussed.

2.4.1 Hybrid-electric Propulsion System

In a hybrid propulsion system, two or more power sources are combined together to increase the efficiency of the vehicle. There are several possibilities, regarding configuration of hybrid systems, the most commonly used being:

- Series
- Parallel
- Power-Split

A study carried out by [27] demonstrated a significant decrease in energetic consumption for a UAV with hybrid configuration when compared to a four-stroke gasoline powered UAV: 52% and 22% less energy use for a one-hour and three-hour intelligence, surveillance or reconnaissance mission, respectively), [28]

A brief description of the mentioned configurations will be performed below.

Series

Features:

- EM is the sole component providing power to the mechanical drive train, leaving the Internal Combustion Engine (ICE) as an auxiliary power unit with the role of driving the EM to propel the aircraft, through the Generator and then Battery

Advantages:

- This configuration enables the ICE to operate at optimum torque and speed range, regardless of the driving conditions.

Limitations:

- Considerable energy conversion losses, since the mechanical energy of the ICE must be firstly converted to electrical energy and then back to mechanical energy through the EM to power the propeller, resulting in an overall system efficiency reduction.

- Another limitation that arises from this configuration is the fact that the EM and Battery generally need to be bigger to meet peak power demands, even if the ICE can be smaller, since it only has to meet average power demands. Furthermore, the Generator needs also to be taken into account, resulting in a significant weight penalty and making this configuration unsuitable for small UAVs.

See Figure 19.

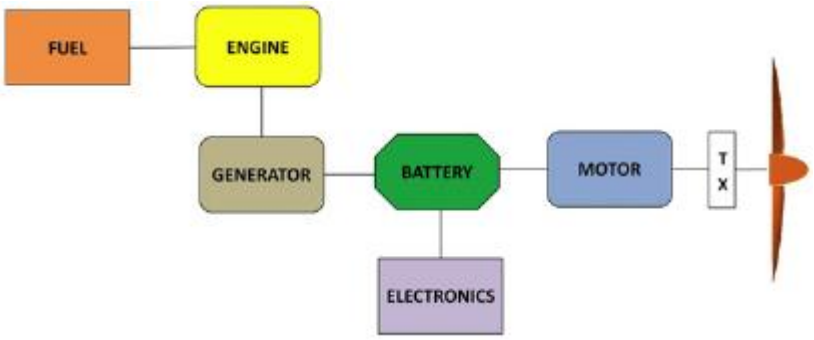

Figure 19: Hybrid Series configuration, [28]

Parallel

Features:

- Commonly used in some of today's automobile hybrid vehicles (e.g., Honda Insight, Civic and Accord).

Advantages:

- Redundancy that comes from the ability of propelling the aircraft either by ICE alone, EM alone, or both simultaneously if required. In fact, this configuration ensures a combination of high endurance, acoustic quietness, high reliability, and redundancy. The latter being a very important feature in UAV applications.

Limitations:

- The ICE does not operate continuously in its most efficient region, naturally leading to decreased efficiency. A way of mitigating this effect is to integrate a Continuously Variable Transmission (CVT), rather than a conventional transmission. Doing so will

however raise difficulties in torque control and in maximizing efficiency when different or combined power sources are required.

See Figure 20.

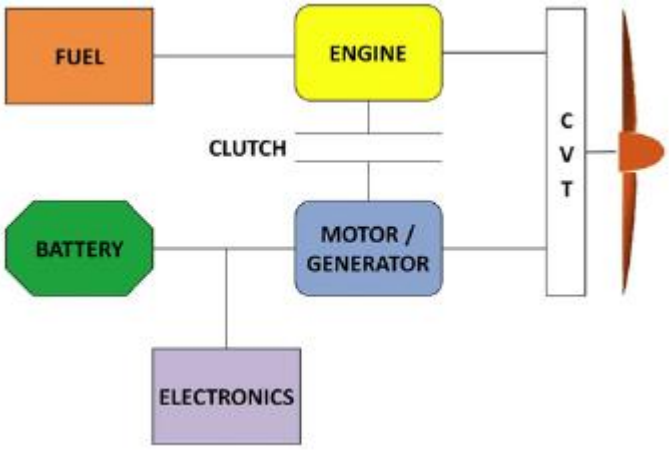

Figure 20: Hybrid Parallel Configuration, [28]

Power-Split

Features:

- Configuration currently in use on hybrid automobiles such as the *Toyota Prius* and comprises a planetary gear used to transfer the power generated by the ICE and/or EM to propel the UAV, therefore comprising no direct connection between the various power plants and the mechanical drive train.

Advantages:

- It combines the various power sources in a more efficient manor, thus reducing fuel usage.

Limitations:

- Cost and control are disadvantages which must be properly considered.

See Figure 21.

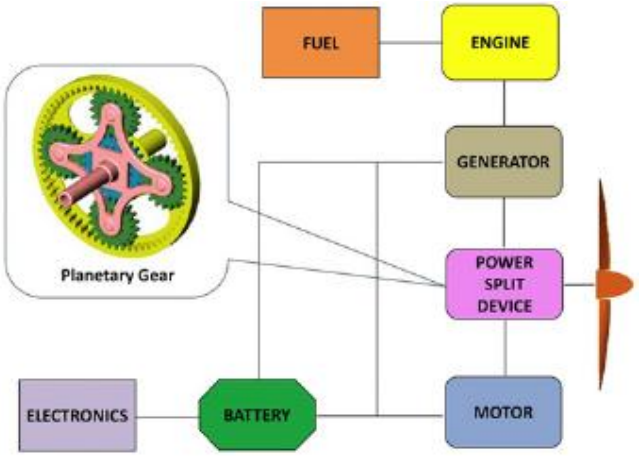

Figure 21: Hybrid Power split configuration with Planetary Gear, [28]

2.5 Composite Materials: Usage in Aeronautics and Mechanics

2.5.1 Advantages brought to the aeronautical industry

Composite materials find their greatest strengths within their high specific stiffness, high specific strength, good fatigue performance and the fact of allowing the construction of components of great geometric complexity. All mentioned advantages are required material properties in applications such as UAVs. Other advantages of composites over metal components are, [30]:

- excellent corrosion resistance;
- reduced machining;
- the ability to fabricate tapered sections and intricate contoured parts;
- the ability to orient reinforcement fibres in the direction of maximum stiffness and strength;
- the reduced number of assemblies and fasteners needed when using co-cure or co-consolidation composite manufacturing processes.
- low radar and microwave absorption of composites, which provides stealth capabilities, making radar detection difficult;
- very low thermal expansion reducing operational problems in high altitude flight.

Besides speaking solely of the aircraft's fuselage, the fabrication of fuel and oxidant reservoirs in fuel cells with composite materials could also be discussed.

2.5.2 Mechanics of Composite Materials

The desired properties of a composite material are obtained through a combination of the fibre-matrix reinforcement. Parameters such as the number of layers used, layer orientation and quantity of material will determine the final mechanical properties of a composite material.

The requirement of several layers comes from the fact that unidirectional composites find a higher stiffness along the fibre direction, while having a lower stiffness transversely. This is due to the fact that fibre mechanical properties are far superior when compared with the ones of resin. That said, it is of the upmost importance to align the fibres along the most demanding directions. That can be achieved by the use of layers that comprise fibres in more than one direction, as well as several layers of unidirectional fibres.

This section provides an overall understanding on how to determine the elastic mechanical properties of a composite material, taking into account the mechanical properties of the constituent materials. It is divided in the study of the Micromechanical behaviour of a lamina, and the Macromechanical behaviour of the Laminate, two or more *laminae* bonded together to act as a structural element. Below is a definition of both behaviour approaches, provided by [31].

Micromechanics

"The study of composite material behaviour wherein the interaction of the constituent materials is examined in detail as part of the definition of the behaviour of the heterogeneous composite material." (see Figure 22)

Macromechanics

"The study of composite material behaviour wherein the material is assumed homogeneous and the effects of the constituent materials are detected only as averaged apparent properties of the composite material." (see Figure 23)

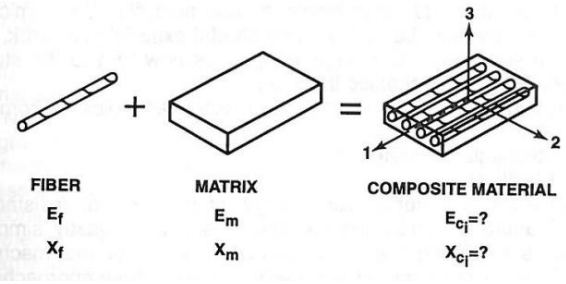

Figure 22: Basic question of micromechanics, [31]

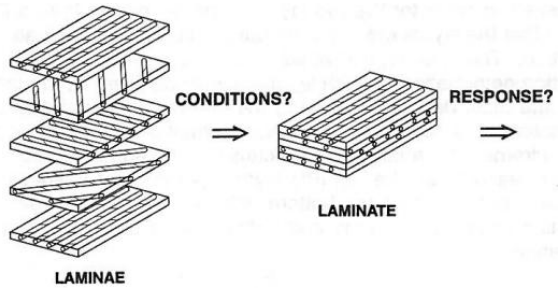

Figure 23: The basic question of laminate analysis, [31]

Micromechanical Behaviour of a Lamina

Approaches to micromechanics seek to determine elastic modulus or stiffnesses or compliances of a composite material in terms of the elastic modulus of the constituent materials, [31]. For that matter, the following fibre and matrix properties must be known:

- The Young's modulus of the isotropic fibre, E_f, and matrix, E_m;
- The Poisson's ratio of the isotropic fibre, ,υ_f, and matrix, υ_m;
- The fibre and matrix Volume Fractions, V_f and V_m, respectively, defined below, along with the relation between the two:

$$V_f = \frac{Fibre\ Volume}{Total\ Volume\ of\ Composite\ Material} \qquad V_m = \frac{Matrix\ Volume}{Total\ Volume\ of\ Composite\ Material}$$

$$V_f = (1 - V_m)$$

Rule of Mixtures

The properties of each layer can be obtained through the law of mixtures, whether it is along fibre direction or transversely. A brief description on how to determine the Young's modulus for both directions, E_1 and E_2, follows:

Determination of E_1

A brief description on how to determine the Young's modulus, E_1, follows. Figure 24 depicts a representative volume when load is occurring in the 1-direction, i.e., in the fibre direction. From the same figure, it is also possible to understand that strain will be the same for both fibre and matrix, thus Equation 2.35.

$$\varepsilon_1 = \frac{\Delta_l}{l}$$ Equation 2.35

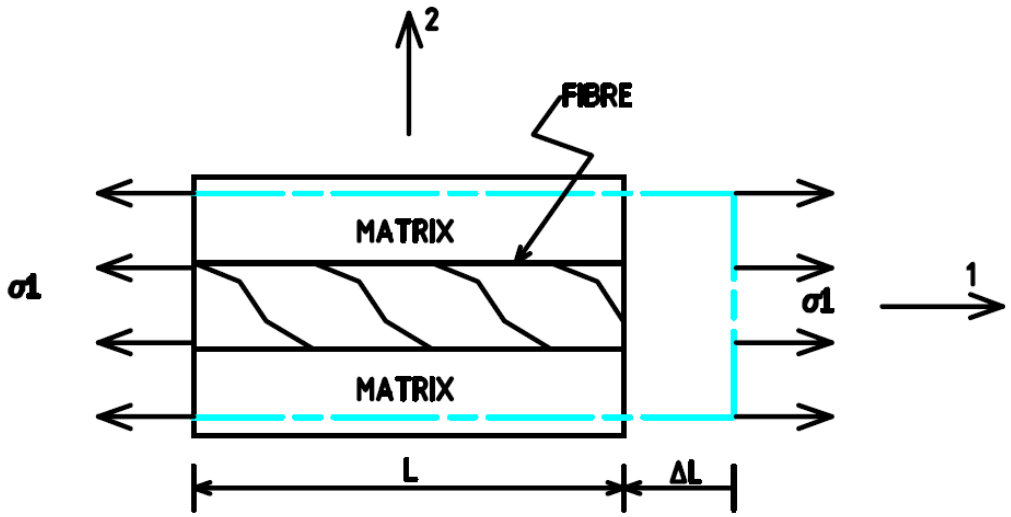

Figure 24: Representative Volume Element Loaded in the 1-Direction, [31]

If both constituent materials behave elastically, than the stresses are, as in Equation 2.36.

$$\sigma_f = E_f \varepsilon_1 \qquad \sigma_m = E_m \varepsilon_1 \qquad \text{Equation 2.36}$$

The resultant force on the representative volume element is the result of the stress, σ_1, acting on the cross-section area, A. However, that is the result of the sum of the σ_f acting on the cross-sectional area of the fibres, A_f, with the σ_m acting on the cross-sectional area of the matrix, A_m, as inEquation 2.37.

$$P = \sigma_1 A = \sigma_f A_f + \sigma_m A_m \qquad \text{Equation 2.37}$$

Substitution of Equation 2.36 in Equation 2.37, and recalling the Hooke's law in macromechanics, as in Equation 2.38, results in Equation 2.39.

$$\sigma_1 = E_1 \varepsilon_1 \qquad \text{Equation 2.38}$$

$$E_1 = E_f \frac{A_f}{A} + E_m \frac{A_m}{A} \qquad \text{Equation 2.39}$$

Since the Volume fractions can also be written as in Equation 2.40, the Rule of Mixtures is achieved in Equation 2.41.

$$V_f = \frac{A_f}{A} \qquad V_m = \frac{A_m}{A} \qquad \text{Equation 2.40}$$

$$E_1 = E_f V_f + E_m V_m \qquad \text{Equation 2.41}$$

Thus determining the Young's modulus of the composite material in the fibre direction.

Determination of E_2

Determination of the apparent Young's modulus, E_2, of the composite material is as follows.

Figure 25 depicts the representative volume element with loading occurring the direction 2, i.e., transversely to fibre direction.

In this case, no assumption can be made regarding strain in fibre and matrix, however σ_2 is thought to be applied on both fibre and matrix, as in Figure 25.

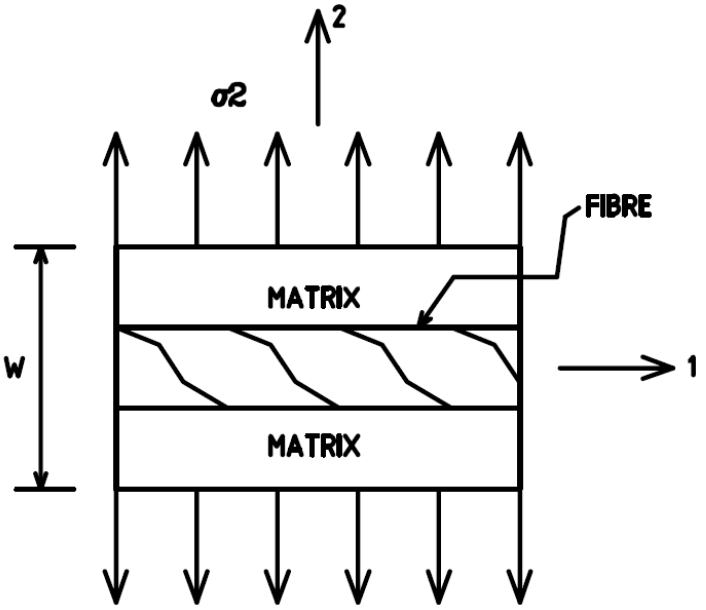

Figure 25: Representative Volume Element in the 2-direction, [31]

The resulting ε_f and ε_m from the stresses are as in Equation 2.42.

$$\varepsilon_f = \frac{\sigma_2}{E_f} \qquad \varepsilon_m = \frac{\sigma_2}{E_m} \qquad \text{Equation 2.42}$$

The total transverse deformation is ε_2 multiplied by the width, W, which in turn must take into account the ε_f acting on $V_f W$ and ε_m acting on $V_m W$, as in Equation 2.43.

$$\Delta W = \varepsilon_2 W = V_f W \varepsilon_f + V_m W \varepsilon_m \qquad \text{Equation 2.43}$$

Which can be transformed into Equation 2.44.

$$\varepsilon_2 = V_f \varepsilon_f + V_m \varepsilon_m \qquad \text{Equation 2.44}$$

Which, upon substitution from Equation 2.42, becomes in Equation 2.45.

$$\varepsilon_2 = V_f \frac{\sigma_2}{E_f} + V_m \frac{\sigma_2}{E_m} \qquad \text{Equation 2.45}$$

From the stress-strain relation, as in Equation 2.46.

$$\sigma_2 = E_2 \varepsilon_2 = E_2 \left[\frac{V_f \sigma_2}{E_f} + \frac{V_m \sigma_2}{E_m} \right] \qquad \text{Equation 2.46}$$

Thus, finally reaching the relation for E_2, as in Equation 2.47.

$$E_2 = \frac{E_f E_m}{V_m E_f + V_f E_m} \qquad \text{Equation 2.47}$$

The previous model is however a poor estimate, [32]. For that purpose, a semi-empirical expression, the Halpin-Tsai, is a more successful one, as seen in Equation 2.48.

$$E_2 = \frac{E_m (1 + \eta V_f)}{1 - \eta V_f} \qquad \text{Equation 2.48}$$

Where η can be obtained from Equation 2.49.

$$\eta = \frac{\frac{E_f}{E_m} - 1}{\frac{\mathrm{E_f}}{\mathrm{E_m}} + 1}$$ Equation 2.49

Ply coordinate system

Figure 26 depicts a unidirectional ply, with the fibre placed along the 1-direction. From the same figure, and considering the previous discussion over the rule of mixtures, it is easily understood that the mechanical properties of the depicted composite ply are not the same in all 3 given directions. The 1-direction must have better mechanical properties, since the fibres are placed along that direction, while the 2- and 3-directions, being transverse to fibre direction should have worse. In fact, being both previously mentioned directions transverse to fibre orientation, proves that in the plane they comprise, elastic properties are the same no matter the direction, meaning that the 23-plane is an isotropic one. Having one plane of isotropy, means that this composite ply is considered to be a transversely isotropic material.

Since only unidirectional plies will be handled in this report, this analysis will solely focus on transversely isotropic materials.

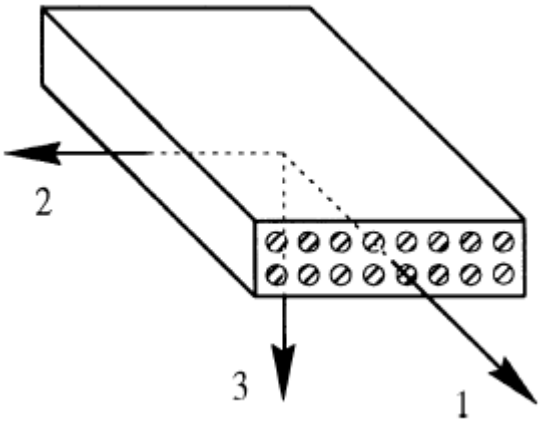

Figure 26: 123-coordinate system; unidirectional ply with the plane of isotropy 23, [31]

The stress-strain relations of an anisotropic material can be expressed in the form of Equation 2.50.

$$\{\sigma\}_{123} = [C]\{\varepsilon\}_{123}$$ Equation 2.50

Where $[C]$ is the stiffness matrix. The inverse relation in terms of a compliance matrix, $[S]$, is as in Equation 2.51.

$$\{\varepsilon\}_{123} = [S]\{\sigma\}_{123}$$ Equation 2.51

Where $[S] = [C]^{-1}$

Table 6 comprises the compliance matrix of an isotropic material on the left, and the compliance matrix of an transversely isotropic on the 23-plane on the right.

Having knowledge of the engineering constants E_1, shear constant in the 12-plane, G_{12}, either υ_{12} or υ_{21}, and any two of E_2, G_{23}, and υ_{23}, the rest can be determined using the relations on the bottom right corner of Table 6.

Table 6: Compliance matrixes of isotropic (left) and transversely isotropic (right) materials

Isotropic Compliance Matrix	Transversely Isotropic Compliance Matrix
$[S] = \begin{bmatrix} S_{11} & S_{12} & S_{13} & 0 & 0 & 0 \\ S_{12} & S_{22} & S_{23} & 0 & 0 & 0 \\ S_{13} & S_{23} & S_{33} & 0 & 0 & 0 \\ 0 & 0 & 0 & S_{44} & 0 & 0 \\ 0 & 0 & 0 & 0 & S_{55} & 0 \\ 0 & 0 & 0 & 0 & 0 & S_{66} \end{bmatrix}$	$[S] = \begin{bmatrix} S_{11} & S_{12} & S_{12} & 0 & 0 & 0 \\ S_{12} & S_{22} & S_{23} & 0 & 0 & 0 \\ S_{12} & S_{23} & S_{22} & 0 & 0 & 0 \\ 0 & 0 & 0 & 2(S_{22}-S_{23}) & 0 & 0 \\ 0 & 0 & 0 & 0 & S_{66} & 0 \\ 0 & 0 & 0 & 0 & 0 & S_{66} \end{bmatrix}$
$[S] = \begin{bmatrix} \frac{1}{E_1} & -\frac{\upsilon_{21}}{E_2} & -\frac{\upsilon_{31}}{E_3} & 0 & 0 & 0 \\ -\frac{\upsilon_{12}}{E_1} & \frac{1}{E_2} & -\frac{\upsilon_{32}}{E_3} & 0 & 0 & 0 \\ -\frac{\upsilon_{13}}{E_1} & -\frac{\upsilon_{23}}{E_2} & \frac{1}{E_3} & 0 & 0 & 0 \\ 0 & 0 & 0 & \frac{1}{G_{23}} & 0 & 0 \\ 0 & 0 & 0 & 0 & \frac{1}{G_{31}} & 0 \\ 0 & 0 & 0 & 0 & 0 & \frac{1}{G_{12}} \end{bmatrix}$	$E_2 = E_3$ $G_{12} = G_{31}$ $G_{23} = \frac{E_2}{2(1+\upsilon_{23})}$ $\upsilon_{23} = \upsilon_{32}$ $\upsilon_{12} = \upsilon_{13}$ $\upsilon_{21} = \upsilon_{31}$ $\frac{\upsilon_{12}}{E_1} = \frac{\upsilon_{21}}{E_2}$

Plane Stress State

In plane stress state analysis for composite plies and laminates, the ply/laminate plane (the 12-plane in Figure 26) is typically assumed, [33]. Normal stress component perpendicular to the mentioned plane and the transverse shear stresses are zero, which means:

$$\begin{cases} \sigma_3 = 0 \\ \tau_{23} = 0 \\ \tau_{31} = 0 \end{cases}$$ Equation 2.52

$$\begin{Bmatrix} \varepsilon_1 \\ \varepsilon_2 \\ \varepsilon_3 \\ \gamma_{23} \\ \gamma_{31} \\ \gamma_{12} \end{Bmatrix} = \begin{bmatrix} S_{11} & S_{12} & S_{12} & 0 & 0 & 0 \\ S_{12} & S_{22} & S_{23} & 0 & 0 & 0 \\ S_{12} & S_{23} & S_{22} & 0 & 0 & 0 \\ 0 & 0 & 0 & 2(S_{22}-S_{23}) & 0 & 0 \\ 0 & 0 & 0 & 0 & S_{66} & 0 \\ 0 & 0 & 0 & 0 & 0 & S_{66} \end{bmatrix} \begin{Bmatrix} \sigma_1 \\ \sigma_2 \\ 0 \\ 0 \\ 0 \\ \tau_{12} \end{Bmatrix}$$ Equation 2.53

Deleting the resulting zero elements from the 6 by 6 compliance matrix, results in a 3 by 3 matrix, as in Equation 2.54.

$$\{\varepsilon\}_{12} = [S]\{\sigma\}_{12}$$ Equation 2.54

The elements of the stiffness matrix in the plane stress state are however not equal to the elements of $[C]$ for general three-axial stress state. This is due to the fact that ε_3 is not zero.

For that matter, the stiffness matrix in plane stress state is denoted by $[Q]$.

The constitutive equations are written as:

$$\{\sigma\}_{12} = [Q]\{\varepsilon\}_{12} \qquad \text{Equation 2.55}$$

Where:

$$\begin{Bmatrix}\sigma_1\\ \sigma_2\\ \tau_{12}\end{Bmatrix} = \begin{bmatrix}Q_{11} & Q_{12} & 0\\ Q_{12} & Q_{22} & 0\\ 0 & 0 & Q_{66}\end{bmatrix}\begin{Bmatrix}\varepsilon_1\\ \varepsilon_2\\ \gamma_{12}\end{Bmatrix} \qquad \text{Equation 2.56}$$

Macromechanical behaviour of a laminate

Now thinking of the macromechanical system, a brief description on how to determine the elastic properties of a laminate follows.

Firstly, laminate coordinate system definition is in order. As seen in Figure 27, the laminate coordinate system is constituted by the axes x, y, and z. The $x-$ and $y-$axes define the plane of the laminate, and the $z-$axis is thus normal to this plane.

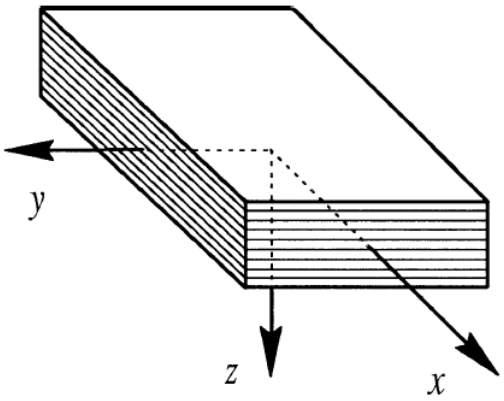

Figure 27: Laminate coordinate system xyz, [33]

In order to take into account the contribution of each layer to the laminate, there must be a distinction between them. In order to do so, it is first necessary to establish a layer numbering convention [33], as depicted in Figure 28, where the number of layers of the laminate is n, the thickness of the laminate, h. Furthermore, the top layer is considered to be layer number 1, and the bottom one, layer number n. Moreover, the $z-$coordinates of the top and bottom surfaces of a given k'th layer are z_{k-1} and z_k, respectively.

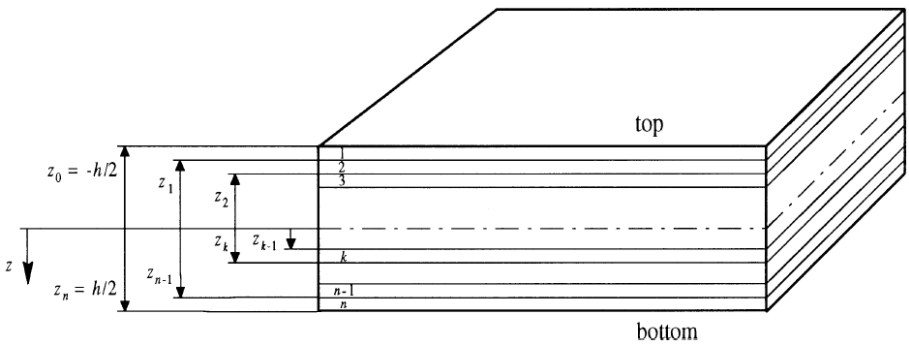

Figure 28: Layer and layer interface numbering convention for laminates, [33]

So as to consider the orientation of each layer, notation for that parameter is also required. Figure 29 depicts the notation for layer orientation, where θ is the rotation angle in the xy −plane.

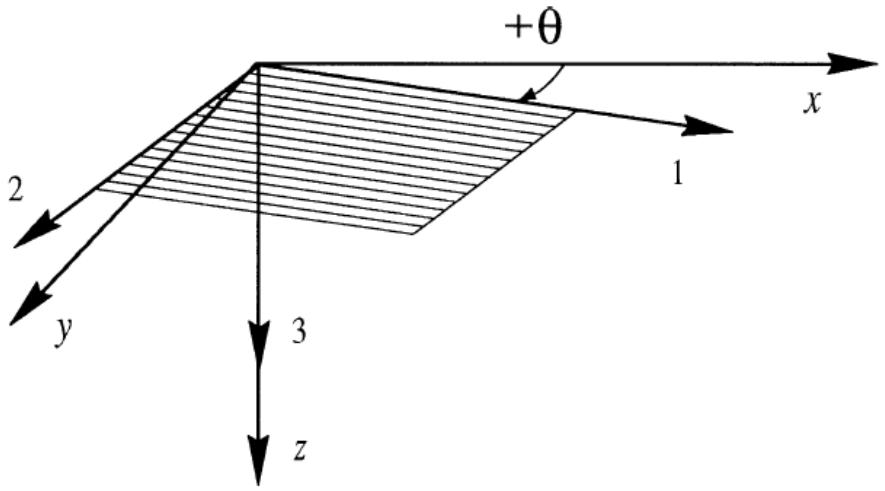

Figure 29: Rotation of layer axes notation, [33]

Remembering the stiffness matrix of plane stress in the 123 coordinate system, now comes the time to define a similar matrix considering the xyz-coordinate system, as well as taking into account layer orientation, for each layer. The result is the layer stiffness matrix, $[\bar{Q}]_k$, and can be obtain through the transformation equation below:

$$[\bar{Q}]_k = [T]_k^{-1}[Q][T]_k^{-T} \quad \text{Equation 2.57}$$

Where $[T]_k$ is the transformation matrix for the layer k.

Strain-Displacement Relations

The laminate stress-strain relations can be stated in terms of stiffnesses as in Equation 2.58.

$$\begin{Bmatrix} N \\ M \end{Bmatrix}_{xy} = \begin{bmatrix} A & B \\ B & D \end{bmatrix} \begin{Bmatrix} \varepsilon^0 \\ \kappa \end{Bmatrix}_{xy} \quad \text{Equation 2.58}$$

Where N and M are the in-plane forces (forces per width corresponding to the stress state in the laminate) and moments (defined in a similar way to the previous; moment effect on the laminate stresses), respectively. The ε^0 and κ are the laminate strains and curvature, respectively.

The $[A]$, $[B]$ and $[D]$ in the relation above are the in-plane, coupling and flexural stiffness matrices, respectively, and can be determined as demonstrated in Equation 2.59, Equation 2.60, and Equation 2.61.

$$[A] = \int_{-h/2}^{h/2} [\overline{Q}]_k dz \quad \text{Equation 2.59}$$

$$[B] = \int_{-h/2}^{h/2} [\overline{Q}]_k \, z \, dz \quad \text{Equation 2.60}$$

$$[D] = \int_{-h/2}^{h/2} [\overline{Q}]_k \; z^2 \, dz$$ Equation 2.61

The three matrices can be combined into a 6 by 6 stiffness matrix of the laminate.

The laminate stress-strain relations can also be stated in terms of compliances, which leads to Equation 2.62.

$$\begin{Bmatrix} \varepsilon^0 \\ \kappa \end{Bmatrix}_{xy} = \begin{bmatrix} a & b \\ b & d \end{bmatrix} \begin{Bmatrix} N \\ M \end{Bmatrix}_{xy}$$ Equation 2.62

Where, in turn, $[a]$, $[b]$ and $[d]$ are the in-plane, coupling, and flexural compliance matrices of the laminate. The combined compliance matrix is the inverse of the 6 by 6 stiffness matrix, as in Equation 2.63.

$$\begin{bmatrix} a & b \\ b & d \end{bmatrix} = \begin{bmatrix} A & B \\ B & D \end{bmatrix}^{-1}$$ Equation 2.63

Normalized stiffness and compliance matrices

In order to reach the in-plane engineering constants of a laminate, one has to achieve the normalized in-plane, $[a^*]$, coupling, $[b^*]$, and flexural, $[d^*]$, compliance matrices of the laminate, which can be written in terms of the normalized stresses, as in Equation 2.64.

$$\begin{Bmatrix} \sigma^0 \\ \sigma^f \end{Bmatrix}_{xy} = \begin{bmatrix} a^* & \frac{1}{3} b^* \\ (b^*)^T & d^* \end{bmatrix} \begin{Bmatrix} \varepsilon^0 \\ \varepsilon^f \end{Bmatrix}_{xy}$$ Equation 2.64

So as to obtain the normalized matrices, the normalization procedure for each of the matrices is as follows:

$$[a^*] = h[a] \qquad [b^*] = \frac{h^2}{2}[b] \qquad [d^*] = \frac{h^3}{12}[d]$$

Laminate Engineering Constants

Finally, attainment of the in-plane engineering constants of a laminate can be performed using the analogy between the ply compliance matrix (see Table 6) and the normalized in-plane compliance matrix of a laminate.

$$E_x = \frac{1}{a_{11}^*} \qquad E_y = \frac{1}{a_{22}^*} \qquad G_{xy} = \frac{1}{a_{66}^*}$$

$$\nu_{xy} = -\frac{a_{12}^*}{a_{11}^*} \qquad \nu_{yx} = -\frac{a_{12}^*}{a_{22}^*}$$

2.6 UAV review

Increased development of UAV systems took place in the end of the 20th Century, focusing on military applications. Surveillance, reconnaissance and detection were foreseen as the main applications for UAVs, however, over the past few years, a broad range of possible missions for UAV systems has been made possible, following a wide array of available sizes with maximum take-off weights (MTOWs) ranging from nano-scale (0,025 kg) to considerable scales of 10.000 kg.

Research conducted by Frost & Sullivan, mentioned in the European Commission report [34], shows an increase of 1 000 to 5 000 in the number of UAVs deployed globally between the years of 2004 to 2008. The greatest contributor to this growth were the United States (US), whose budget and current need is larger than any other country or region in the world, [34].

Forecasted future investment on military Unmanned Aerial Systems (UAS) by the EU and the US is show in Chart 1.

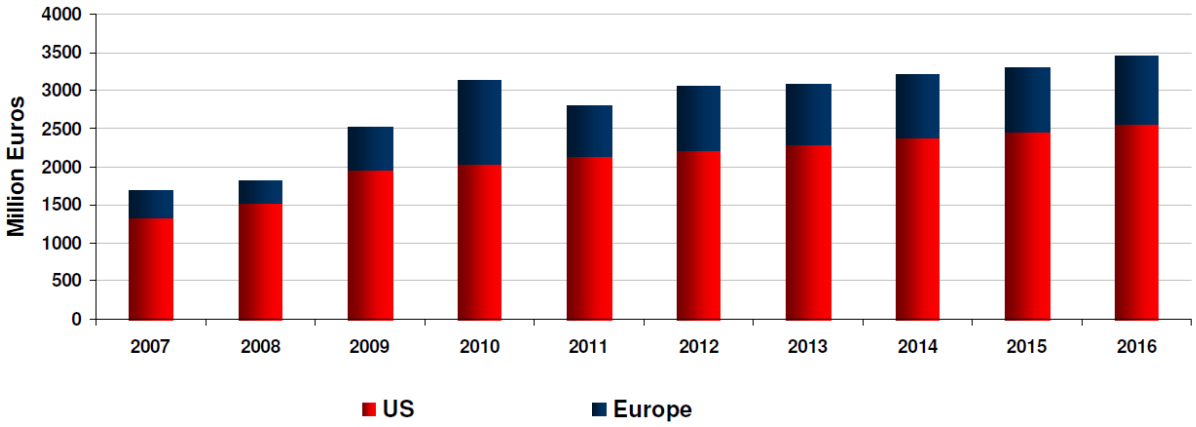

Chart 1: Expenditure on Military UAS (Europe and the USA), 2007-2016, [34]

Until recently, military applications, such as the previously foreseen mentioned ones, as well as support and intervention in theatres of war, have been the developing drive. However, the technology has become increasingly interesting for civilian and commercial purposes, such as forest fire surveillance, law enforcement (e.g., border control, coast guard), as well as research and monitoring.

2.6.1 UAV Categorization

According to UVS international, UAS are categorized according to performance parameters, such as the following:

- MTOW: The maximum take-off weight is the maximum weight for which all airworthiness, i.e., safe flight, requirements are ensured for the aircraft to take-off.
- Payload: defined by the cargo (e.g., sensors; cameras) capacity of the aircraft
- Endurance: parameter defined as the maximum flight time;
- Speed: cruise, loiter or maximum speed impact on both the time to station and the hourly acquisition rate (the area a UAS can swift in one hour), assuming the sensor package does not limit performance.
- Range: Range is the maximum distance the aircraft can travel between take-off and landing, and it comes as a function of variation of aircraft weight (fuel), engine specific fuel consumption and aerodynamic configuration.

UVS International constructed a categorization of UAS, according to the previously performance features, given in Table 7.

Table 7: Categorization for UAS, UVS International

UAS Categories		Acronym	Endurance (h)	Range (km)	Flight Altitude (m)	MTOW (kg)
Tactical	Nano	**Nano**	<1	<1	100	<0,025
	Micro	**Micro**	1	<10	250	<5
	Mini	**Mini**	<2	<10	300	<30
	Close Range	**CR**	2 to 4	10 to 30	3000	150
	Short Range	**SR**	3 to 6	30 to 70	3000	200
	Medium Range	**MR**	6 to 10	70 to 200	5000	1250
	Medium Range Endurance	**MRE**	10 to 18	>500	8000	1250
	Low Altitude Deep Penetration	**LADP**	0,5 to 1	>250	50 to 9000?	350
	Low Altitude Long Penetration	**LALE**	>24	>500	3000	<30
	Medium Altitude Long Endurance	**MALE**	24 to 48	>500	14000	1500
Strategic	High Altitude Long Endurance	**HALE**	24 to 48	>2000	20000	12000
Special Purpose	Unmanned Combat Aerial Vehicle	**UCAV**	2	1500	10000	10000
	Lethal	**LETH**	3 to 4	300	4000	250
	Decoy	**DEC**	<4	0 to 500	5000	250
	Stratospheric	**STRATO**	>48	>2000	20k to 30k	tbd
	Exo-Stratospheric	**EXO**	tbd	tbd	>30000	tbd
	Space	**SPACE**	tbd	tbd	tbd	tbd

2.6.2 Civil application of UAVs

According to Frost & Sullivan [34], the European civilian UAV market is currently small. However it is expected to grow significantly over the next ten years, as seen from Chart 2.

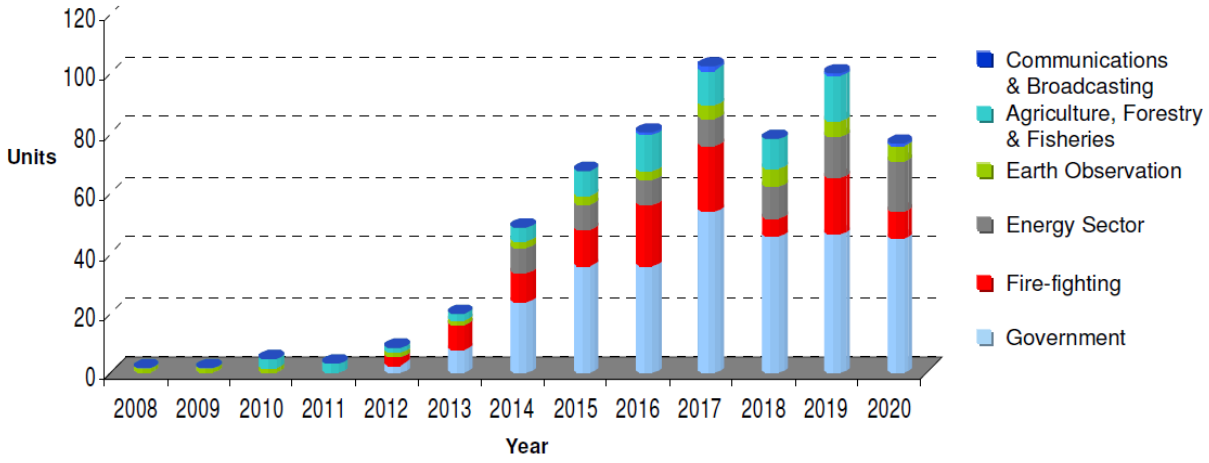

Chart 2: European civil and commercial UAV market. Total Market by vertical segment, 2008-2020, [34]

Furthermore, development is expected to occur within different governmental and commercial segments, as depicted in List 1.

Government
- Law enforcement (Police, Civil Security)
- Border security
- Coastguard

Fire Fighting and Emergency Services
- Forest fires
- Other major incidents
- Emergency rescue (e.g., Mountain rescue)

Energy Sector
- Oil and gas industry distribution infrastructure
- Electricity grids / distribution networks

Agriculture Forestry and Fisheries
- Environmental monitoring
- Crop dusting
- Optimising use of resources (water, fertilizers)

Earth Observation and Remote Sensing
- Climate monitoring
- Aerial photography mapping and surveying
- Seismic events
- Major incident and pollution monitoring

Communications and Broadcasting
- VHALE platforms as proxy-satellites
- MALE / S/MUAS as short-term, local communications coverage

List 1: UAV application by market segment, [34]

2.7 Goal of this Dissertation

Having gathered the necessary information regarding UAV state of the art propulsive systems, and withdrawn the required conclusions, it is now possible to formulate an hypothesis to address the objective proposed in Section 1.: assess the feasibility, from a technological perspective (i.e., not considering costs), of a Fuel Cell based propulsive system for a UAV. The hypothesis of this dissertation is formulated, taking into account six considerations regarding UAV propulsion that follow.

1. Considering that the efficiency of a Fuel cell system is almost 2 times bigger than that of an ICE and that a PEM FC shows a 60% efficiency (confirmed by the PM catalogue: >52% efficiency, as in [35]), along with the 95% efficiency of the Launch Point Halbach Array Motor.
    a) $\eta_{FCoverall} = \eta_{EM} \cdot \eta_{FC} \cdot \eta_{Propeller}; \eta_{EM} = 0{,}95;\ \eta_{FC} = 0{,}60;$
    b) $\eta_{ICEoverall} = \eta_{ICE} \cdot \eta_{Propeller}; \eta_{ICE} = 0{,}30$
2. Considering that the Specific Energy contained in a H_2 vessel at 700 bar reaches 33,3 kWh/kg, according to [26];
3. Considering a possible Electric Motor (EM) with a weight of 3 kg. This assumption occurred because of the 7 HP Launch Point Halbach Array EM (available in Annexe D). The EM achieves 7 HP ≈ 5,2 kW weighing only 0,645 kg. Since Launch Point does not provide EM with the required power, an assumption of 3 kg mass was assumed it the EM were to achieve 20 kW;
4. Considering the implementation as the propulsive system of an Unmanned Aircraft with a Maximum Take-off Weight (MTOW) of 210 kg; 70 kg of which are available to the propulsive system. The power required for take-off is about 20 kW. This information was based on previous projects done by INEGI on an aircraft of similar dimensions and MTOW;
5. Considering that, as mentioned in Table 5, the DOE targets for system gravimetric capacity, wt%, i.e., the targets for stored mass of hydrogen per total system storage mass ($m_{H_2}/m_{storage}$) are as follows:
    a) The wt% in 2015 should be 5,5%;
    b) The ultimate target for the wt% is 7,5%;
6. Finally, considering the total FC mass, as well as End Plate mass weight in the total stack mass. It be should noted that, no Fuel Cell systems catalogues with power of 20 kW were found online. An assumption of using 2 Proton Motor 8 kW, combined with a 4 kW, resulting in 20 kW in total power was made ($2 \times 8\,kW + 1 \times 4\,kW = 20\,kW$). Stack total mass is then 38,4 kg ($14{,}6\,kg \times 2 + 9.2\,kg = 38{,}4\,kg$), assuming an extra weight of 2,5 kg of BoP; results in 40,9 kg. The assumption of using 2 systems of 8 kW, combined with 1 of 4 kW, will naturally result in increased weight when facing one with 20 kW, since a larger system is expected to have lesser mass than a combination of smaller systems. Furthermore, one must take into account that the relative mass weight of the end plate in the total FC stack is 19% according to [3]. Since mass decrease improvements are expected in the bipolar plates, as already mentioned, the end plates are expected to have a greater significance in weight

distribution in the FC stack. Section 3 has further development on the reason for which this FC system was chosen.

From the six previous considerations, the following assumptions can be made:

1. Ratio of FC/ICE efficiencies: $\frac{\eta_{FCoverall}}{\eta_{ICEoverall}} = \frac{\eta_{EM} \cdot \eta_{FC} \cdot \eta_{Propeller}}{\eta_{ICE} \cdot \eta_{Propeller}} = \frac{0{,}90 \cdot 0{,}60 \cdot \eta_{Propeller}}{0{,}30 \cdot \eta_{Propeller}} = 1{,}8 \approx 2{,}0$;

Combining Bullets 2. and 5.:

- 2. (Specific Energy of 33,3 kWh/kg) and 5. (Gravimetric capacity, i.e., ratio of Hydrogen mass per mass of storage, wt%)
    - H_2 stored at 700 bar: 33,3 kWh/kg;
    - wt% (2015) = 5,5%: 1,832 kWh/kg (see Table 5);
    - wt% (ultimate) = 7,5%: 2,498 kWh/kg (see Table 5);
- 3. (EM) e 6. (FC weight)

From consideration 3. that foresees an Electric Motor with the required power of 20 kW to weigh 3 kg and consideration 6. that establishes the mass ratio in a FC.

    - 3 kg $_{(EM)}$ + 38,4 kg $(2 \times 8kW + 1 \times 4kW)$ $_{(FC)}$ + 2,5 kg $_{(FC\_BoP)}$;
- 4. (Aircraft: Available weight for propulsion)
    - $70 = 3\,kg\ (EM) + 40{,}9\,kg\ (FC) + x\,kg\ (Storage + Fuel)$;
    - $x = 26{,}1\,kg\ (Storage + Fuel)$
        - $26{,}1\,kg \times 2{,}55\,kWh/kg = 66{,}555\,kWh$
        - In the following calculation, the achieved energy can also be seen as if it was powering the propeller mechanical drain with roughly 12 kW for 5,5 h: $66{,}555\,kWh \approx 12\,kW \times 5{,}5\,h$.

Therefore, considering the 66,555 kWh of available energy, for the 70 kg mass of the propulsive system, $m_{propulsive}$, a Specific Energy of $950{,}786\,Wh/kg$ is achieved, as in Equation 2.65.

$$\text{Specific Energy} = \frac{\text{available energy}}{\text{m}_{\text{propulsive}}} \qquad \text{Equation 2.65}$$

However, this specific energy was obtained considering the mass of the currently used End Plates. The objective of this dissertation is then to ascertain whether the introduction of Composite Materials in the end plates can result in a sufficient mass reduction, in order to significantly increase the specific energy of the concerned FC propulsive system, and provide a comparison with a conventional type of fuel, such as a gasoline ICE propulsive system.

The specific energy of gasoline is $11{,}5\,kWh/kg$, which is clearly lower than of Hydrogen stored at 700 bar. However, its gravimetric capacity is *c.* $8\,kWh/kg$, i.e., the fuel mass over fuel storage system mass in gasoline systems is far greater than that of hydrogen, according to [26], causing it to have a far superior specific energy when considering the real practical system.

Fuel Cell systems require a stabilizing element for power peak stages during flight, such as take-off. That can be achieved through battery hybridization, i.e., the implementation of batteries for peak power instants, as shown from the literature review in Section 2.4. This fact was not taken into account on the hypothesis for this aircraft. This consideration would imply further study in the battery area, which was not possible to achieve. Furthermore, if

considered, the increased weight caused by the introduction of batteries, could possibly result in rendering FC systems unfit for current existing FC systems. Nevertheless, this could be avoided if a different take-off mechanism were to be considered. Such a mechanism would provide the necessary energy for take-off to the aircraft, making unnecessary the use of heavy batteries for the take-off power peak. The mechanism could be for instance a catapult or a tow system, the latter resembling current glider aircrafts.

3. Conceptual Development

This third section of the dissertation discusses the conceptual development path taken. It provides a description of the concepts, and all the required assumptions to proceed to the stage that follows.

The sketching of small to medium sized parts, as is the case of the parts dealt in this dissertation, on computer aided design is often easier if the length units are in millimetres. However, that fact naturally has its implications in many other dimensional properties, as e.g. mass coming in tonnes, rather than kilograms. For that reason, consistency in units is required and the commonly designated "MPa" unit system was used. Table 8 shows the required units to consider for several properties when using millimetres as a dimension for length.

Table 8: Table of consistent units

Property or Load	**SI (International System of Units)**	**"MPa" unit system**
Mass	$[kg]$	$[tonne]$
Length	$[m]$	$[mm]$
Time	$[s]$	$[s]$
Temperature	$[K]$	$[K]$
Velocity	$[m/s]$	$[mm/s]$
Acceleration	$[m/s^2]$	$[mm/s^2]$
Force	$[N]$	$[N]$
Moment	$[Nm]$	$[Nmm]$
Pressure	$[Pa]$	$[MPa]$
Density	$[kg/m^3]$	$[tonne/mm^3]$

3.1 Selected FC System

In order to properly consider every aspect required for Fuel Cell stack construction, an online catalogue search was carried out to find a suitable system for the propulsion of the concerned UAV. Proton Motor and Horizon were amongst the most credible manufacturers found, along as well as among the only ones identified with products producing enough power to be considered in the propulsion system for the UAV under study.

The systems considered were the H-5000, a 5 kW fuel cell, and the Proton Motor 8kW, both PEM type fuel cell systems. Even though these systems do no reach the required power of 20 kW, the hypothesis foresaw the use of multiple units, i.e., either four stacks of the H5000 or two of the Proton Motor 8kW, put together with the Proton Motor 4 kW, all adding up to 20 kW.

In the analysis performed, the Horizon H-5000 was found to be considerably heavier than the PM 8kW and, for that reason, he PM 8kW was chosen (see Figure 30).

The studied end plate was therefore one of the 8 kW systems, however one can assume that the same end plate is used for both systems.

Both FC system catalogues are available in the Annexes B and C.
The selected and henceforth considered Fuel Cell system was the Proton Motor 8kW with the following characteristics shown in Table 9.

Table 9: Proton Motor 8 kW features, [35]

Type	**Low Temperature PEM Fuel Cell**	
	4 kW	**8 kW**
Cells	48	96
Power (Rated/Peak)	4,0/4,4 kW	8,0/8,8 kW
Current (Rated/Peak)	130/150 A	
DC Voltage	27... 55 V	53… 110 V
Efficiency	> 52%	
Hydrogen quality	ISO 14687-2 / SAR J2719	
Operating pressure H2	400… 600 mbar	
Pressure process air (lower pressure is possible)	600 mbar	
$Width \times height \times length\ (Overall\ Dimensions)$	$246 \times 136 \times 247\ mm$	$246 \times 136 \times 432\ mm$
Mass	9,2 kg	14,6 kg
Operating Lifetime	Up to 5000 h	

Figure 30: The Proton Motor 8 kW Fuel Cell stack, [35]

3.2 Geometrical considerations and assumptions

Given that very specific and technical online information is either difficult to be found or simply unavailable, some assumptions had to be made in order to successfully produce a model. The assumptions taken regarding this matter are stated in this section.

3.2.1 Metal Plate Thickness and Mass, and Graphite Block Length

Metal plate dimensions

Following the width height dimensions given in Table 9, the metal plate's face was considered to have the following dimensions: 248×140. The general dimensions of the metal plate are depicted in Figure 31.

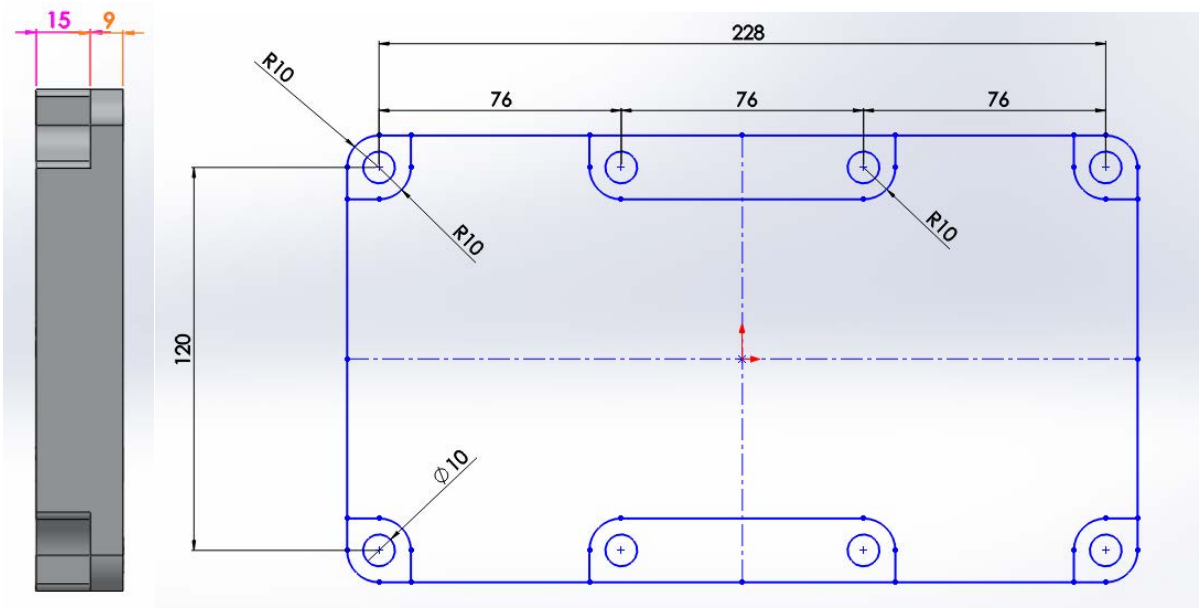

Figure 31: Metal plate general dimensions

The assumed general dimensions of the Metal End Plate were then $248 \times 140 \times 24\ mm^3$.

Graphite Block

The Graphite block is perceived as the assembly of the combined 96 unit cells.

Considering each unitary cell, containing two Bipolar Plates, to have 4 mm (which is an appropriate value to consider, since each bipolar plate is supposed to be less than 3 mm thick, [6]), and that this stack contains 96 cells, the total length results in 384 mm.

$$96\ cells \times 4\ mm/cell\ =\ 384\ mm$$

Knowing that the total length of this stack is 432 mm, the thickness of each End Plate should be 24 mm. Since:

$$\frac{432 - 384}{2\ End\ Plates} = 24\ mm/End\ Plate$$

Only half of the cell block will be modelled. Thus, the length of half the graphite block results in:

$$\frac{384\ mm}{2} = 192\ mm$$

In order to reach the assumption of the dimensions of the graphite block, a rule of dimension proportionality was considered, i.e., same height-width ratio for both metal end plate and graphite block.

$$\frac{width}{height} = \frac{248}{140} \approx 1{,}77$$

The first chosen dimensions were 177x100 mm, however the height coincided with the screw cut extrude region of the Metal End Plate. In order to avoid this situation, that would surely lead to stress concentration in that particular area, a height limitation for the graphite block was established. The height should then be smaller than 100 mm not to coincide with the stipulated dimensions. A height of 96 mm was established, and a width of 177 mm was maintained. The stipulated dimensions ($height \times width$) of the graphite block were then $177 \times 96\ mm$.

$$177\ mm \times 96\ mm = 17{,}7\ cm \times 9{,}6\ cm = 169{,}92\ \ cm^2$$

$$Cell\ Total\ Area = 169{,}92\ \ cm^2 \times 96\ cells = 16\ 312{,}32\ cm^2$$

$$\frac{8\ 000\ W}{16\ 312{,}32\ cm^2} = 0{,}490\ W/cm^2 = 490\ mW/cm^2$$

To see if the achieved specific power (W/cm^2) for each cell was suitable, an inquiry was made to an FC expert. A value of $450\ mW/cm^2$ was told to be customary for state-of-the-art FC systems.

A calculus of the required area to achieve a $450\ mW/cm^2$ is performed below:

$$\frac{8\ 000\ W}{0{,}450\ W/cm^2} = 17\ 777{,}778\ cm^2$$

$$A_{cell} = \frac{17\ 777{,}778\ cm^2}{96\ cells} = 185{,}185\ cm^2/cell = 0{,}0185185\ m^2/cell$$

$$1{,}77 \times y \times y = 0{,}0185185$$

$$height = y = 0{,}102286\ m \approx 102\ mm$$

$$width = x = 0{,}181046\ m \approx 181\ mm$$

Since there was no information regarding hole diameter size, some assumptions had to be made:

- Screw hole diameter, $\emptyset = 10\ mm$
- Fuel, oxidant and cooling holes diameter, $\emptyset = 10\ mm$

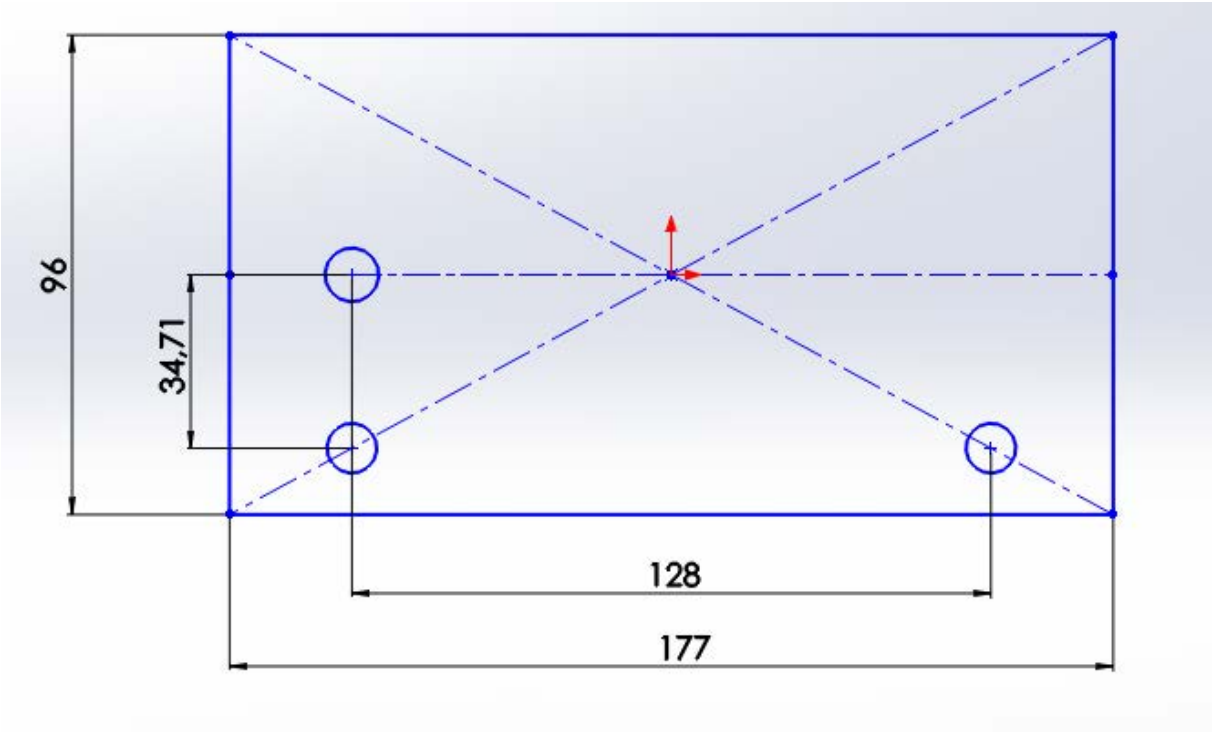

Figure 32: Assumed general dimensions for the graphite block and hole positioning

FC stack and Metal Plate mass assumption

As pointed out before, the PM 8kW differs for its low mass (14,6 kg), when compared to the Horizon H-5000 (30 kg). Table 10 contains the mass of the end plates for the two materials (steel and aluminium) used in the metal end plate, along with the mass ratio to the FC stack total mass. Having such a considerable low mass, one assumes that the PM 8kW must employ aluminium end plates in its FC stack, since steel end plates would imply that the end plates would weight almost 80% of the total stack mass, which is not reasonable (and distant from the typical values).

A mass ratio of 27% is found acceptable, considering the 19% mass ratio stated in [3]. Therefore, and hereinafter, the employed material for the PM 8kW and 4 kW end plates is considered to be aluminium, and all the final mass comparisons will be made taking this fact into account.

Table 10: Metal End Plate mass and mass ratio to FC stack total mass for aluminium and steel

Material	1 End Plate Mass (kg)	2 End Plate Mass (kg)	Mass ratio to FC stack total mass (%)
Steel	5,794	11,588	79,37
Aluminium	2,005	4,010	27,47

Figure 33 depicts a Solid Works rendering of the FC metal end plate stack with the considered dimensional assumptions.

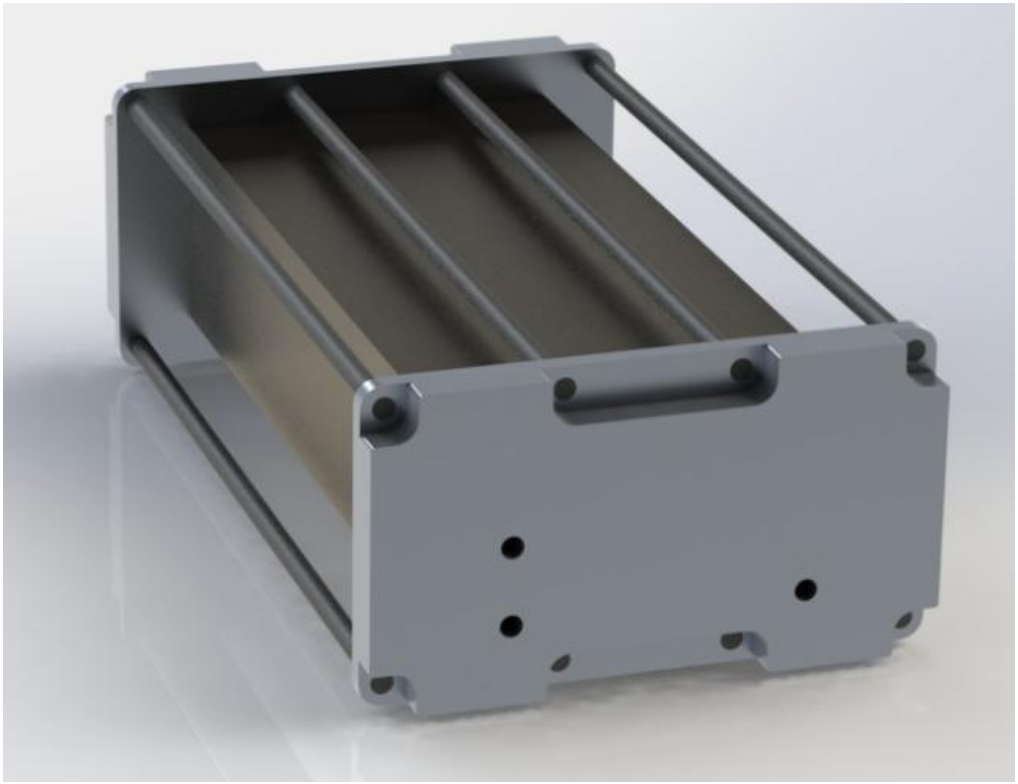

Figure 33: FC metal EP stack Solid Works rendering

3.2.2 Composite Plate Concepts

This subchapter describes the assumptions for the suggested composite end plate concepts.

Composite Layup

Since flexural strength is required along the $x-$ and $y-directions$, the chosen fibre orientations were 0º and 90º. Selected ply thickness was 0,200 mm, combining 50 plies, resulting in a plate with a thickness of 10 mm, as seen in Table 11.

Table 11: Composite ply thickness, stacking sequence and resulting plate thickness

Carbon/epoxy		
Ply thickness (mm)	Stacking Sequence	Plate thickness
0,200	$[0/90]_{25}$	10 mm

Composite Inserts

A hole in a composite reinforced polymer can be very harmful to the part's mechanical strength, since it disrupts fibres, *ergo* load transfer. Inserts for composite materials are often used as a way to distribute load and avoid stress concentration around the holes in a composite part. Knowing that the composite plates being dealt with in this project contain a significant amount of holes in them, considering inserts would not only be more beneficial to the stress and strain results, but would also pose as a more realistic approach to the model, though causing a harmful increase in End Plate weight. However, the author's lack of experience in handling Abaqus, combined with the time limitation, lead to leave this issue as an interesting subject to be discussed as future work. The proposed concepts modelled in FEM can then be seen as the worst possible case, since better results can be expected with the introduction of inserts. Figure 34 depicts a composite insert.

Figure 34: Composite Insert

Quantity of Holes in Plate

An issue that immediately came up was the number of plate holes for screw fixation. An uneven number of screws on each of the top and bottom sides, leading to the existence of plate fixation in the middle, is thought to assist in decrease stress and strain in the middle, though undermining composite strength. For that matter, all suggested composite concepts come with 10 holes (5 on top, 5 on the bottom), instead of the 8 holes of the metal plate.

Normal Plate

This plate was the first composite design thought upon and tested. Its name is due to its basic design (rectangular plate with similar dimensions to the metal end plate). Figure 35 depicts the dimensions of the normal plate, with hole positioning, as well as the contact surface of the normal plate with the graphite block (inner rectangle). It should be noted that hereinafter this will be the basic geometry of every composite concept, with the exception of the Inertia plate.

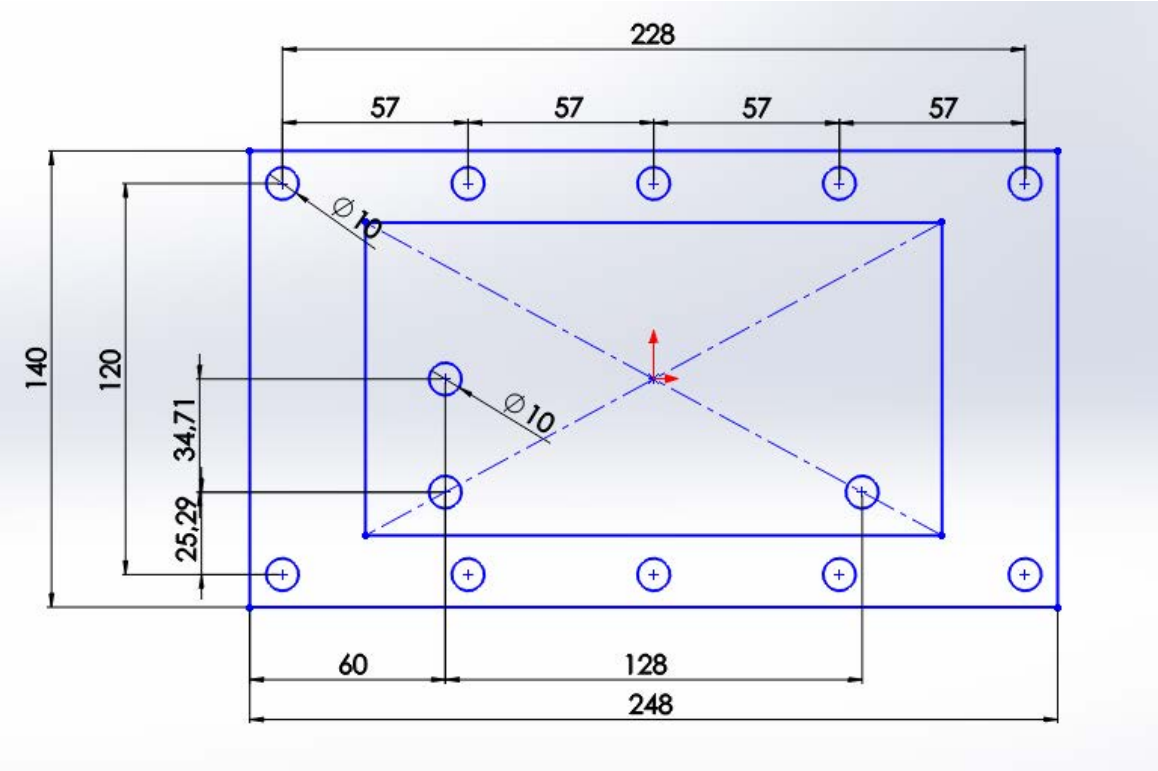

Figure 35: Normal plate dimensions. Positioning of holes and contact surface with graphite block (inside rectangle)

Figure 36 depicts a Solid Works rendering of the Normal plate, having a thickness of 10 mm.

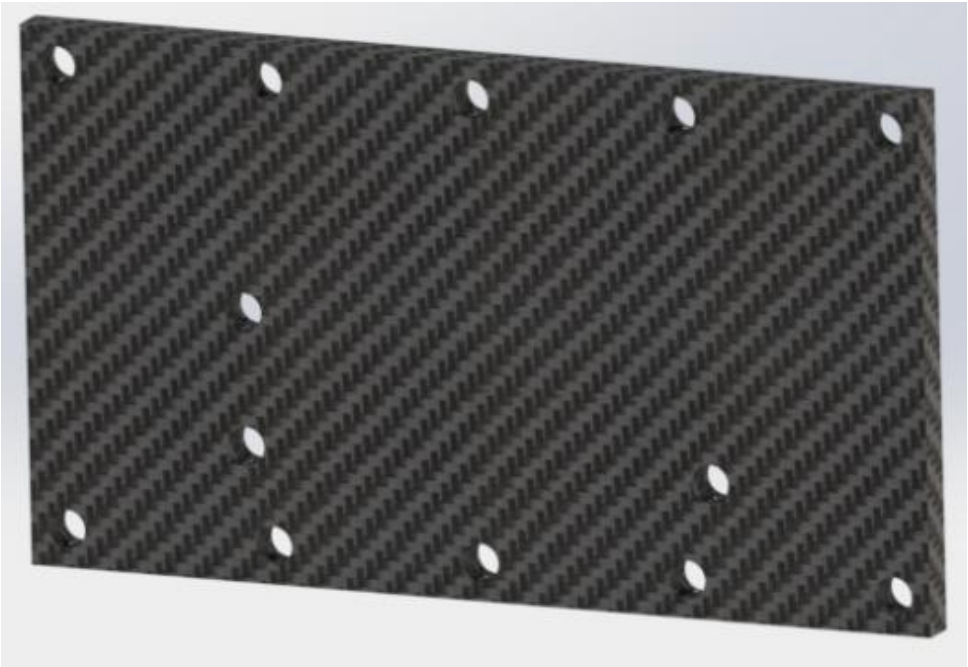

Figure 36: Normal plate with Solid Works rendering

Pre-curvature

This concept came up as a suggestion from Professor Dai Gil Lee from the Korea Advanced Institute of Science and Technology, as he had already performed work on this area, and with a similar concept.

An end plate with a pre-made curvature is seen as a possible way to resolve the non-uniform stress issue, for once the clamping force is performed, the plate is expected to deform and apply a uniform pressure to the fuel cell stack. A pre-curvature theoretical calculus should have been made prior to plate design, however, the calculus was said to be too demanding, as well as too time consuming. Since there is already conclusive literature on this issue, for an end plate with similar dimensions (100x200) to the ones being considered, a decision for the radius dimension was taken based on the results of the mentioned paper.

The plate that achieved the biggest uniformity was a plate comprising two types of composite materials: glass fibre-epoxy and carbon fibre-epoxy. Its details are shown in Table 12.

Table 12: Flexural Stiffness (EI), curvatures (R) of the best performer composite plate tested in [18]

Composite End Plate	Glass/epoxy		Carbon/epoxy		EI (Nm^2)	R (m)
	Stacking sequence	Thickness (mm)	Stacking sequence	Thickness (mm)		
	$[0/90/0]_{28}$	10,5	$[0/90/0]_6$	4,5	3782	10,52

The curvature is of 10,52 mm. For that matter, a curvature of 10 mm was chosen to the design of the pre-curvature plate used in this report.

Figure 37 and Figure 38 depict the curvature in the $y-z$ plane, and $x-z$ plane, respectively.

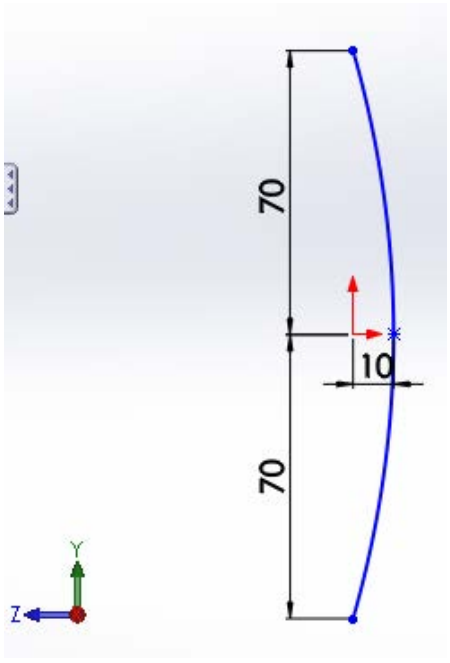

Figure 37: Pre-curvature plate curvature in the y-z plane

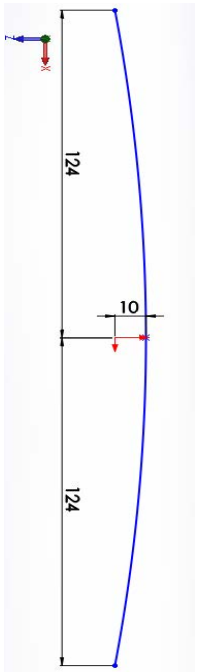

Figure 38: Pre-curvature plate curvature in the x-z plane

Figure 39 depicts a Solid Works render of the Pre-curvature plate.

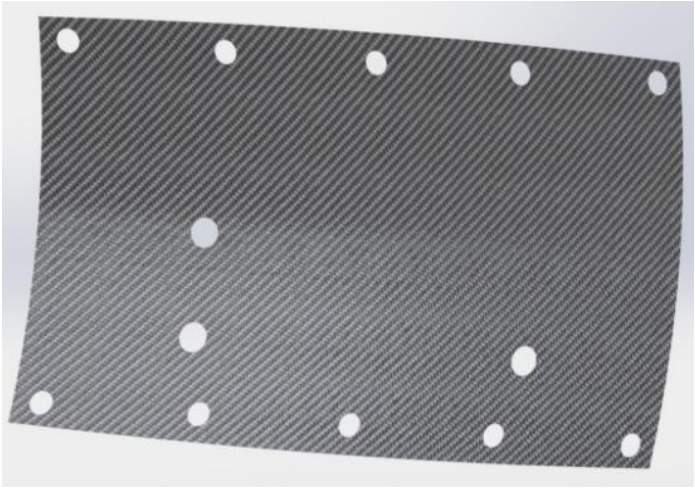

Figure 39: Pre-curvature plate sketched as surface

Shoe Box

This concept was thought upon as a good strategy to create a rigid cover. It was named because its basic concept consists of a conventional shoe box cover, as shown in Figure 40.

Figure 40: Conventional Shoe Box cover

This conceptual plate would have a carbon fibre supports, connecting the face to each of the perpendicular side faces for increased rigidity. These supports would be adhered to each surface through the use of an epoxy resin. Figure 41 is the result of a Solid Works rendering to demonstrate the thought-of concept.

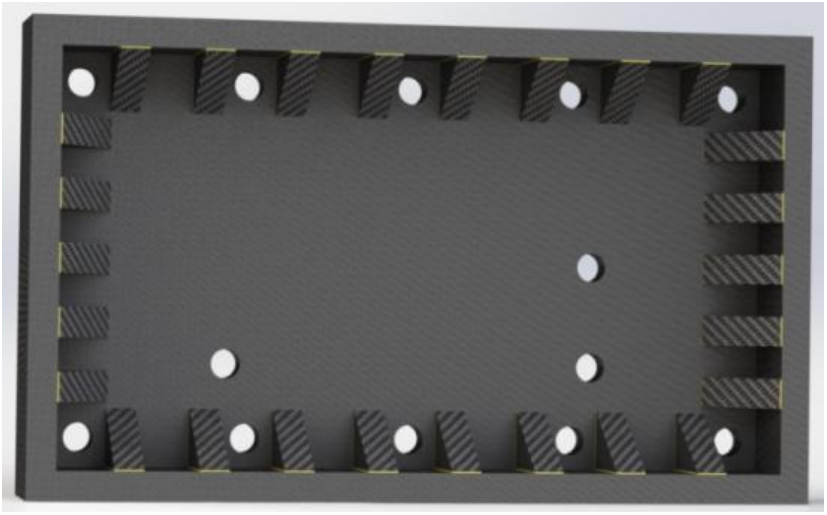

Figure 41: Shoe Box concept with Solid Works rendering

Supports

The whole assembly then consists of the Shoe Box cover, along with the adhesive contact and the supports. There are 8 supports separated by 28,5 mm along each horizontal face on the bottom and upper side, and 5 supports separated by 21,25 mm located on both vertical edges. Figure 42 shows the positioning of the supports in the shoe box face.

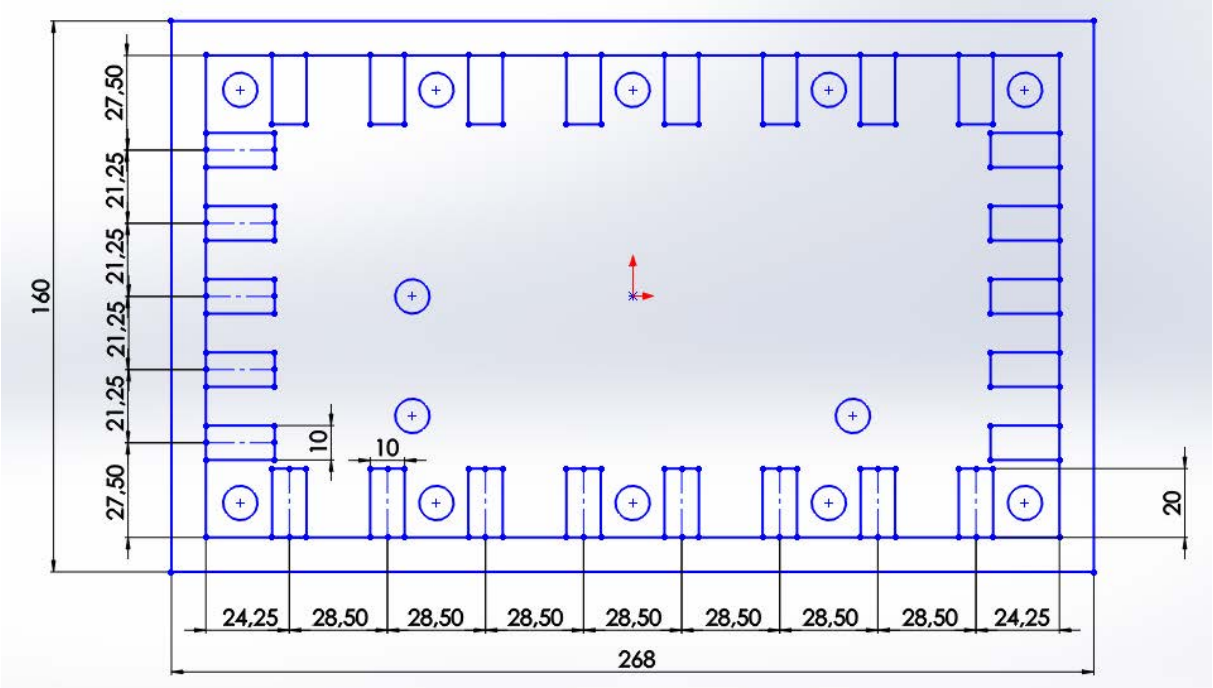

Figure 42: Placement of supports in shoe box face

Figure 43 depicts the remaining dimensions of the support and adhesive.

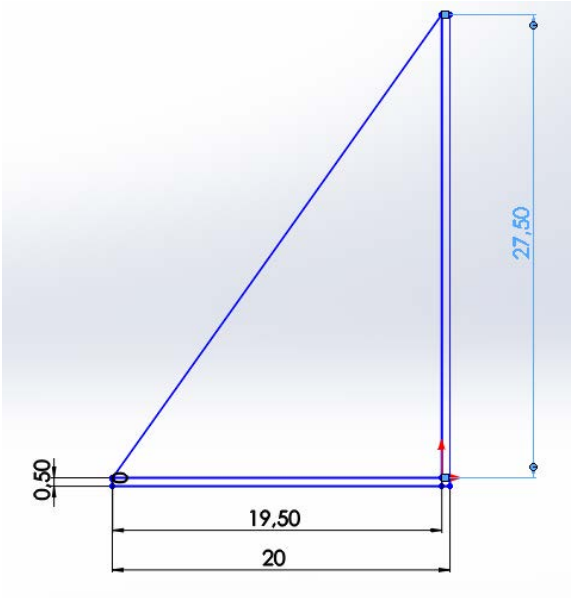

Figure 43: Dimensions of the support and epoxy adhesive

Inertia Plate

The inertia plate was named as so because it intended to decrease deflection through increase in moment of inertia. It comprises a centred face with the same dimensions of the other suggest composites, however the sides protrude. This was a big increase in volume, and with it, mass. Figure 44 depicts the general dimensions of the Inertia plate.

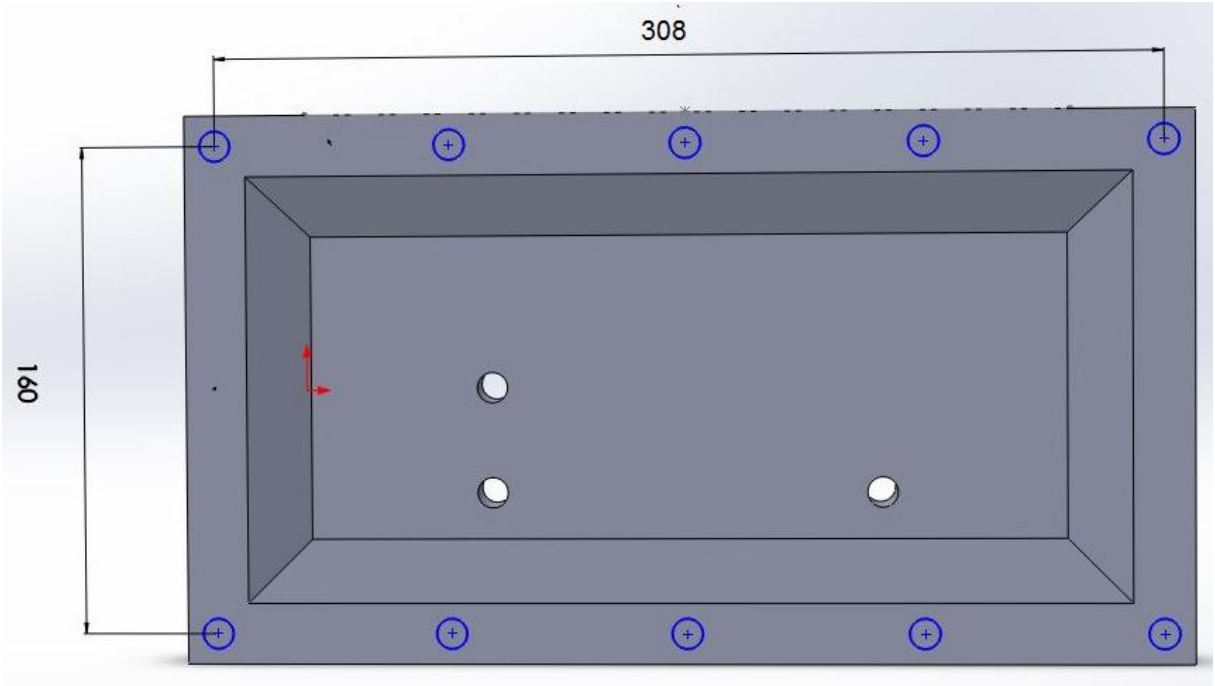

Figure 44: General dimensions of the Inertia plate

Figure 45 and Figure 46 depict a front and a rear view, respectively, of the Inertia plate.

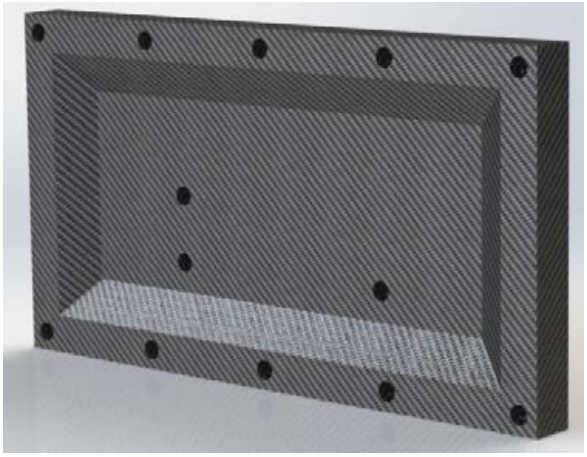

Figure 45: Front view of Inertia plate

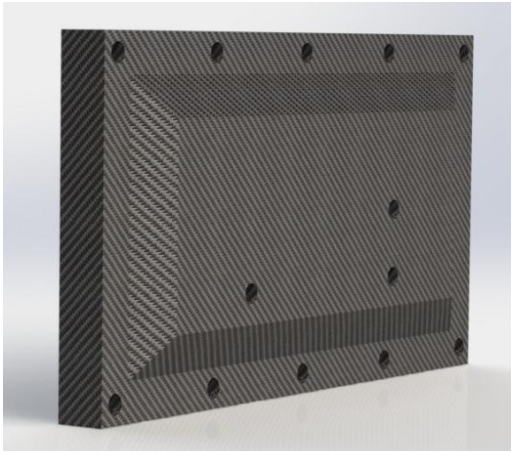

Figure 46: Back view of the Inertia plate

Reinforcement Plate

The reinforcement plate was conceived to be located between the suggested plates and the graphite block, so as to provide extra rigidity, as well as distribute stress more evenly across the graphite block's contact surface. Figure 47 depicts the reinforcement plate's general dimensions. Figure 48 depicts a Solid Works render of the reinforcement plate with the used thickness (10 mm).

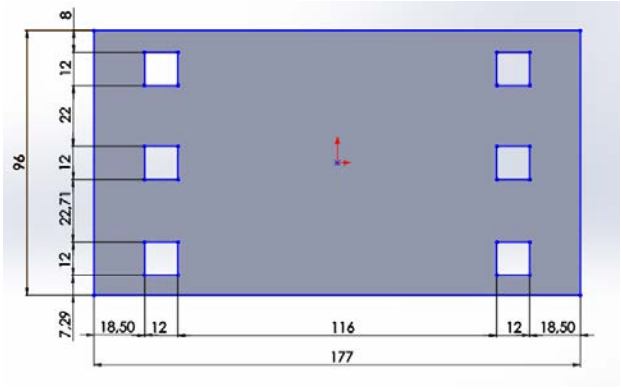

Figure 47: Reinforcement plate general dimensions

Figure 48: Reinforcement plate Solid Works render

3.2.3 Conceptual Plates

Table 13 comprises a summary of the applied concepts.

Table 13: Conceptual plates

Component		
Metal End Plate	Steel End Plate	
	Aluminium End Plate	
Shoe Box Assembly		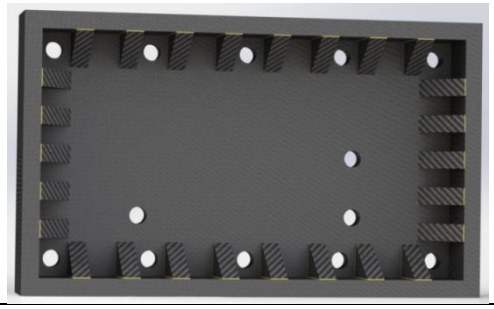
	Shoe Box Face and Cover	
	Adhesive for Shoebox	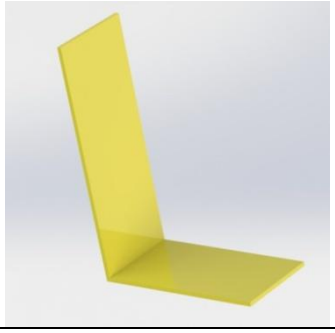

	Support	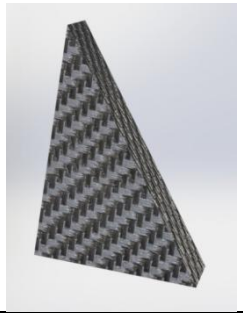
Double Pre-curvature		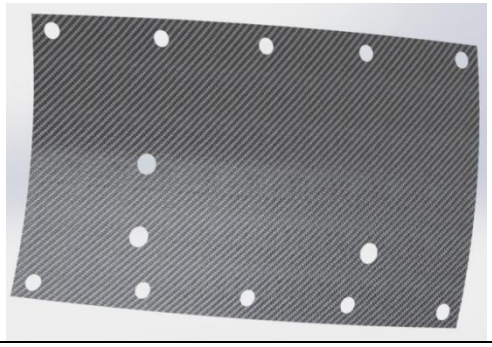
Inertia Plate		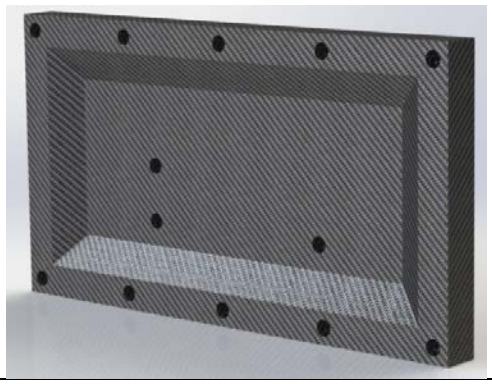
Normal		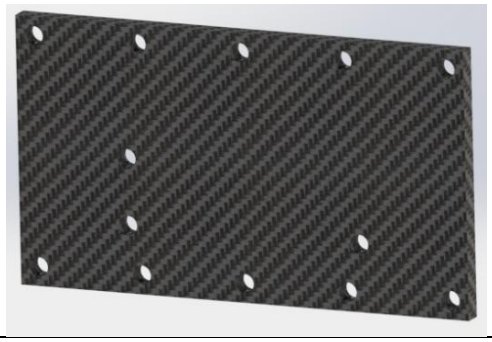
Reinforcement		

3.3 Clamping pressure assumption

The assumed clamping pressure was taken from the literature review. Work on the design of end plates for a 5 kW PEM FC, an assumption of 1,2 MPa for the clamping pressure was found suitable in that instance for the selected MEA. In fact, for safety testing purposes, a 1,5 MPa pressure was tested in the mentioned paper, [2]. In this case, having no information regarding the clamping pressure of the concerned system, and since the rated power is greater, a pressure of 1,5 MPa was assumed.

3.4 Selected ICE system

In order to perform a proper comparison, an ICE had to be chosen. There is, in the UAV industry, great concern over durability and reliability of engines. For that matter, engines with a higher rated power than that of aircraft requirements are often chosen, since working in a lower power than the rated one, results in increased reliability, though not working in the ideal state, leads to increased consumption.

For this case of 20 kW required for propulsion, the suggestion was to select an engine with about 30 kW of power. For that purpose, the UAV Engines Limited AR741 Wankel engine, a Single rotor Wankel-type spark ignition engine with 28,3 kW of power at 7800 RPM was chosen, as seen in Figure 49.

Figure 49: The UAV Engines Limited AR741 Wankel engine, [36]

Table 14 comprises the technical specifications of the selection engine.

Table 14: Technical specifications of the selected engine - UAV Engine Limited AR741 Wankel engine, [36]

Technical Specifications		
Chamber size	208 cm^3	
Maximum Power Output at 7800 RPM	37,95 HP	28,3 kW
Fuel Type	Mogas regular grade , leaded or unleaded, or AVGAS 100LL	
Vibration	Nominally zero radial vibration	

Consumption (maximum power)	9,84 kg/h
Consumption (cruise)	9,0 kg /h
Mass without generator (kg)	10,7
Generator	Provision for mounting GEC/Plessey 28 V, or 900 or 1500 W, weighing 3,5 kg

4. Numerical Modelling

This chapter comprises a description of each step of the employed methodology throughout the numerical modelling construction, as well as its results.

The use of numerical methods has become increasingly widespread and crucial in engineering problem solving. The Finite Element Method (FEM) is a numerical computational technique which enables the prediction of the behaviour of a given mechanical system. In order to ensure that this prediction is credible and reliable, the model must be an accurate replication of the real system.

The employed numerical modelling software in this project was Abaqus, a commercial software suited for finite element analysis (FEA) and computer aided engineering (CAE) originally released in 1978. Abaqus is currently used in applications ranging from aerospace, automotive, consumer packaged goods, energy and life sciences, allowing users to predict the behaviour of products and materials, thus improving performance, reliability, and safety, while reducing development costs, [37].

A good definition of an accurate model was given by David Moncayo in the presentation "Method Development and Validation for the Crash Simulation of Composite Structures in Automotive Applications" given at FEUP, and at which the author of this report was present, and goes as follows: *"Material model and discretization as simple as possible, but as complex as necessary"*.

The numerical modelling objectives given at that lecture, and that were kept in mind at all times throughout the use of this model were the following:

- Adequate material characterization;
- Adequate structural design of parts;
- Adequate joining methods;
- Adequate modelling techniques;
- Adequate interpretation of results.

A description of the numerical modelling construction is below and is followed by its results.

4.1 Numerical Modelling Construction

The construction of a numerical model implies relevant decisions, as for example, the simplifications regarding geometrical component simplification, element type selection for spatial discretization, finite element mesh generation, integration method, etc. Each one of the mentioned characteristics, along with a different combination of each, has a profound influence in the simulation final results. This leads to the fact that a very good and precise model is sometimes very hard to achieve, especially to the inexperienced user, such is the case of the author of this dissertation. For that reason, and since no experimental result for validation will be accomplished, the results of the performed models in this paper and respective conclusions are to be seen has a mere comparison between currently used and suggested concepts and materials, and should not be regarded as physically accurate results. A good numerical model is known to be one that represents the physical reality it intends to simulate to some degree of reliability.

In this section some decisions, simplifications and assumptions regarding the creation of the conceived numerical models are presented.

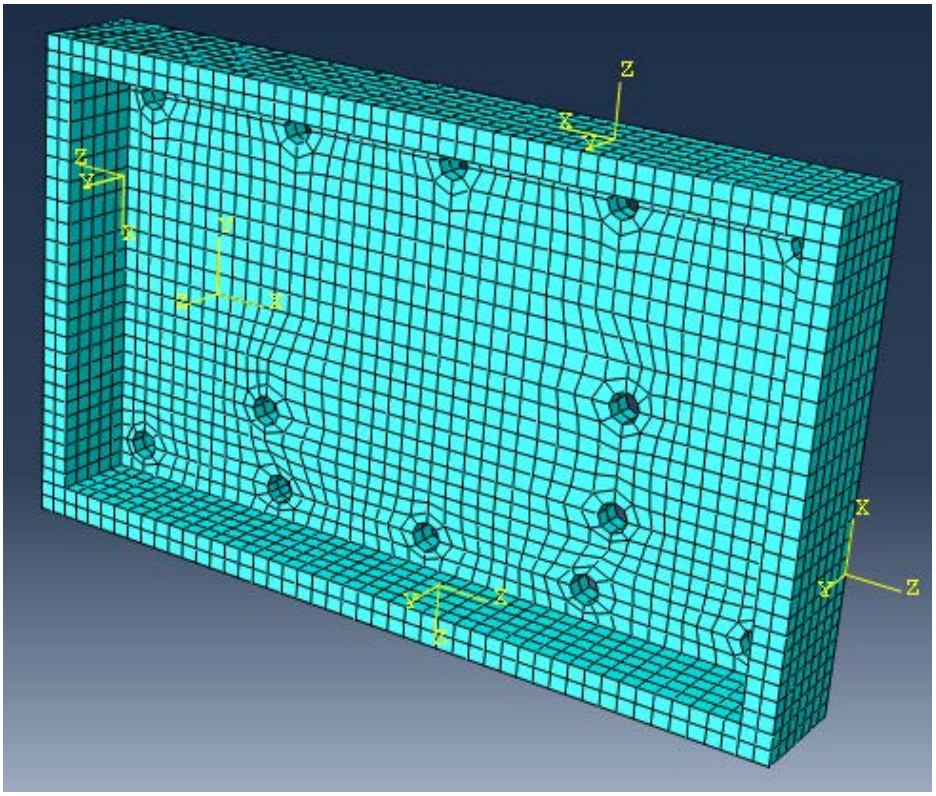

Figure 50: Finite Element Geometry and Mesh of an applied concept

The objective of the numerical modelling in this paper is to reach a conclusion, regarding the stress and deflection distribution on the edges of the graphite block that suffer the biggest deflection for every concept suggested. The mass of the composite concept that achieves the best results will then be analysed to see if sufficient mass reduction is achieved in order to enable FC viability in the considered UAV.

One model approach to determine stress and deflection was accomplished. The model poses as an alternative perspective of the system. The model comprises half of the fuel cell stack, i.e., a symmetry plane in the middle, however instead of applying the pressure in the

symmetry plane face, the equivalent force of the pressure is applied in the screw holes. The face of the graphite block located in the symmetry plane is then fixed in all translation and rotation movements. A representation can be seen in Figure 51. The yellow arrows represent the force being applied in the holes, while the orange and blue elements represent the fixed area of the graphite block.

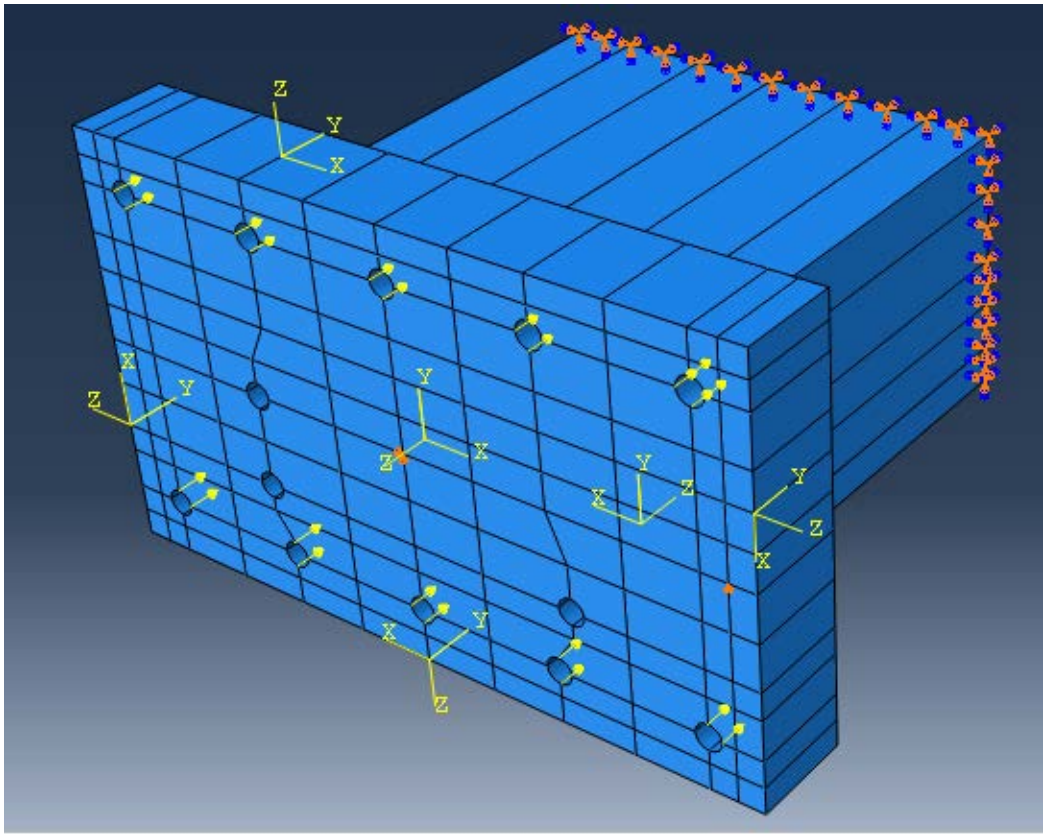

Figure 51: Representation of the model with applied loads (yellow arrows) and boundary conditions (blue and orange triangles)

4.1.1 Geometry Definition

Geometry Definition is an essential consideration within the numerical model construction. Two approaches are possible regarding this matter:

- sketching the part directly on Abaqus or;
- sketching it in any other computer aided design (CAD) software, such as SolidWorks, and then import it to Abaqus as a PARASOLID (.x_t) type file.

Both approaches have their own advantages and disadvantages. While the Abaqus user interface is somewhat poor (especially when compared to truly devoted computer assisted design software), leading to extreme difficulty in sketching if a geometrically complex part is intended, importing a file as Parasolid may result in some loss of geometrical data, for instance, some dimensions not being as exact as intended.

For that matter, Table 15 comprises the performed procedure that led to geometrical construction. The more complex geometries parts, such as the Metal End Plate, the Shoe Box, the Inertia plate, and the Double Pre-curvature Plate were sketched in Solid Works and imported to Abaqus. In fact, some geometrical exactitude errors were displayed upon the import of the Double Pre-curvature Plate. All of the remaining components, being of less complex geometry, were designed in Abaqus.

Table 15: Component Geometrical sketch procedure

Component			Procedure
Metal End Plate	Steel End Plate Aluminium End Plate	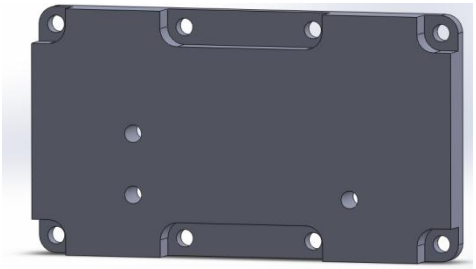	Sketched as solid in SolidWorks; imported as Solid to Abaqus
Shoe Box Assembly		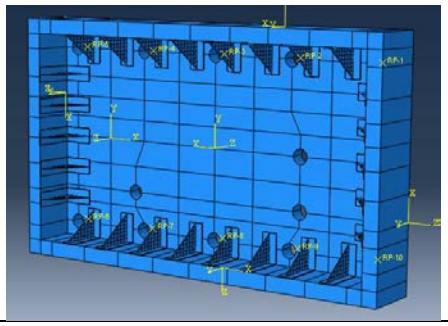	Result of Interactions
	Shoe Box Face and Cover	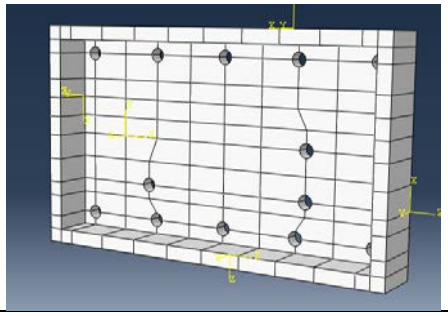	Sketched as solid in Solid Works and imported to Abaqus
	Adhesive For Shoebox	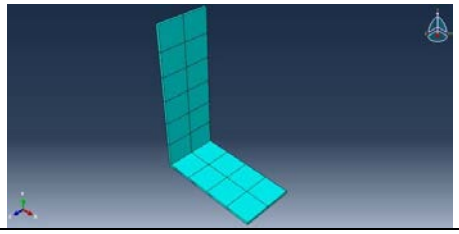	Sketch as solid in Abaqus
	Support	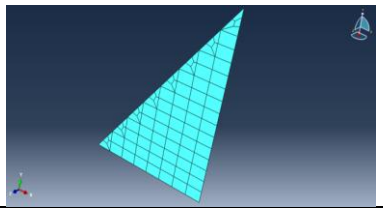	Sketched as shell in Abaqus
Double Pre-curvature		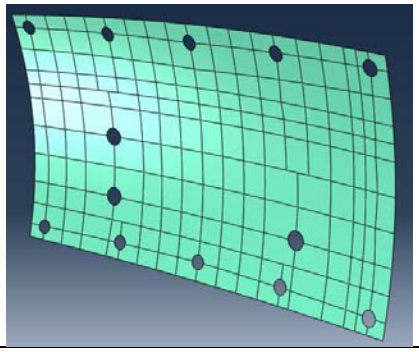	Sketched as Surface in SolidWorks and imported as shell to Abaqus

Inertia Plate	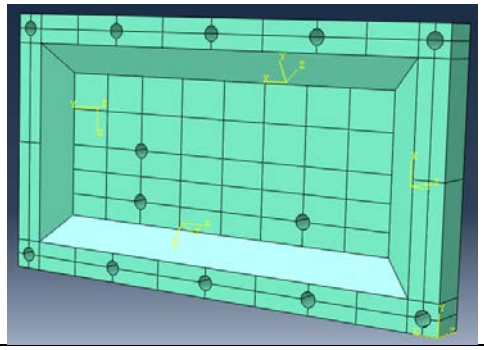	Sketched as solid in SolidWorks and imported as solid to Abaqus
Normal	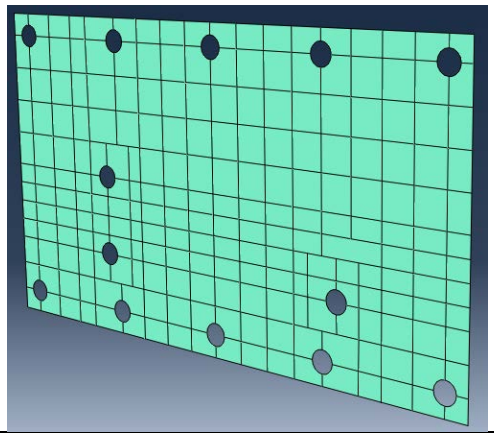	Sketched as shell in Abaqus
Reinforcement	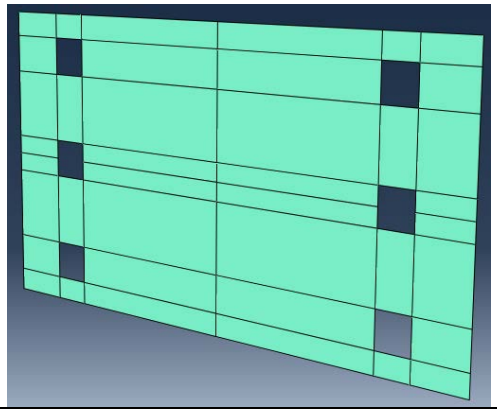	Sketched as shell in Abaqus

4.1.2 Material Definition

This section defines the properties of the materials considered in the numerical modelling. The following materials were used: Aluminium, Steel, Carbon Fibre Reinforced Polymer (CFRP), and an Epoxy Resin. Table 16 relates the used material for each Part.

Table 16: Used materials for each component and part

Part/Assembly			Material
Metal End Plate	Steel End Plate	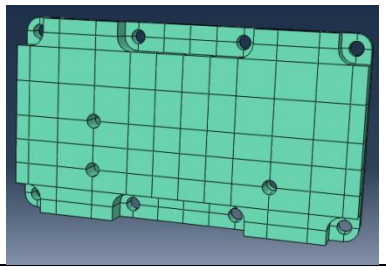	Steel
	Aluminium End Plate		Aluminium
Shoe Box Assembly		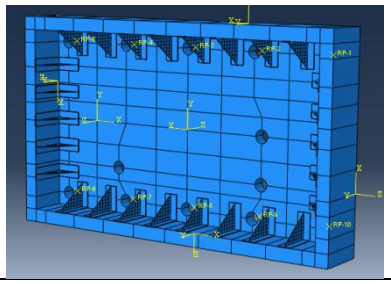	
	Shoe Box Face and Cover	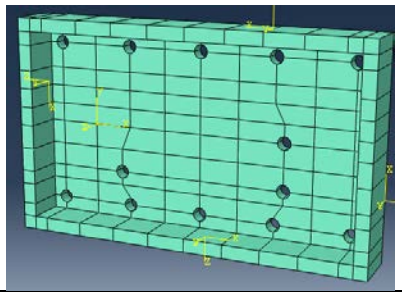	CFRP
	Shoebox Adhesive	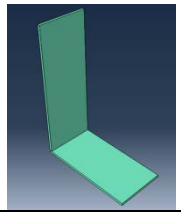	Epoxy
	Support	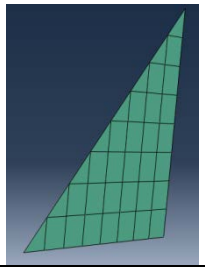	CFRP
Double Pre-curvature		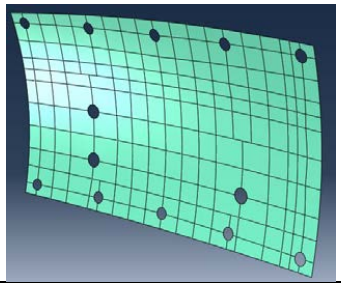	CFRP

Inertia Plate	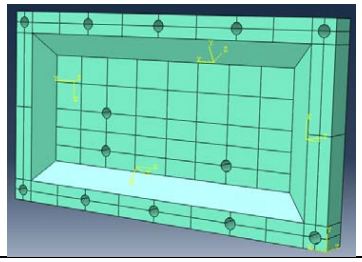	CFRP
Normal	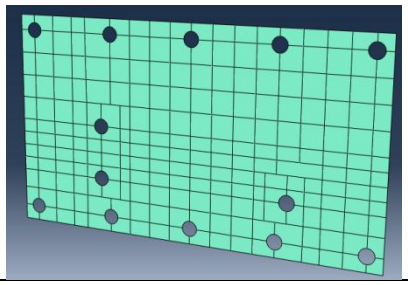	CFRP
Reinforcement	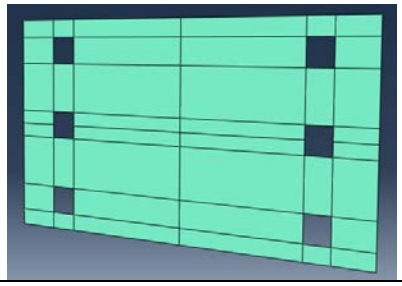	CFRP
Graphite Block	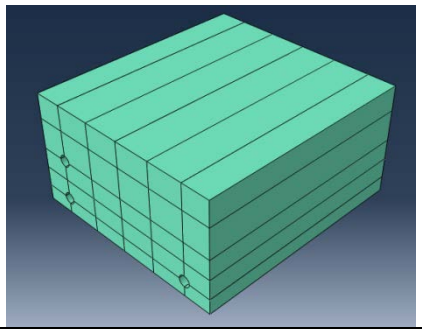	Graphite Block Assumption Material

For this model, only elastic analysis were performed, since no plastic behaviour for the mentioned materials is foreseen with an applied pressure of 1,5 MPa. In fact, CFRP and the Graphite assumption are brittle; therefore do not possess plastic behaviour even if non-linearity can be seen in delamination/damage propagation of composites. For that matter, only the elastic mechanical properties of each material were considered. As shown in Section 2, unidirectional composite materials, unlike steel and aluminium e.g., are not isotropic and it is necessary to distinguish the mechanical property description of each. Regarding material selection and assumption, for the considered steel and aluminium materials, no specific catalogue material was selected.

Since there was no clear idea on what to consider for the graphite block, an assumption was made regarding its mechanical properties and mass density, based in a comparison with common graphite The assumption was performed considering that graphite has the following properties.

- $E_{graphite} = 11\ GPa$
- $\upsilon_{graphite} = 0{,}31$

- , $\rho_{graphite} = 2200\ kg/m^3$

The graphite block, i.e., the combination of all the components within the clamped cells, was assumed to have $\rho_{graphite\ block} = 1000\ kg/m^3$. The assumption made regarding its mechanical properties was that, since mass density ratio ($\rho_{graphite\ block}/\rho_{graphte}$) is roughly 1 to 2, then its mechanical properties would also be divided two fold (see Table 17).

Table 17 and Table 19 comprise the mechanical properties for the modelled isotropic and orthotropic materials, respectively.

Table 17: Mechanical Properties of the considered isotropic materials, and respective mass density

Isotropic Material	Young Modulus, E (GPa)	Poisson Coefficient, υ	Mass density, ρ (kg/m^3)
Steel	210,00	0,3	7800
Aluminium	70,00	0,3	2400
Epoxy	3,66	0,36	1200
Graphite Block Assumption Material	5,50	0,3	1000

The chosen CFRP was the Toray M40J (data sheet available in Annexe A).

Table 18 displays the properties of the fibre employed in the composite M40J.

Table 18: Toray M40J Fibre Properties

Fibre Properties	
Fibre Tensile Modulus	377 GPa
Fibre Density	1770 kg/m^3
Composite Properties	
Composite Tensile Modulus	230 GPa
Tensile Strain	1,1%
Fibre volume	60%
Matrix	Toray 250ºF Epoxy Resin

Considering that the M40J CFRP has 60% fibre volume, i.e. $V_f = 0{,}60$, then recalling Equation 2.41and Equation 2.48, the values for E_1 and E_2 should be c. 227 GPa and 11 GPa, respectively, suggesting that the 230 GPa of Composite Tensile Modulus in Table 18 are the result of an approximation.

Since no data was available regarding shear modulus: G_{12}, G_{13}, G_{23}; and Poisson ratios: υ_{12}, υ_{13} and υ_{23}, these parameters had to be assumed.

Recalling Table 6:

- $E_2 = E_3$
- $G_{12} = G_{31}$
- $G_{23} = \frac{E_2}{2(1+\upsilon_{23})}$

- $\upsilon_{12} = \upsilon_{13}$

The following parameters were assumed to have the following values:

- $G_{12} = G_{31} = 5\ GPa$
- $\upsilon_{12} = \upsilon_{13} = 0{,}25$
- $\upsilon_{23} = 0{,}25\ GPa$

Thus, resulting in $G_{23} = 4{,}4\ GPa$.

Composite mass density can also be obtained through the rule of mixtures, as in Equation 4.1.

$$\rho_{composite} = \rho_{fibre} \times V_{fibre} + \rho_{matrix} \times V_{matrix} \qquad \text{Equation 4.1}$$

All parameters, except for the mass density of the matrix, ρ_{matrix}, are known. Since no data is provided by the manufacturer on this matter, ρ_{matrix} is assumed to be $1200\ kg/m^3$ after consultation of similar matrixes in the software ESAComp.

As previously mentioned, Table 19 comprises the mechanical properties, along with the mass density of the employed CFRP.

Table 19: Mechanical Properties of the considered orthotropic material, and mass density

Non Isotropic Material	E_1 (GPa)	E_2 (GPa)	E_3 (GPa)	υ_{12}	υ_{13}	υ_{23}	G_{12} (GPa)	G_{13} (GPa)	G_{23} (GPa)	ρ (kg/m^3)
CFRP	227	11	11	0,25	0,25	0,25	5	5	4,4	1542

Table 20 describes the stacking sequence, ply thickness, and resulting plate thickness for the considered carbon/epoxy composite material used.

Table 20: Carbon/epoxy stacking sequence and ply thickness for the considered composite parts

Carbon/epoxy composite		
Stacking Sequence	Ply thickness (mm)	Resulting plate thickness (mm)
$[0/90]_{25}$	0,200	10

For the composite section assignment, the Abaqus Composite Layup Manager was used. This manager enables the definition of several parameters for each ply of the laminate, such as the intended region, material, ply thickness, coordinate system, fibre orientation (Rotation Angle), and number of integration points, as seen in Figure 52. This Manager can be applied in either Shell or Solid Elements. As for Shell Elements, the Manager allows the offset to be performed in the location best preferred by the user: Top, Middle, Bottom or User defined surface.

		Ply Name	Region	Material	Thickness	CSYS	Rotation Angle	Integration Points
1	✔	Ply-1	(Picked)	CFRP	0.2	<Layup>	0	3
2	✔	Ply-2	(Picked)	CFRP	0.2	<Layup>	90	3
3	✔	Ply-1-Copy1	(Picked)	CFRP	0.2	<Layup>	0	3
4	✔	Ply-2-Copy1	(Picked)	CFRP	0.2	<Layup>	90	3
5	✔	Ply-1-Copy2	(Picked)	CFRP	0.2	<Layup>	0	3

Figure 52: Abaqus Composite Layup Manager

4.1.3 Contact definition

Contact definition is an important aspect of a numerical model where two or more components are, or come into contact throughout the simulation. The contact regions of the model can be defined as the regions where contact between parts takes place.

There were two types of contact definition considered for both considered models:

- Through the Interaction Manager, a Surface-to-Surface contact was selected, having considered "Normal Behaviour", Finite Sliding and allowed separation after contact in the Contact Property options. This type of contact definition is most suitable for contact of materials that have friction between each other, having always been used in the contact definition between the Graphite Block and the Reinforcement Plate or End Plate that followed.
- Through the Constraint Manager, a Tie type constraint was defined. This type of contact definition was used always between the Composite End Plate concepts and reinforcements, as well as between the Shoe Box face and adhesive and support. A Position Tolerance of 0,1 mm was considered.

Having defined the interaction properties, Abaqus then asks to proceed to select the surfaces that come into contact defining each as *slave* and *master* surfaces. The contact interactions are defined in Table 21.

Table 21: Contact description and representation

Contact Description	Representation
Interaction between Graphite Block and End Plates	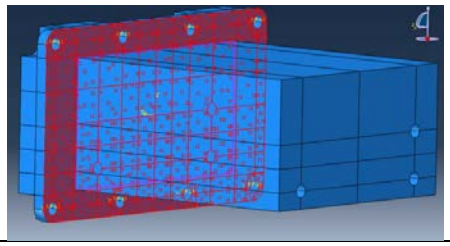
Tie between Plates and Reinforcement	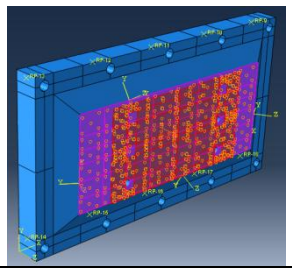
Tie between Shoe Box side face and Adhesive	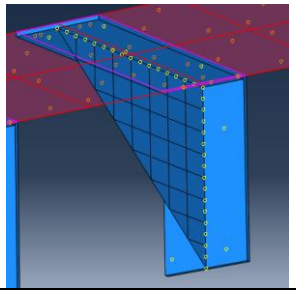

Tie between Shoe Box centre face and Adhesive	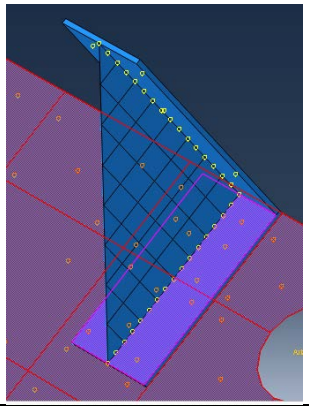
Tie between Adhesive and support	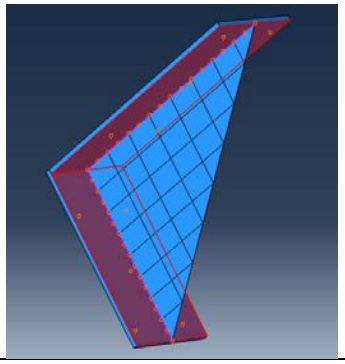

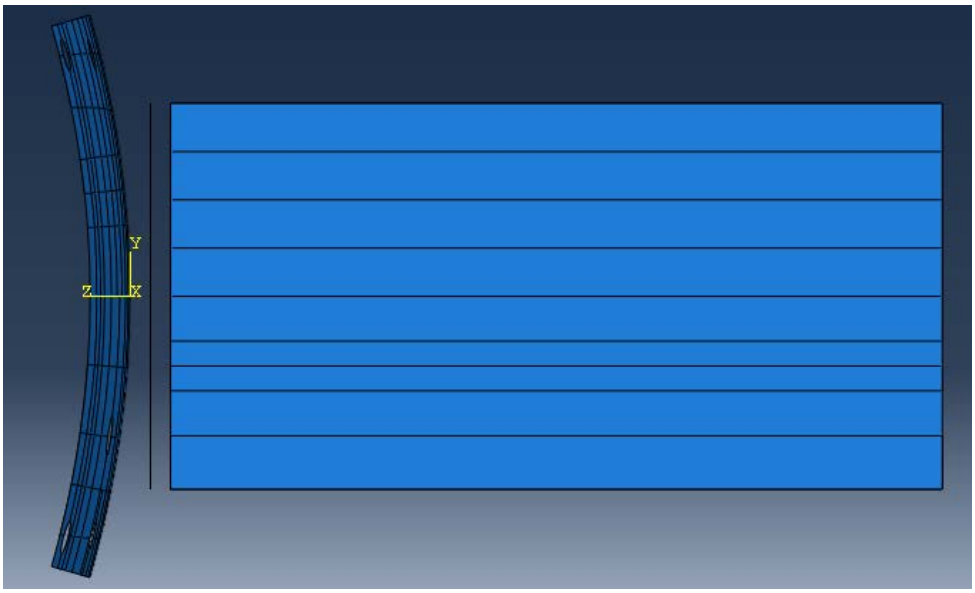

Figure 53: Example of tested assembly; Plate on the left, reinforcement in the middle, and graphite block to the right

4.1.4 Load and External connections definition

This part of the section describes the approach taken to loads and fixation.

Independently of the model, null displacements in the directions 1 and 2 (x and y) were performed in a centre point of each part, as well as null displacement in direction 2 in a side point of each part, in order to prevent unintended torsion. This situation is exemplified in Figure 54. The orange triangles represent the central and side fixations.

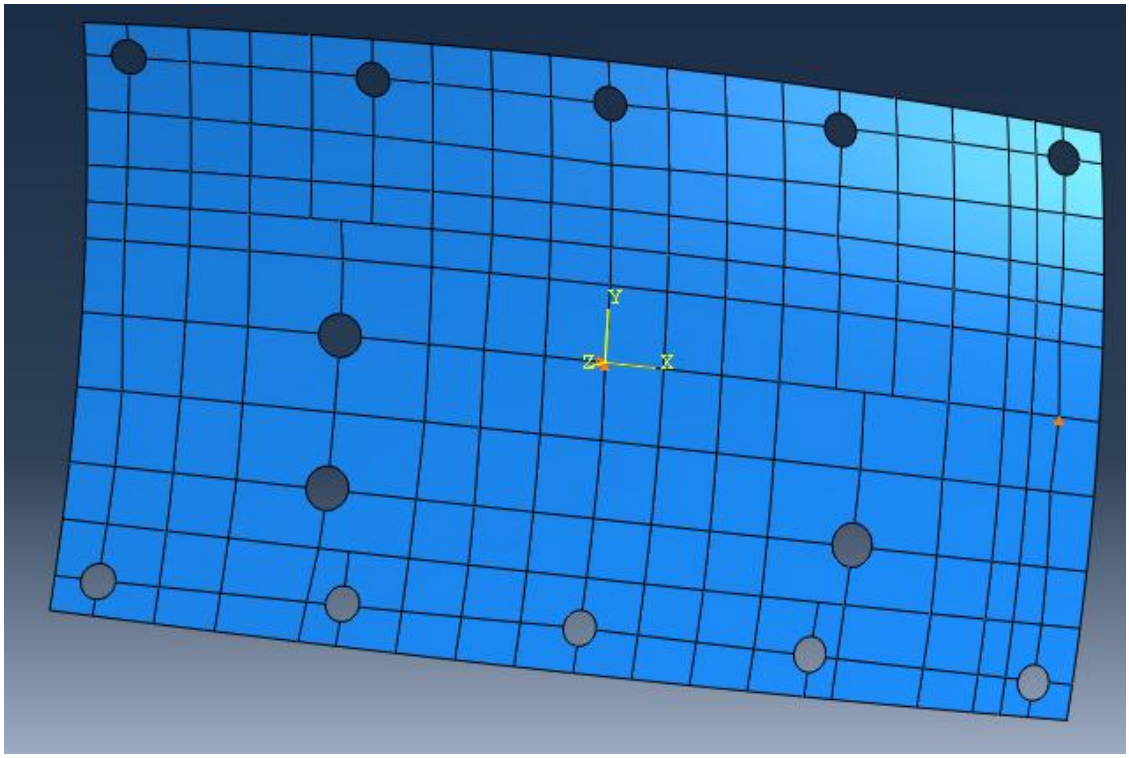

Figure 54: Double pre-curvature plate; displacements disabled (orange triangles) in centre (U1,U2; x and y) and side (U2; y)

As mentioned previously (see Figure 51), the clamping force is applied in the holes, and the fixation is performed in the graphite block symmetry face, as seen from an above view in Figure 55. Also seen in Figure 55, the $z-$ axis is normal to the CFRP block. Stress and displacement results will be obtained in the mentioned axis.

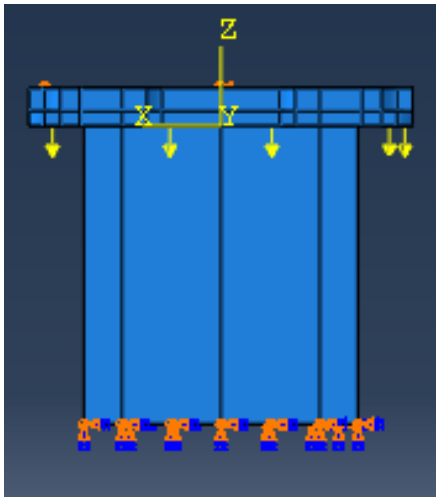

Figure 55: Loads (yellow arrows) and fixation (orange and blue triangles) seen from above

The calculus of the equivalent force, $F_{equivalent}$, calculated knowing the assumed pressure, P, and the area, A, onto which it would be applied, i.e., the area of the contact surface of the graphite block with the end plate.

$$F_{equivalent} = P \times A$$

Remembering Section 3.3, the assumed pressure, taken from [2], is as follows:

$$P = 1{,}5 \times 10^6\ Pa$$

A and $F_{equivalent}$ are then:

$$A = 0{,}177 \times 0{,}096\ m^2$$

$$F_{equivalent} = 25\ 488\ N$$

The obtained force must then be divided by the number of holes present in the plate. This differs from the metallic end plate to the composite suggested ones, since the metallic end plate has 8 holes, while the composite has 10. Since each hole contains 4 points, the force must then be divided by 4.

$$F_{eq\_hole\_metal} = \frac{25\ 488\ N}{8}$$

$$F_{eq\_hole\_composite} = \frac{25\ 488\ N}{10}$$

Table 22: Equivalent force per hole for the metal and composite end plates

	Number of holes	$F_{equivalent}\_hole$ (N)	Equivalent force per point (N)
Metal end plate	8	3186	796,5
Composite end plate	10	2548,8	637,2

It should be noted that, in reality, the reaction force of each screw is not the same for all. In fact, the reaction force should be bigger on the centre holes than in the side holes. A different, and perhaps more accurate, approach would be to consider the pressure to be applied in the face of the graphite block located on the symmetry plane. The fixation could be performed by a tool present in Abaqus, which consists of rigidly fixing reference points in the holes, such as if they were springs, being that the rigidity of the spring would be the one of the screw/fixating element.

4.1.5 Discretization

Perhaps one of the most important and influential aspects in the construction of a numerical model is finite element discretization. Quality of results is strongly influenced by the type of elements employed, as well as finite element mesh quality. Solid (C3D8) and shell (S4) elements were used, always with reduced integration, hence the "R". Table 23 describes the type of element, quantity of nodes, and quantity of elements for the meshed parts.

Table 23: Type of Element, Quantity of Nodes and Elements for each part

Component		Type of Element		Quantity of Nodes	Quantity of Elements
Metal End Plate	Steel End Plate	Solid	C3D8R	37671	31587
	Aluminium End Plate				
Shoe Box Assembly					
Shoe Box Face and Cover		Solid	C3D8R	6654	4200
Adhesive For Shoe Box		Solid	C3D8R	576	245
Support		Shell	S4R	1793	1696
Double Pre-curvature		Shell	S4R	852	753
Inertia Plate		Solid	C3D8R	17772	14100
Normal		Shell	S4R	4140	3936
Reinforcement plate		Shell	S4R	521	456
Graphite Block		Solid	C3D8R	102846	95160

The accuracy of the results from a FEA is directly related with the number of elements used. However, an increase in element number leads to an increased computational cost, and for that matter, any mesh refinement has to be properly considered by the user. In this sense, it would be wise to increase element number in the parts/areas of the model where the gathering of results will take place, thus leading to greater productivity.

Partition

The part partition process is a division of geometrically complex parts, containing holes, and/or parts resultant from merge of two or more parts. It is an essential procedure in order to generate a good quality structured mesh and which can be considerably time consuming. Abaqus offers a "Auto-partition" tool, however it rarely performs the partition in the most efficient way. For that reason, all of the partitions performed in the tested parts were manual partitions, that were often very complex and demanding tasks. Such was the example of the pre-curvature plate shown in Figure 56, for not only were the holes a demanding problem to solve, but also the fact that the surface had a double curvature, leading to a very time demanding task.

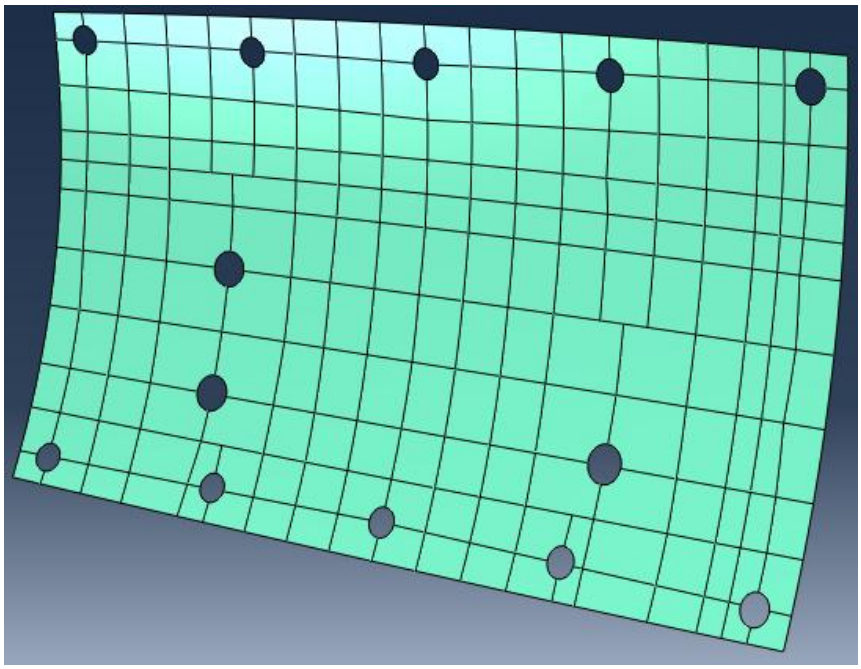

Figure 56: Pre-curvature plate partition

4.1.6 Results

The higher values of stress and displacement were generally found in the upper and lower edges of the graphite block. For that matter, using the "path" tool on Abaqus, the collection of nodes on those edges was established, so that the displacement could be then gathered for each point so as to be analysed and to create a plot. The top and bottom edge paths can be seen in Figure 57 and Figure 58, respectively.

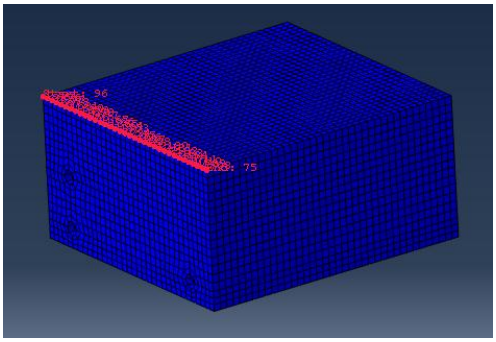

Figure 57: Top edge path on the graphite block

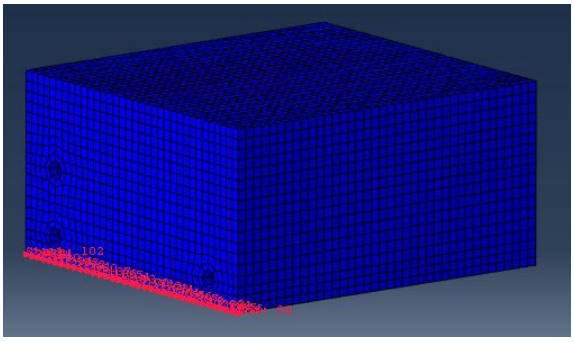

Figure 58: Bottom edge path on the graphite block

There was however the exception of the pre-curvature plate. Its maximum displacement and stress were not found in the upper nor lower edges, as seen in Figure 59 and Figure 60, which show the displacement and stress distribution on the graphite block's face. For that matter its path was covered elsewhere, as shown in Figure 61. The higher displacement values are negative. This is obviously related to approach taken to model construction, i.e., the application of force in the holes, naturally results in negative displacement, considering the employed coordinate system. For that matter, the areas in blue in Figure 59 and Figure 61 are the places with the biggest displacement, contrary to Figure 60, where red stands for the location with the highest stress.

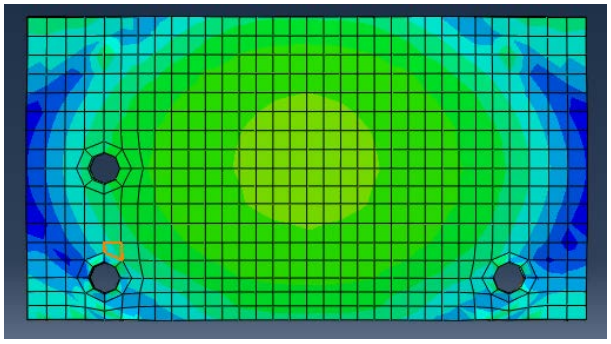

Figure 59: Displacement distribution in graphite block with pre-curvature end plate

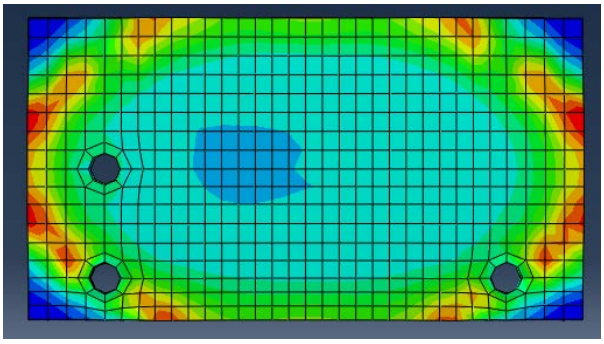

Figure 60: Von Mises Stress distribution in graphite block with pre-curvature end plate

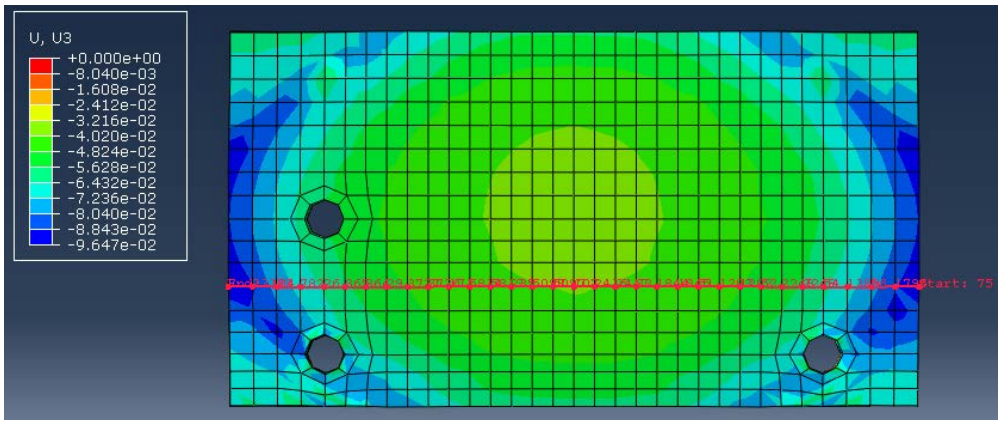

Figure 61: Placement of path for the graphite block, considering the pre-curvature plate

The maximum displacement and stress results of the plate model are shown in Table 24. Along with those parameters, the mass of each concept is also present. The pre-curvature plate was not considered without reinforcement. This is due to the fact that the reinforcement in this case is necessary in order to provide a good distribution of stress. Otherwise, stress would concentrate in the centre of the face.

Table 24: Concept results for the model

	Max Displacement in Graphite Block, $U_{3\ max}\ (mm)$	Min Displacement in Graphite Block, $U_{3\ min}\ (mm)$	Max von Mises Stress in Graphite Block surface, $S_{von\ Mises\ max}\ (MPa)$	Mass (kg)
Steel End Plate	$-7{,}564 \times 10^{-2}$	$-4{,}499 \times 10^{-2}$	4,060	5,794
Aluminium End Plate	$-9{,}969 \times 10^{-2}$	$-4{,}417 \times 10^{-2}$	7,202	2,005
Normal Plate				
No reinforcement (noRF)	$-22{,}220 \times 10^{-2}$	$-6{,}500 \times 10^{-2}$	28,150	0,520
10 mm reinforcement	$-15{,}190 \times 10^{-2}$	$-5{,}584 \times 10^{-2}$	14,750	$0{,}520 + 0{,}249 = 0{,}769$
Double Pre-curvature w	$-9{,}647 \times 10^{-2}$	$-3{,}996 \times 10^{-2}$	5,884	$0{,}527 + 0{,}249 = 0{,}776$
Shoe Box				
No reinforcement (noRF)	$-16{,}200 \times 10^{-2}$	$-7{,}474 \times 10^{-2}$	16,37	0,972
10 mm reinforcement	$-11{,}384 \times 10^{-2}$	$-6{,}137 \times 10^{-2}$	7,904	1,220
Inertia Plate				
No Reinforcement (noRF)	$-11{,}120 \times 10^{-2}$	$-5{,}531 \times 10^{-2}$	7,000	2,230
10 mm reinforcement Top edge	$-9{,}191 \times 10^{-2}$	$-5{,}234 \times 10^{-2}$	5,653	2,482

Figure 62 shows the displacement of the plates above along the bottom horizontal edge with some exceptions. The Shoe Box and Normal without reinforcement plates were not considered in Figure 62 for their displacement results are clearly worse than the remaining concepts, and their presence would result in a least detailed observation of the curves that interest the most.

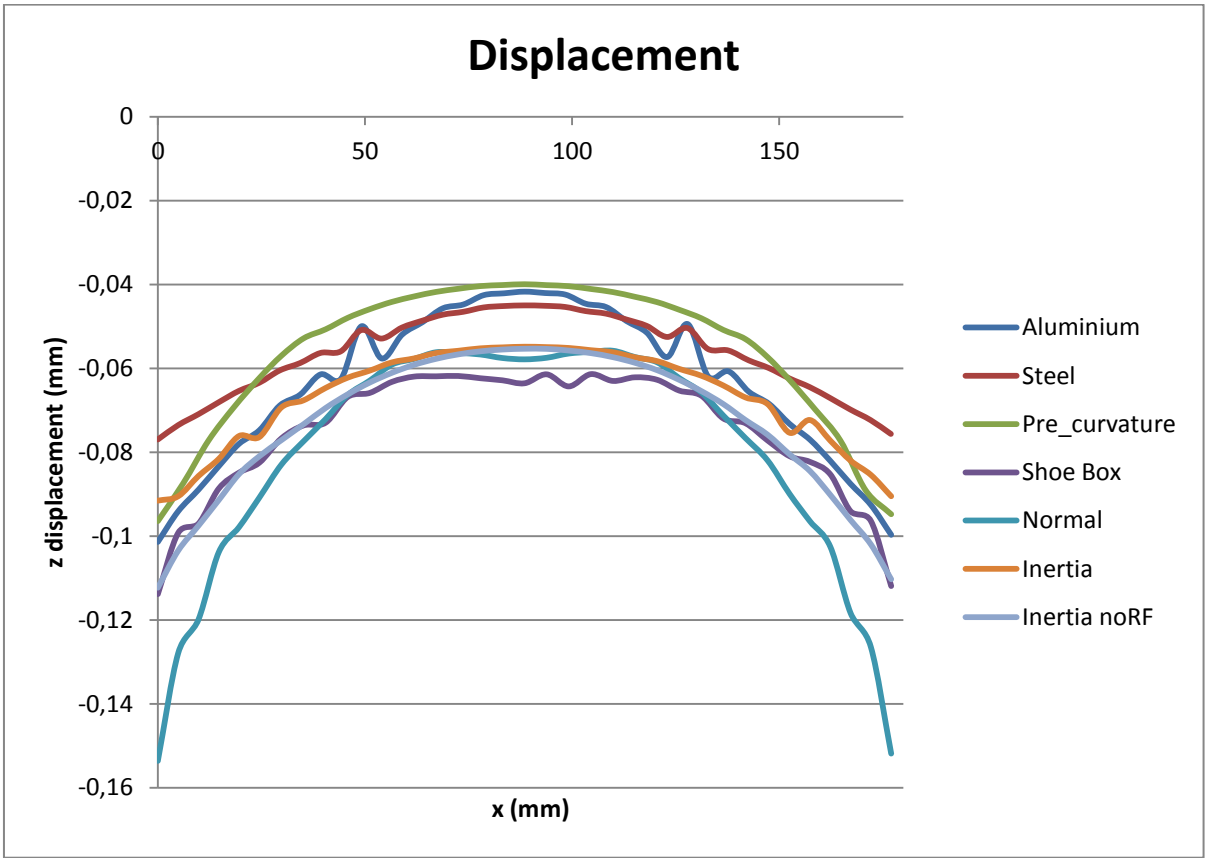

Figure 62: Displacement of each concept of the plate model with respect to the x-direction

The deflection, ∂, of each concept was then calculated and plotted to determine which deformed the most. The calculation is performed subtracting the displacement in the $z-axis$ of each point from the displacement of the point that displaced the most for each plate, as in Equation 4.2.

$$\partial(x) = U_3(x) - U_{3\,max} \qquad \text{Equation 4.2}$$

Table 25 comprises the maximum deflection in the graphite block for each of the concepts, as well as the respective maximum stress and mass.

Table 25: Deflection results for the model

	Max Deflection in Graphite Block, $\partial_{max}\ (mm)$	Max von Mises Stress in Graphite Block surface, $S_{von\ Mises\ max}\ (MPa)$	Mass (kg)
Steel End Plate	$-3{,}064 \times 10^{-2}$	4,060	5,794
Aluminium End Plate	$-5{,}799 \times 10^{-2}$	7,202	2,005
Normal Plate			
No reinforcement	$-21{,}857 \times 10^{-2}$	28,150	0,520
10 mm reinforcement	$-9{,}606 \times 10^{-2}$	14,750	$0{,}520 + 0{,}249 = 0{,}769$
Double Pre-curvature	$-5{,}487 \times 10^{-2}$	5,884	$0{,}527 + 0{,}249 = 0{,}776$
Shoe Box			
No reinforcement	$-8{,}400 \times 10^{-2}$	16,37	0,972
10 mm reinforcement w	$-5{,}055 \times 10^{-2}$	7,904	1,220
Inertia Plate			
No Reinforcement	$-5{,}502 \times 10^{-2}$	7,000	2,230
10 mm reinforcement Top edge	$-3{,}567 \times 10^{-2}$	5,653	2,482

The plot of the deflection of each plate is shown in Figure 63, again with the exception of the Shoe box and Normal without reinforcement plates.

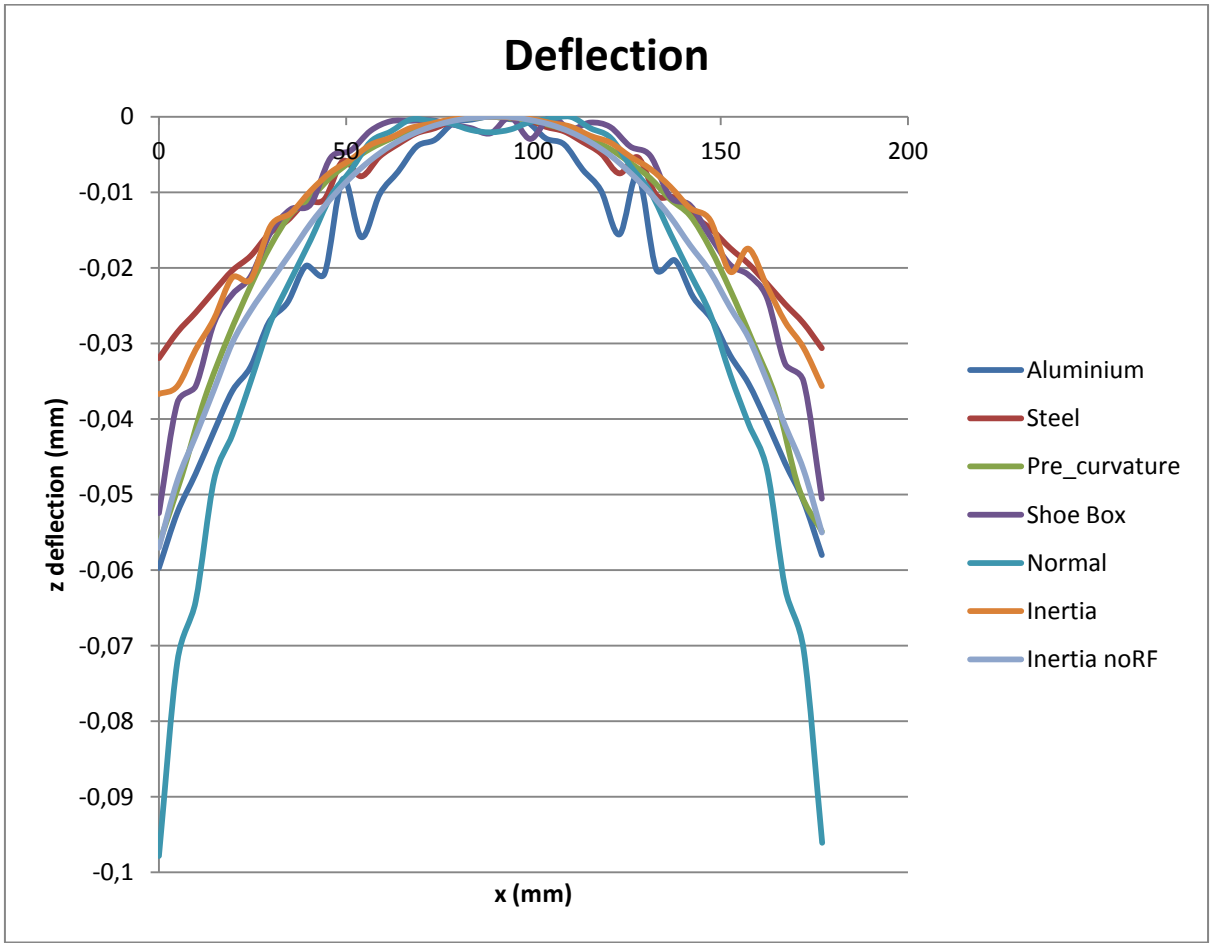

Figure 63: Deflection of each concept of the plate model with respect to the x-direction

In what regards stress and displacement distribution in the whole surface, Table 26 provides with the figures for each of the tested concepts.

Table 26: Stress and displacement distribution in the graphite block's face for every tested concept

End plate concept	Von Mises Stress distribution	Displacement distribution
Steel End Plate	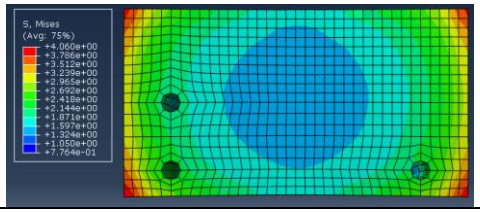	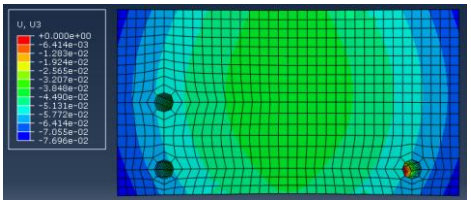
Aluminium End Plate	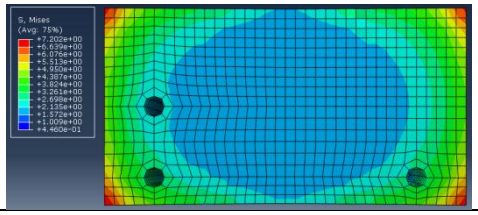	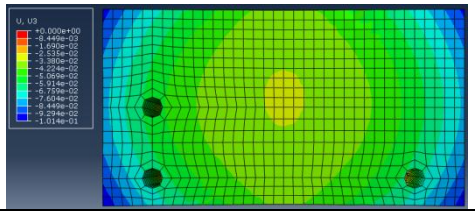
Normal Plate		
No reinforcement	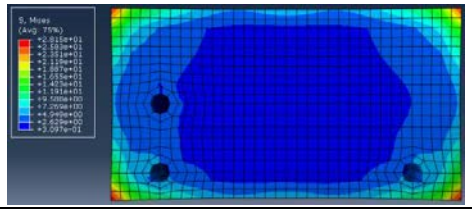	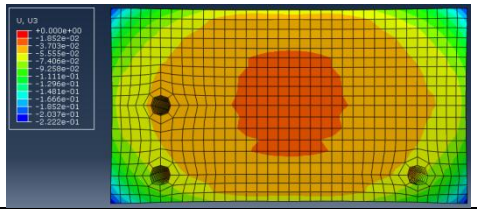
10 mm reinforcement	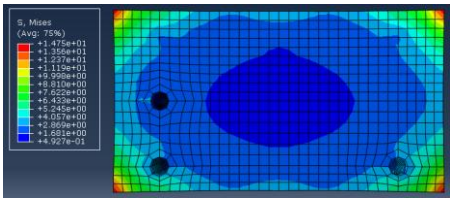	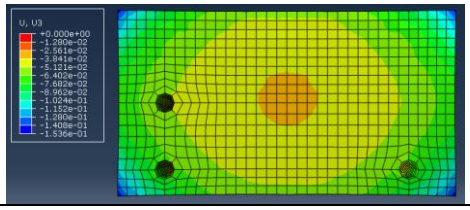
Double Pre-curvature	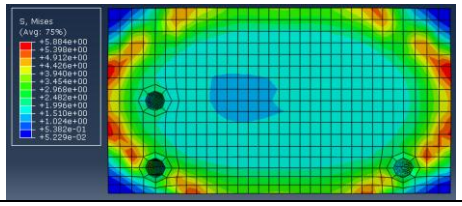	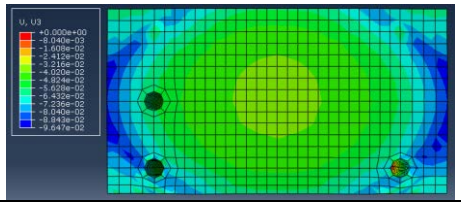
Shoe Box		
No reinforcement	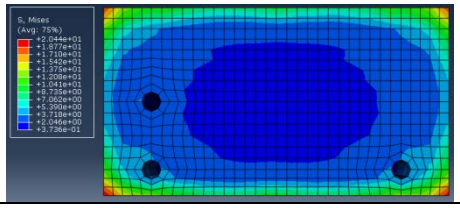	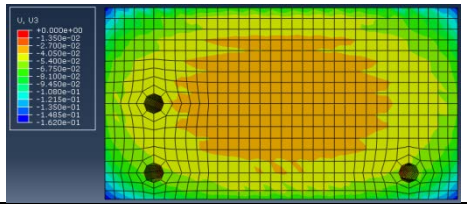
10 mm reinforcement	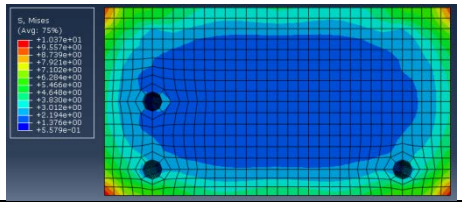	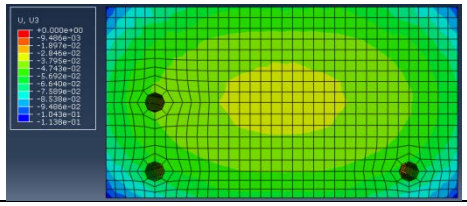
Inertia Plate		

	No Reinforcement	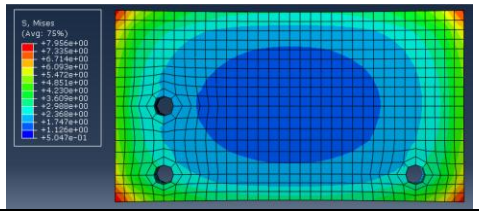	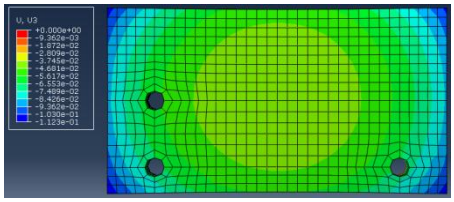
	10 mm reinforcement Top edge	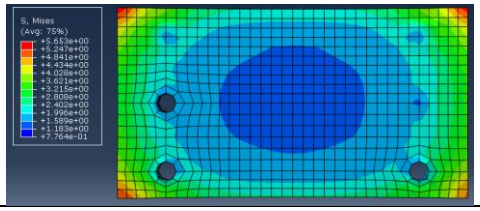	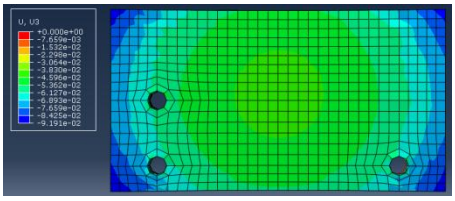

Note: the colours in the displacement column are inverted due to negative displacement, i.e., blue stands as maximum displacement, while red minimum.

5. Results Discussion

5.1 End Plate Numerical Model results

As was expected, the steel EP has the smallest deflection, however three of the composite plates (Inertia Plate, Shoe box and Pre-curvature) concepts succeed in achieving smaller deflection than the Aluminium end plate. Of those three, the one that succeeds in having the smaller mass is the pre-curvature, as seen previously in Table 25.

The best composite performer in this model is considered to be the pre-curvature plate with reinforcement. Although it did not achieve the lowest values of stress and deflection, the difference between these results and the best performer, the Inertia Plate, is not very significant, and more importantly, its mass is significantly lower than the Inertia Plate: 0,776 kg to 2,482, little more than 3 times lower. Furthermore, its stress-deflection results are clearly better than the aluminium plate.
Moreover, looking at the stress-displacement figures provided by Abaqus in Table 26, one can see that the pre-curvature plate has a configuration that is completely unlike all the others. It has apparently managed to distribute stress differently, especially out from the corners which now have a similar stress to the centre, unlike the other concepts, where the critical stress is in the corners. A significant stress concentration (reddish areas) can be seen in what seems to be an ellipse, in which the biggest stress value is of c. 5,9 MPa, against the 5,7 MPa of the Inertia Plate and 4,1 MPa of the steel end plate. A study on cell performance would have to be made in order to ascertain which of the stress distributions result in the best performance, however, having a similar value of stress as its competitors only placed in a more centred region rather than in the block's corners, the pre-curvature plate has apparently the most uniform stress-displacement distribution of all the concepts studied.

Within the concepts without a reinforcement plate, only the Inertia was selected, the others had far worse results than the average in such a way that it did not make sense to consider them, for it would harm the comparative analysis.

Another interesting observation is that the introduction of the reinforcement plate in the assembly successfully managed to mitigate graphite block deflection caused by the bottom holes. As seen in Figure 63, the aluminium plate curve has two irregular parts of the curvature, which seem to be created by the holes, for they are positioned close to the locations of the holes. On the remaining components, this does not seem to occur with such a profound impact.

Lack of experience in Abaqus modelling, along with short time for the necessary work dictated composite inserts could not to be considered in the models, however their use would

possibly reduce composite plate stress and deformation for the reasons previously mentioned, although having a negative impact on system mass.

While the chosen CFRP has a relatively high Young Modulus (230 GPa), a higher modulus Carbon Fibre could also have been chosen. The employment of such a material would also have resulted in decreased strain results. The results on the suggested composite concepts regarding stress and strain can then be seen as the worst case scenario; however they are not when considering mass. As previously mentioned, the introduction of composite inserts would result in an increase in mass.

5.2 Comparison with other propulsive systems

5.2.1 Contained Energy and Specific Energy determination

This section discusses the calculations required to determine the specific energy of the metal end plate systems as well as the ones suggested from the composite concepts. The aim is to propose a comparison between them, and lastly a comparison with a typical ICE gasoline system will be attempted. The objective is to determine the feasibility of the Fuel Cell system with the proposed modifications. Only the pre-curvature plate concept, the composite plate best performer, will be considered for the reasons previously stated.

Table 27: PM 8 kW, PM 4 kW and proposed combination masses

FC stack	**Mass (kg)**
PM 4 kW	9,2
PM 8 kW	14,6
$2 \times 8\ kW + 1 \times 4\ kW$	38,4

Since aluminium was assumed to be the material of the Proton Motor 8 and 4 kW FC systems, the calculus to determine the mass of the remaining components within the stack will be made taking into account the aluminium end plate masses. Table 27 provides the mass for the aluminium FC with one, and two end plates, along with the end plate mass ratio, i.e., the mass of the plate divided by total stack mass. Furthermore, it provides the mass of the remaining components within the stack.

Table 28: Mass ratio of 2 end plates and determination of the mass of the remaining components

	1 EP mass (kg)	2 EP mass (kg)	EP 8 kW mass ratio (%)	EP 4 kW mass ratio (%)	Remaining mass 8 kW (kg)	Remaining mass 4 kW (kg)
Aluminium Concept mass (kg)	2,005	4,010	27,47	43,59	10,59	5,19

The total stack masses for the steel and CFRP are obtained by adding the remaining masses calculated before, with the mass of both end plates. The resulting total stack masses of the steel and CFRP end plate systems are given in Table 29.

Table 29: Total mass for the steel and CFRP Plate 4 and 8 kW FC stack

End Plate Concepts	1 EP mass (kg)	2 EP mass (kg)	FC stack mass 8 kW (kg)	FC stack mass 4 kW (kg)
Steel	5,794	11,588	22,178	16,778
CFRP	0,776	1,552	12,142	6,742

Thus, the total stack mass for each end plate material, along with the mass ratio of each for both 8 and 4 kW stacks, as in Table 30.

Table 30: Total stack mass for aluminium, steel and CFRP

	8 kW mass (kg)	EP mass ratio 8 kW (%)	4 kW mass (kg)	EP mass ratio 4 kW (%)
Aluminium	14,600	27,47	9,200	43,59
Steel	22,178	52,25	16,778	69,07
CFRP chosen	12,142	12,78	6,742	23,02

Having determined the FC stack mass for each of the considered materials, it becomes possible to estimate the mass of the global system, with the aim of determining the available mass for fuel, $m_{fuel\_available}$. Knowing that the available mass for propulsion established in the hypothesis section must contain every required component/sub-system for the propulsion, wherein the FC case comes as follows: the mass of the electric motor, m_{EM}, the FC stack mass, m_{FC_stack}, the balance of plant mass, m_{BoP}, along with the $m_{fuel\_available}$, as in Equation 5.1.

$$m_{propulsion} = m_{EM} + m_{FC\_stack} + m_{BoP} + m_{fuel\_available} \quad \text{Equation 5.1}$$

Being that the $m_{fuel\_available}$ is the only unknown parameter, one can easily determine it for each material case, as shown in Table 31.

Table 31: Calculation of the available mass for fuel (H_2) for the FC propulsive system

	Available propulsion mass (kg)	EM mass (kg)	FC stack mass (kg)	BoP mass (kg)	Available mass for Fuel (kg)
Aluminium	70	3	38,4	2,5	26,100
Steel			61,134		3,366
Chosen CFRP			31,026		33,474

Recalling the gravimetric targets of the DOE for a 700 bar H_2 vessel, stated in the hypothesis in Section 2.7, it is now possible to determine the contained energy by multiplying the available mass for fuel by the specific energy of each of the gravimetric goals, as seen in Equation 5.2 and Equation 5.3.

$$Contained\ Energy\ (5{,}5\%) = 1{,}832\ kWh/kg \times m_{fuel_{available}} \quad \text{Equation 5.2}$$

$$Contained\ Energy\ (7{,}5\%) = 2{,}498\ kWh/kg \times m_{fuel_{available}} \quad \text{Equation 5.3}$$

Then, recalling Equation 2.65, it is possible to determine the specific energy by dividing the result for the total propulsive system mass, as shown in Equation 5.4 and Equation 5.5.

$$Specific\ Energy\ (5{,}5\%) = \frac{Contained\ Energy\ 5{,}5\%}{m_{propulsion}} \quad \text{Equation 5.4}$$

$$Specific\ Energy\ (7{,}5\%) = \frac{Contained\ Energy\ 7{,}5\%}{m_{propulsion}} \quad \text{Equation 5.5}$$

The results for the contained energy considering both gravimetric targets, as well as Specific energy, for the three considered materials are shown in Table 32.

Table 32: Contained energy and specific energy for the aluminium, steel and CFRP FC stacks, according to the gravimetric targets of the DOE

	Energy contained in H2 5,5% (kWh)	Specific Energy 5,5% (kWh/kg)	Energy contained in H2 7,5% (kWh)	Specific Energy 7,5% (kWh/kg)
Aluminium	47,802	0,683	65,185	0,931
Steel	6,165	0,088	8,407	0,120
CFRP chosen	61,308	0,876	83,601	1,194

Table 33 shows the resulting values for the same parameters seen in Table 32, considering a 60% overall efficiency for the FC propulsive system.

Table 33: Contained energy and specific energy for the aluminium, steel and CFRP FC stacks, according to the gravimetric targets of the DOE, considering 60% overall efficiency

FC system, considering 60% efficiency		Energy contained in H2 5,5% (kWh)	Specific Energy 5,5% (kWh/kg)	Energy contained in H2 7,5% (kWh)	Specific Energy 7,5% (kWh/kg)
	Aluminium	28,681	0,410	39,111	0,559
	Steel	3,699	0,053	5,044	0,072
	CFRP chosen	36,785	0,525	50,161	0,717

In order to make a comparison with an ICE, the same computational procedure as before is required to be performed. Recalling Equation 5.1, the calculation of the available mass for fuel (gasoline), $m_{fuel\_available\_ICE}$, only now one has to consider the ICE mass, m_{ICE}, the generator mass, $m_{generator}$, as in Equation 5.6.

$$m_{propulsion} = m_{ICE} + m_{generator} + m_{fuel\_available\_ICE} \quad \text{Equation 5.6}$$

Again, resolving considering $m_{fuel\_available\_ICE}$ as unknown, results in the values in Table 34.

Table 34: Determination of the available mass for fuel (gasoline) for the ICE propulsive system

Available Propulsion mass (kg)	ICE mass (kg)	Generator mass (kg)	Available mass for fuel (kg)
70	10,7	3,5	55,8

Considering the fuel (gasoline) to have a gravimetric specific energy of 8 kWh/kg, as stated in the hypothesis, and multiplying it by the available mass for fuel, as in Equation 5.7.

$$Contained\ Energy = 8\ kWh/kg \times m_{fuel_{available}}\_ICE \quad \text{Equation 5.7}$$

The calculus of the specific energy of the ICE is depicted in Equation 5.8.

$$Specific\ Energy\ (ICE) = \frac{Contained\ Energy\ ICE}{m_{propulsion}} \quad \text{Equation 5.8}$$

The results are shown in Table 35.

Table 35: Contained energy and specific energy of the ICE propulsive system

ICE propulsive system	Energy contained in Fuel (kWh)	Specific Energy (kWh/kg)
	446,4	6,377

Finally, considering an overall system efficiency of 30% results in:

Table 36: Contained energy and specific energy of the ICE propulsive system, considering 30% overall system efficiency

ICE system, considering 30% efficiency	Energy contained in Fuel (kWh)	Specific Energy (kWh/kg)
	133,920	1,913

Finally, having calculated the available and specific energy for all system, it is possible to make a comparison between the four. Figure 64 and Figure 65 comprise a comparison between the available energy and specific energy, respectively, of the analysed systems.

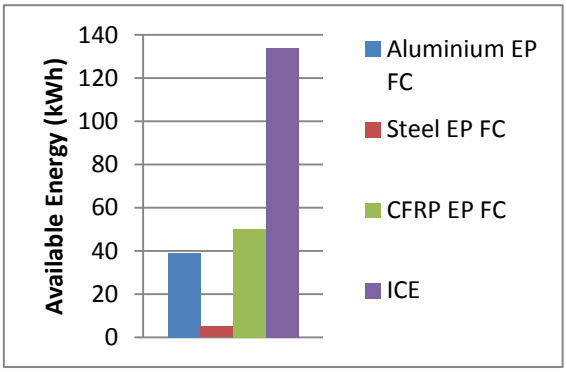

Figure 64: Available energy of the considered FC systems with different EP materials, as well as ICE system

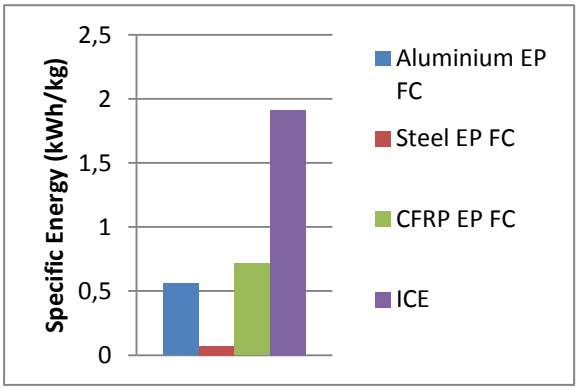

Figure 65: Specific energy of the considered FC systems with different EP materials, as well as ICE system

The steel end plate achieves an insignificant specific energy, proving that it was definitely not suitable for the considered stack power design. The ICE system is by far the one that achieves the biggest specific energy, having almost 2,7 times more than the CFRP end plate stack, as seen in Table 37.

Table 37: Comparison Specific Energy ICE-CFRP FC

	Specific Energy (Wh/kg)	Ratio ICE/FC
ICE	1,913	2,667
CFRP EP FC	0,717	

Nevertheless, the CFRP succeed in achieving a 28,30% increase in specific energy, facing the used aluminium plate, as seen in Table 38.

Table 38: Comparison Specific Energy CFRP FC-Al FC

	Specific Energy (Wh/kg)	Ratio CFRP EP/Al EP
CFRP EP FC	0,717	1,283
Aluminium EP FC	0,559	

The Specific Energy, along with the available energy, in the ICE system is far greater (almost 2,7 fold) than that of the fuel cell. Even if with significant mass reduction, the Fuel Cell cannot yet achieve a sufficient result to match the conventional ICE system. However, significant mass reduction, and subsequent increase in Specific Energy was achieved. In fact, the increase in Specific Energy and Available Energy was of 28,30%. Even though no assumption or result validation was performed, it has been proven that the suggested composite material concepts can bring a very interesting improvement to FC systems. Note that there were several critical assumptions made in this dissertation. Result validation requires a validation of those assumptions.

30% efficiency was considered for the ICE system, however the de-rating of the ICE engine, i.e., the selection of a higher rated power engine, so as to obtain reliability and durability would result in increased consumption, thus reducing efficiency. Perhaps, considering a smaller efficiency would be more accurate, and would realistically shorten the gap between FC and the ICE system.

6. Conclusions and Future Work

6.1 Conclusions

The prediction and awareness of the structural behaviour of parts with relatively complex geometries, used in fuel cell systems, was performed through the use of finite element numerical modelling. The outcome enabled the selection of the assumed best performing concept regarding mass, as well as stress-deflection uniformity within a group of previously suggested concepts. The selected concept was thereafter used in the calculation of the specific energy to determine whether this modification would make feasible, merely from a technological perspective, an implementation of a Fuel Cell system in an unmanned aerial aircraft.

The best performing concept managed to achieve a considerable improvement in specific energy facing current FC end plate concepts, however it also showed that FC systems are not yet viable as the propulsive system of an UAV when compared to currently used ICE systems. Nevertheless, this improvement is hoped to have shown that there is significant room for improvement, for this area of study appears to have been somewhat forgotten when it comes to fuel cell research.

There are however several implications regarding this study. There were a significant number of assumptions made throughout this project that influenced the obtained results. Nevertheless, there is the awareness that, with such limited time, and since some of those assumptions had to be made due to the limited availability of critical technical information, work on this subject could not have been done differently. Having only been made commercially available recently, it is still a considerably arduous task to obtain that detailed information regarding fuel cell systems online or through any other source, for that matter. If implementation of the concepts here proposed were to be considered, all of the assumptions made would have to be thoroughly confirmed with the selected FC manufacturer, or with a proper expert on the subject.

In fact, having failed in finding a suitable FC system for the required power, which in turn led to the necessity of selecting a combination of several smaller systems, decreased significantly the chance of proving FC viability facing conventional systems. It can be naturally assumed that the mass sum of a combination of smaller systems, far exceeds the mass of the single equivalent system.

One critical assumption made early in this report, was not to consider the battery mass. As mentioned previously in this report, FC systems intended for transportation applications require a stabilizing element which can be achieved through hybridization, i.e., implementation of batteries for peak power instants. This was not considered in the hypothesis, or in the performed calculations. Even though the battery system would not have

to be as heavy as in a purely electric aircraft, its consideration could have led to further unexplored differences when facing conventional systems: i.e. how does increasing battery/supercapacitor weight reduce the total amount of power required in the FC and what is the net weight change? Or, how could alternative strategies, such as the jettisoning of a take-off battery pack change the overall system performance.

There is awareness that the obtained results of the numerical model may not be trustworthy, and may not represent its physical reality. Considering for instance the shoe box concept, it would naturally be very hard to attain in reality the mechanical properties inputted in Abaqus. Therefore, some concepts may not be as robust as they are depicted in the simulation result. On the other hand, the introduction of composite inserts should also significantly enhance mechanical properties, though increasing concept mass.

Being a cutting-edge technology, research and improvements in fuel cell systems aren't always publically announced, and might take years to become available to the general public. Commercial examples of FC systems used as the propulsive systems in transportation applications where weight is critical, such as the newly released Honda Clarity, or the Phantom Eye prototype by Boeing Phantom Works, prove that there must be grounding to viability.

This work is believed to have contributed in proving that advanced materials can still play a role in FC performance improvement if alternative stack design is considered, along with innovative end plate design.

The two greatest benefits brought to the author by this study are seen to have been the skills acquired with the software Abaqus, as well as with Composite Materials. Regarding the first, even though an expert level is still far from reach, this is seen as a very satisfactory first step in finite element analysis. As for the latter, it is seen as a profoundly interesting field of study, unveiling several possibilities when it comes to structural behaviour optimization that were never devised, besides having perspectives of increasingly bigger world-wide usage. Hopefully both subjects can be further developed in the future.

6.2 Future Work

In this final sub-section suggestions of relevant studies that could be made are included if *de facto* implementation is intended. Moreover, it also introduces a concept that engages the hypothesis with a different approach for stack fixation. This concept is further described in Section 6.2.1.

Recommendations for further research are as follows.

A suitable FC system regarding required power should be selected. The selection of such a system would certainly enable greater improvement than the one here achieved through the combination of several smaller systems.

A careful manufacturing processes analysis for the suggested concepts should be made, so as to determine the best way to guarantee the best possible mechanical properties.

A factor that greatly influences mechanical behaviour is the mechanical properties of the graphite block material. The assumption needs validation if results are intended to be accurate. The graphite block concept itself is being re-assessed and a further study on the concepts involving metal plate stacks is justified.

A thermal analysis should be performed before the introduction of the suggested plates. Metal end plates should have a better performance at dissipating heat than its composite counterparts, which might have a negative influence on FC performance. Perhaps a resizing of the cooling system would be in order. Furthermore, a conductivity analysis should also be performed.

No study was found regarding aircraft acceleration impact on fuel cell functioning. In the case of a small aircraft, where acceleration is not significant, perhaps this is not important, however, if by any chance in a near future fuel cells are employed on larger, as well as faster aircrafts this could be a decisive issue.

Fixation components, such as bolts, screws and washers, have demonstrated to pose as a significant part in the total FC stack mass. An interesting approach that was not considered in this work would be to replace the materials for lighter ones that could naturally ensure the same clamping properties.

For all of these matters, the introduction of composite plates to the FC system should be accompanied by a performance analysis. That is to say, that a cell potential difference vs current density plot should be constructed and compared to existing solutions, to ascertain a possible positive or negative impact on fuel cell performance.

It was mentioned early on that the work here performed would only be concerned in proving FC viability as the propulsive system of an UAV from a technological point of view, however no implementation is possible if a proper cost analysis hasn't been performed. That is why a recommendation for future work is to perform a cost analysis covering all possible implications here suggested.

Needless to say that experimental validation is naturally of the greatest importance, so as to verify the obtained numerical results.

6.2.1 Filament Winding concept

INEGI has a considerable experience on the filament winding (FW) manufacturing process, for that matter an alternative concept for stack fixation involving filament winding was

suggested. The concept is of a very basic nature and was added to this report with the awareness of all the conceptual problems involved, as well as practical implementation implications. It should be seen as a suggestive contribution for future work, rather than a thoroughly developed concept, and that is the reason why it is included in this final section, rather than being present in Sections 14.

A proper development would require expertise in filament winding, as well as a considerable amount of time, both were however unavailable.

The great obvious advantage of this concept would naturally be to make the screw connections unnecessary, since, recalling Figure 9, screw connections represent 17% of the total stack weight, which can be seen as a significant part of the total stack mass.

Some implications if implementation of the suggest concept is considered can be the following:

- System maintenance: FC systems require regular maintenance (every 500-1000h); the FW tube would have to be destroyed for every invasive maintenance operation, and stack rewound.
- Feed hole positioning:
- Manufacturing: positioning of mandrel
- Heat management: extra coverage would probably result in decreased heat dissipation. Cooling system would most likely have to be resized
- Stack fixation during winding
- etc.

Figure 66 demonstrates, in a very basic manner, the intended assembly configuration for this concept. It should be noted that fibre orientation seen in Figure 66 does not represent the proposed fibre orientation. It only intends to depict a carbon fibre part, and it was done as so because there was no alternative in the Solid Works rendering options.

Figure 66: Filament Winding concept assembly Solid Works rendering

A very simple model was performed in Abaqus, in order to raise some awareness over the structural viability of the proposed suggestion. Again, this model is a very inaccurate one, and

should definitely not be seen as a reliable analysis of the mechanical behaviour of the suggested concept.

Table 39 shows the figure of each part used in this model, along with the sketching procedure.

Table 39: Part description for FW model

Component		Procedure
FW box	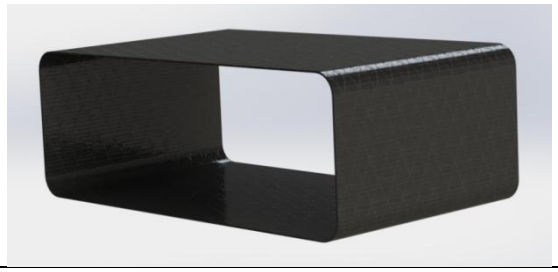	Sketched as shell in Abaqus
Composite cover		Sketched as shell in Abaqus
Reinforcement		Sketched as shell in Abaqus

The general dimensions of the FW box sketch are available in Figure 67. Thereafter, an extrude of 260 mm was considered.

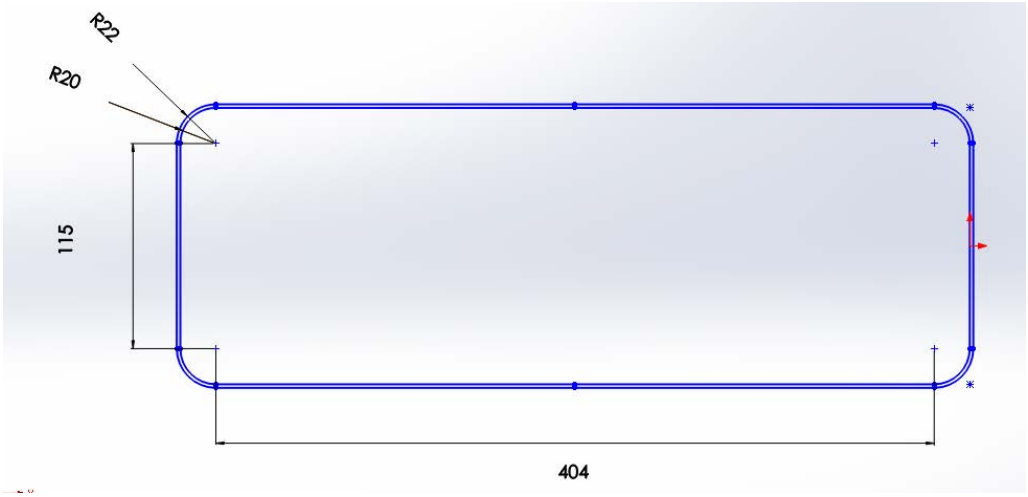

Figure 67: General dimensions of the FW box

Table 40 comprises the used material for each of the part considered in this model.

Table 40: Material definition for the used parts in the FW model

Part/Assembly		Material
FW tube	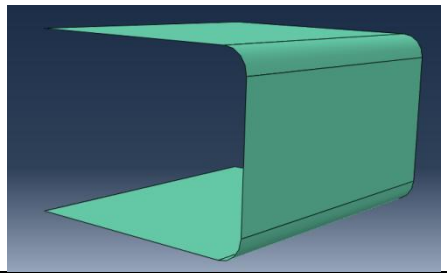	CFRP
Reinforcement	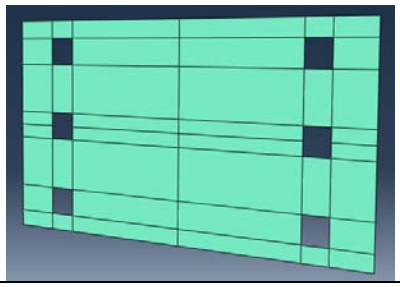	CFRP
Graphite Block	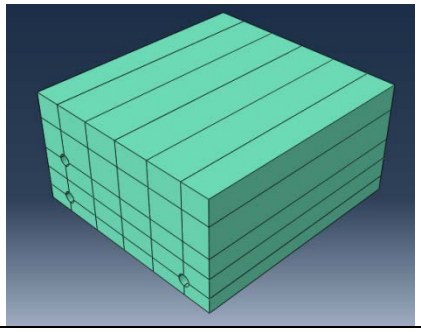	Graphite Block Assumption Material
Composite Cover	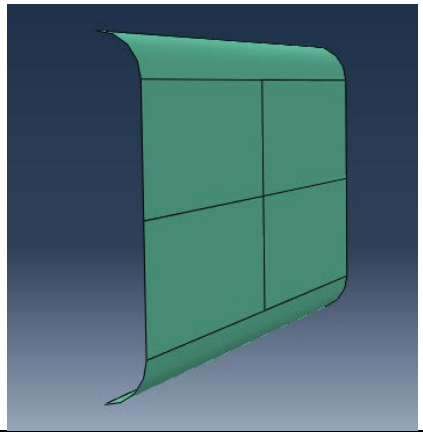	CFRP

The FW tube was considered to be winded in a 90º orientation, as seen in Figure 68. The light blue arrows indicate the fibre's direction.

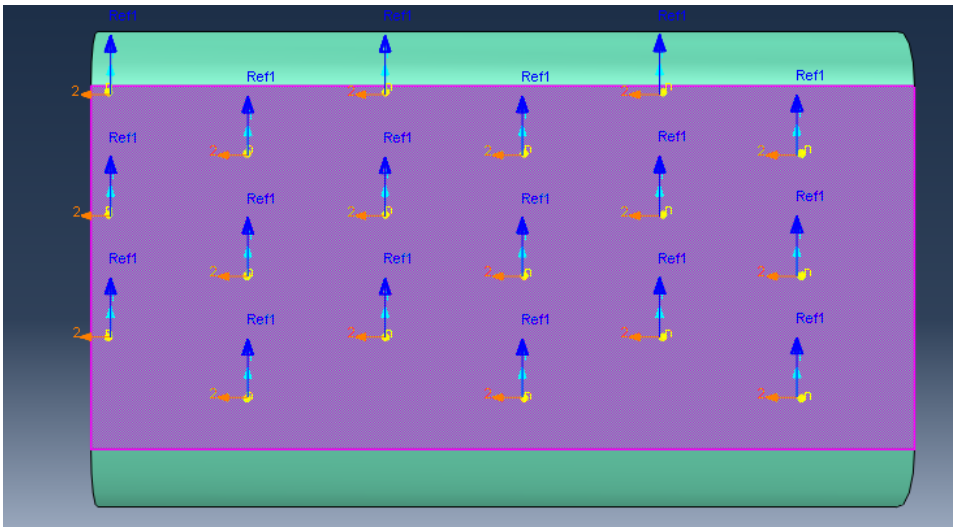

Figure 68: FW tube fibre orientation

Table 41 describes the stacking sequence for each part, ply thickness and resulting part thickness

Table 41: Carbon/epoxy stacking sequence and ply thickness

Component	Carbon/epoxy composite		
	Stacking Sequence	Ply thickness (mm)	Resulting part thickness (mm)
FW tube	$[90]_{10}$	0,200	2
Composite cover	$[0/90]_{25}$	0,200	10
Reinforcement	$[0/90]_{25}$	0,200	10

In the likeness of the produced model for the suggested conceptual plates in Section 1, only half of the stack was modelled. Figure 69 is a representation of the model.

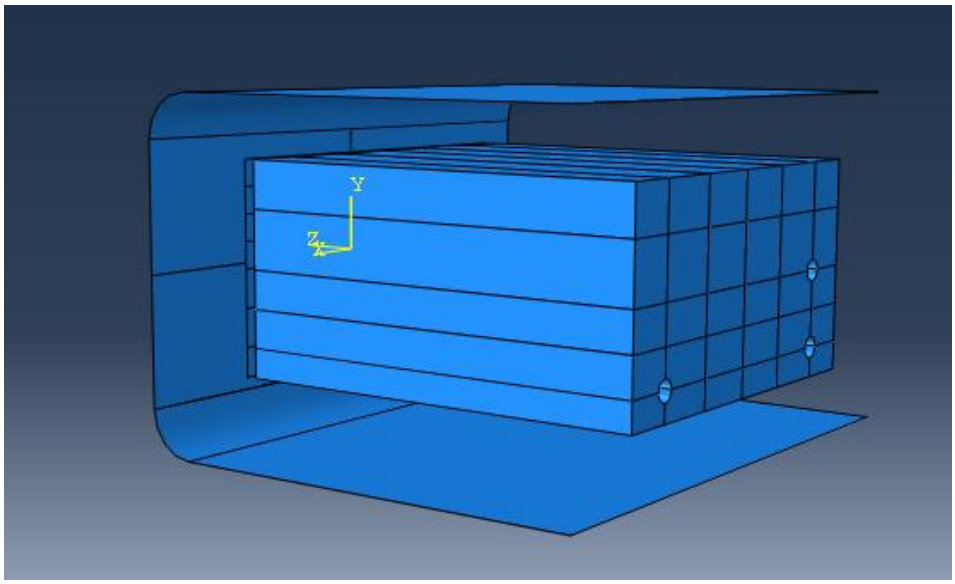

Figure 69: FW half stack assembly in Abaqus

Nevertheless, a different approach regarding applied load and boundary conditions was performed. As seen in Figure 70, the load (represented by the orange arrows pointing at the

red surface) is applied on the graphite block symmetry face. The filament winding tube is fixed in the edges of the symmetry plane (orange and blue triangles), and U1 and U2 (x and y) displacements are limited on the top and bottom sides (orange triangles), as seen in Figure 70.

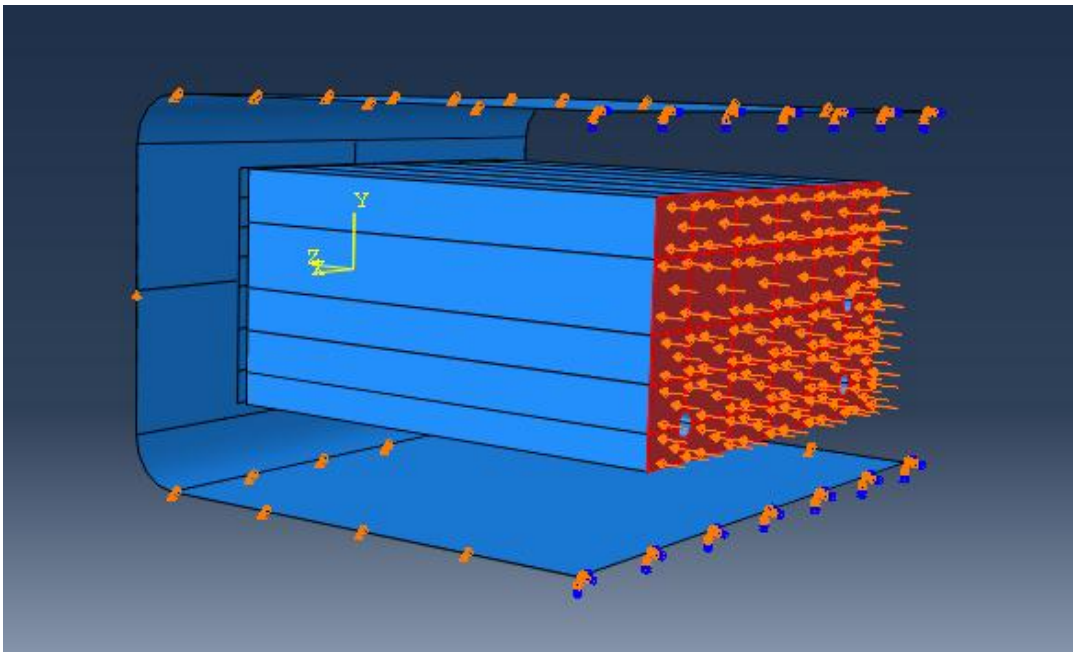

Figure 70: Load and boundary conditions in the FW model

Results

This part describes the results and attempts a comparison with the previously presented concepts.

Table 42 describes the mass of the parts used in this model.

Table 42: Mass of the parts used in the FW model

Part	Mass (kg)
Filament Winding	0,450
Composite reinforcement	0,249
Composite cover	0,712
Total assembly	1,412

Since this approach only considers half of the model, the total mass reached in Table 42 must be multiplied by 2, thus reaching a total mass of 2,823 kg. It should be noted that this mass exceeds the 1,552 kg mass of the 2 pre-curvature EPs, however in this case, the mass of fixation components is nonexistent.

If considering that this solution leads to non necessity of the fixating elements, then a significant mass reduction can be achieved. The mass weight of the fixating elements is 17%, according to [5]. Recalling Figure 9, the mass reduction should be as in Equation 6.1 and Equation 6.2.

In order to make a comparison with the end plate models, the sum of masses of the parts considered in the FW model is hereon named two end plate equivalent mass (2 EP equivalent mass). As mentioned previously, Table 45 comprises the FC stack mass for the FW concept for both 8 and 4 kW systems.

Table 45 comprises the equivalent mass, as well as the total 4 and 8 kW FC stack mass. Recalling Table 28, both stack masses were obtained through the sum of equivalent mass with the assumed remaining mass.

In order to determine the remaining mass for both stacks, the performed calculations were to subtract the assumed remaining mass for the aluminium end plate stack with 17% of the total stack mass (see Equation 6.1 and Equation 6.2) for both 8 and 4 kW systems, as in Equation 6.3 and Equation 6.4, respectively.

$$m_{fixation\ components\ 8kW} = 17\% \times m_{8\ kW} \quad \text{Equation 6.1}$$

$$m_{fixation\ components\ 4kW} = 17\% \times m_{4\ kW} \quad \text{Equation 6.2}$$

$$m_{remaining\ fw\ 8kW} = m_{remaining\ 8kW} - m_{fixation\ components\ 8kW} \quad \text{Equation 6.3}$$

$$m_{remaining\ fw\ 4kW} = m_{remaining\ 4kW} - m_{fixation\ components\ 4kW} \quad \text{Equation 6.4}$$

Table 43 and Table 44 comprise the mass of the remaining components in both FW 8 kW and 4 kW systems, respectively.

Table 43: Determination of remaining mass for the FW 8 kW stack mass

PM 8 kW mass (kg)	$m_{fixation\ components\ 8kW}$ (kg)	Remaining mass 8 kW	Remaining mass fw 8 kW
14,6	2,482	10,590	8,108

Table 44: Determination of remaining mass for the fw 4 kW stack mass

PM 4 kW mass (kg)	$m_{fixation\ components\ 4kW}$ (kg)	Remaining mass 4 kW (kg)	Remaining mass fw 8 kW (kg)
9,2	1,564	5,190	3,626

As mentioned previously, Table 45 comprises the FC stack mass for the FW concept for both 8 and 4 kW systems.

Table 45: Equivalent mass for 2 EP and FC stack mass for the 8 kW and 4 kW considering the FW model

End Plate Concepts	2 EP equivalent mass (kg)	FC stack mass 8 kW (kg)	FC stack mass 4 kW (kg)
FW concept	2,653	10,761	6,279

Table 46 comprises the mass of the two end plate equivalent mass, as well as its relative weight in the stack.

Table 46: EP equivalent mass ratio for the 8 and 4 kW stacks

	EP equivalent mass ratio 8 kW (%)	EP equivalent mass ratio 4 kW (%)
FW concept	24,65	42,25

Considering the FC stack mass to be the sum of two 8 kW stacks andone of 4 kW, it is possible to achieve total stack mass, and available mass for fuel, as in .

Table 47: Calculus of the available mass for fuel (H2) for the FC propulsive system in the FW model

	Available propulsion mass (kg)	EM mass (kg)	FC stack mass (kg)	BoP mass (kg)	Available mass for Fuel (kg)
FW concept	70	3	27,800	2,5	36,700

In likeness of before, and considering the calculations performed previously through Equation 5.2 and Equation 5.3, one can obtain the contained energy and specific energy considering both DOE targets, see Table 48.

Table 48: Contained energy and specific energy for the aluminium, steel and CFRP FC stacks, according to the gravimetric targets of the DOE for the FW model

	Energy contained in H2 5,5% (kWh)	Specific Energy 5,5% (kWh/kg)	Energy contained in H2 7,5% (kWh)	Specific Energy 7,5% (kWh/kg)
FW stack	67,215	0,960	91,657	1,309

Again, considering an overall 60% efficiency for the FC system, the intended comparing parameters are reached, see Table 49.

Table 49: Contained energy and specific energy for the aluminium, steel and CFRP FC stacks, according to the gravimetric targets of the DOE, considering 60% overall efficiency for the FW model

FC system, considering 60% efficiency		Energy contained in H2 5,5% (kWh)	Specific Energy 5,5% (kWh/kg)	Energy contained in H2 7,5% (kWh)	Specific Energy 7,5% (kWh/kg)
	FW stack	40,329	0,576	54,994	0,786

Reaching a value of 0,786 kWh/kg, this attempt of modelling the proposed FW concept achieved greater specific energy than that of the aluminium EP FC, but has also achieved one greater than the previously suggested CFRP EP FC, see Figure 71 and Figure 72.

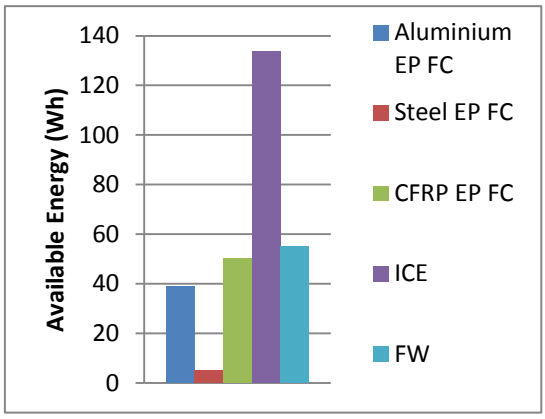

Figure 71: Available energy of the considered FC systems, as well as the FW concept and the ICE system

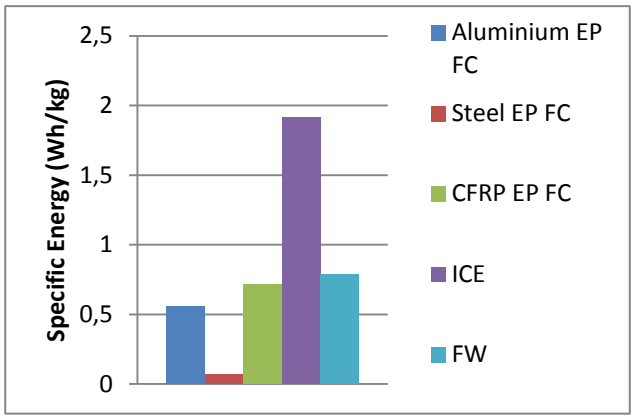

Figure 72: Specific energy of the considered FC systems, as well as the FW concept and the ICE system

This concept is still of a very basic nature, however it has proven that it may be an interesting alternative to FC stack fixation. Naturally, solutions for all the implications mentioned at the beggining of this chapter, and for any other that could come up, would have to be properly developped.

7. References

[8, 9, 12, 13, 19, 21, 23, 28, 29, 38-45]

1. Defense, O.o.t.S.o.D.-D.o. *Unmanned Aerial Vehicles Roadmap 2000-2025*. 2001.
2. Asghari, S., M.H. Shahsamandi, and M.R. Ashraf Khorasani, *Design and manufacturing of end plates of a 5 kW PEM fuel cell.* International Journal of Hydrogen Energy, 2010. **35**(17): p. 9291-9297.
3. Rungsima Yeetsorn, M.W.F.a.C.T., *A Review of Thermoplastic Composites for Bipolar Plate Materials in PEM Fuel Cells, Nanocomposites with Unique Properties and Applications in Medicine and Industry*. 2011: InTech.
4. Wang, X., Y. Song, and B. Zhang, *Experimental study on clamping pressure distribution in PEM fuel cells.* Journal of Power Sources, 2008. **179**(1): p. 305-309.
5. Mawdsley, J.R., et al., *Composite-coated aluminum bipolar plates for PEM fuel cells.* Journal of Power Sources, 2013. **231**(0): p. 106-112.
6. Li, X. and I. Sabir, *Review of bipolar plates in PEM fuel cells: Flow-field designs.* International Journal of Hydrogen Energy, 2005. **30**(4): p. 359-371.
7. Middelman, E., et al., *Bipolar plates for PEM fuel cells.* Journal of Power Sources, 2003. **118**(1–2): p. 44-46.
8. Scott, J.H., *The Development of Fuel Cell Technology for Electric Power Generation: From NASA's Manned Space Program to the "Hydrogen Economy".* Proceedings of the IEEE, 2006. **94**(10): p. 1815-1825.
9. Hoogers, G., *Fuel Cell Technology Handbook*. 2003: Boca Raton [etc.] : CRC Press.
10. Drebushchak, V.A., *Universality of the emf of thermocouples.* Thermochimica Acta, 2009. **496**(1–2): p. 50-53.
11. Barbir, F., T. Molter, and L. Dalton, *Efficiency and weight trade-off analysis of regenerative fuel cells as energy storage for aerospace applications.* International Journal of Hydrogen Energy, 2005. **30**(4): p. 351-357.
12. Organization, N.A.T.O.-S.a.T., *Manwearable Power Study Group*.
13. Bagotsky, V.S., *Fuel Cells: Problems and Solutions*. 2 ed. 2012: John Wiley & Sons.
14. Energy, U.S.D.o.E.-E.E.R. *Fuel Cells - Types of Fuel Cells*. 2011; Available from: http://www1.eere.energy.gov/hydrogenandfuelcells/fuelcells/fc_types.html.
15. Haile, S.M., *Fuel cell materials and components.* Acta Materialia, 2003. **51**(19): p. 5981-6000.
16. Lin, C.-W., et al., *Dynamic mechanical characteristics of five elastomeric gasket materials aged in a simulated and an accelerated PEM fuel cell environment.* International Journal of Hydrogen Energy, 2011. **36**(11): p. 6756-6767.

17. Kim, M., et al., *Bipolar plates made of plain weave carbon/epoxy composite for proton exchange membrane fuel cell.* International Journal of Hydrogen Energy, 2012. **37**(5): p. 4300-4308.

18. Yu, H.N., et al., *Composite endplates with pre-curvature for PEMFC (polymer electrolyte membrane fuel cell).* Composite Structures, 2010. **92**(6): p. 1498-1503.

19. Laboratory, H.U.S.D.o.E.N.E.T., *Fuel Cell Handbook*. Reprinted from the 2000 edition ed. 2005: Honolulu : University Press of the Pacific, cop. 2005.

20. Hua, T.Q., et al., *Technical assessment of compressed hydrogen storage tank systems for automotive applications.* International Journal of Hydrogen Energy, 2011. **36**(4): p. 3037-3049.

21. Ananthachar, V. and J.J. Duffy, *Efficiencies of hydrogen storage systems onboard fuel cell vehicles.* Solar Energy, 2005. **78**(5): p. 687-694.

22. Energy, U.S.D.o.E.-E.E.R. *Hydrogen Storage*. Ful Cell Technologies Program, 2011.

23. Najib, W.B., *Fuel Cell Powered AUVs; An Overview*, 2005, INEGI - Unidade de Materiais Compósitos; Universidade de Aveiro.

24. CEA, C., *Hydrogen, new energy technologies - Onboard storage of hydrogen.* The Hydrogen Pathway, 2004-2005(No. 50/51).

25. Francescato, P., et al., *Comparison of optimal design methods for type 3 high-pressure storage tanks.* Composite Structures, 2012. **94**(6): p. 2087-2096.

26. Klell, M., *Handbook of Hydrogen Storage*. Storage of Hydrogen in the Pure Form. 2010: WILEY-VCH Verlag GmbH & Co. KGaA, Weinheim.

27. FG, H., *Neural network control of a parallel hybrid-electric propulsion system for asmall unmanned aerial vehicle*, 2005, University of California: USA.

28. Hung, J.Y. and L.F. Gonzalez, *On parallel hybrid-electric propulsion system for unmanned aerial vehicles.* Progress in Aerospace Sciences, 2012. **51**(0): p. 1-17.

29. Ruddell, D.A., *WP Report - Storage Technology Report ST6: Flywheel* 2003, Investire-Network.

30. Mazumdar, S.K., *Composites Manufacturing : Materials, Product, and Process Engineering*. 2002: CRC PRESS.

31. Jones, R.M., *Mechanics of Composite Materials*. Second Edition ed. 1999.

32. Cambridge, U.o., *Mechanics of Fibre Reinforcemend Composites - Stiffness of long fibre composites*, 2004.

33. ESAComp, *Theoretical Background of ESAComp Analyses*, M. Palanterä, Editor 1999, HELSINKI UNIVERSITY OF TECHNOLOGY.

34. Frost&Sullivan, *STUDY ANALYSING THE CURRENT ACTIVITIES IN THE FIELD OF UAV*, 2007, EUROPEAN COMMISSION - ENTERPRISE AND INDUSTRY DIRECTORATE-GENERAL.

35. Group, P.M.S.p., *PM 200 Hydrogen Fuel Cell*, P.M.F.C. GmbH, Editor 2010.

36. Limited, B.M. *Developing Unmanned Aircraft Systems and Design Software*. 2012; Available from: http://www.barnardmicrosystems.com/L4E_wankel.htm.

37. Systems, D.D. *Abaqus Unified FEA*. 2013; Available from: http://www.3ds.com/products-services/simulia/portfolio/abaqus/latest-release/.

38. Blomen, L.J.M.J., Mugerwa, Michael N., *Fuel Cell Systems*. 1993.

39. El Chaar, L., L.A. lamont, and N. El Zein, *Review of photovoltaic technologies.* Renewable and Sustainable Energy Reviews, 2011. **15**(5): p. 2165-2175.

40. Fazelpour, F., et al., *Considerable parameters of using PV cells for solar-powered aircrafts.* Renewable and Sustainable Energy Reviews, 2013. **22**(0): p. 81-91.

41. Guimarães, S.M.d.A.L., *Estudo do Desempenho de Células de Combustível de Membrana de Permuta Iónica*, in *Faculdade de Engenharia da Universidade do Porto*2006, Universidade do Porto: Porto.

42. Larminie, J.D., Andrew, *Fuel cell systems explained*. 2nd ed ed.: Chichester : John Wiley & Sons, cop. 2003.

43. Parida, B., S. Iniyan, and R. Goic, *A review of solar photovoltaic technologies.* Renewable and Sustainable Energy Reviews, 2011. **15**(3): p. 1625-1636.

44. Pires, I.A.E., *ANÁLISE E PROJECTO DE UMA CÉLULA DE*

AVIÓNICOS PARA O UAV ALFA, 2009, Academia da Força Aérea.

45. Thomas, C.E., *Fuel cell and battery electric vehicles compared.* International Journal of Hydrogen Energy, 2009. **34**(15): p. 6005-6020.

46. Mair, W.A., *Aircraft Performance*. 1996: Cambridge University Press.

Annexes

Annexe A: Toray M40J CFRP

Annexe B:Proton Motor Data Sheet

Annexe C: Horizon Data Sheet

Annexe D: Launch Point Halbach Array EM

Annexe E: Performed Literature review

1. Photovoltaic Cells

The solar cell working principle is based on the Photovoltaic (PV) effect. Sunlight, when striking a light absorbing material present within the cell structure, imparts enough energy to some electrons to raise their energy level and thus free them. Those free electrons are then used to produce voltage through a built-in potential barrier, and used to drive current through a circuit.

A cell is grouped into modules and multiple modules can be wired together to form an array. Generally, the amount of electricity produced increases with the increase of the area of a module or array. Photovoltaic modules and arrays produce direct-current (DC) electricity. Any required voltage and current combination can be achieved by connecting in both series and parallel electrical arrangements.

The rated unit for these systems is the peak kilowatt (kWp), which represents the amount of electric power that a system is expected to deliver when the sun is directly overhead on a clear day. A defining property of a PV system is its band-gap, measured in electro-volts (eV). The band-gap is the energy gap an electron must cross in order to be promoted from the valence band to the conduction band. Also, the wider and the larger the band-gap of PV cell is, the greater is the output production voltage, since it absorbs more light. In cells with a smaller band-gap, however, the result is larger current, yet smaller output voltage. According to *Review of photovoltaic technologies*, there are currently four major types of PV technology: crystalline, thin film, compound and nanotechnology.

A solar cells' efficiency is dependent upon many environmental features and weather parameters such as humidity, wind speed, dust, temperature, shading, tilt angle, azimuth plane angle, sun intensity, etc. High relative humidity and temperature, and dust are undesirable factors in a solar cell, since they decrease efficiency. Wind can lead to increased efficiency since it causes convection heat transfer, thus lowering humidity and temperature, yet dust lifting by wind may lead to shading and efficiency decrease. As seen from Figure 73, a higher efficiency is reached for lower temperatures, independently of the solar cell type. In fact, the part of a photovoltaic energy which is not converted into electricity will appear in the heat form of energy in solar cells and elevates temperature of the cell, thus leading to greater inefficiency.

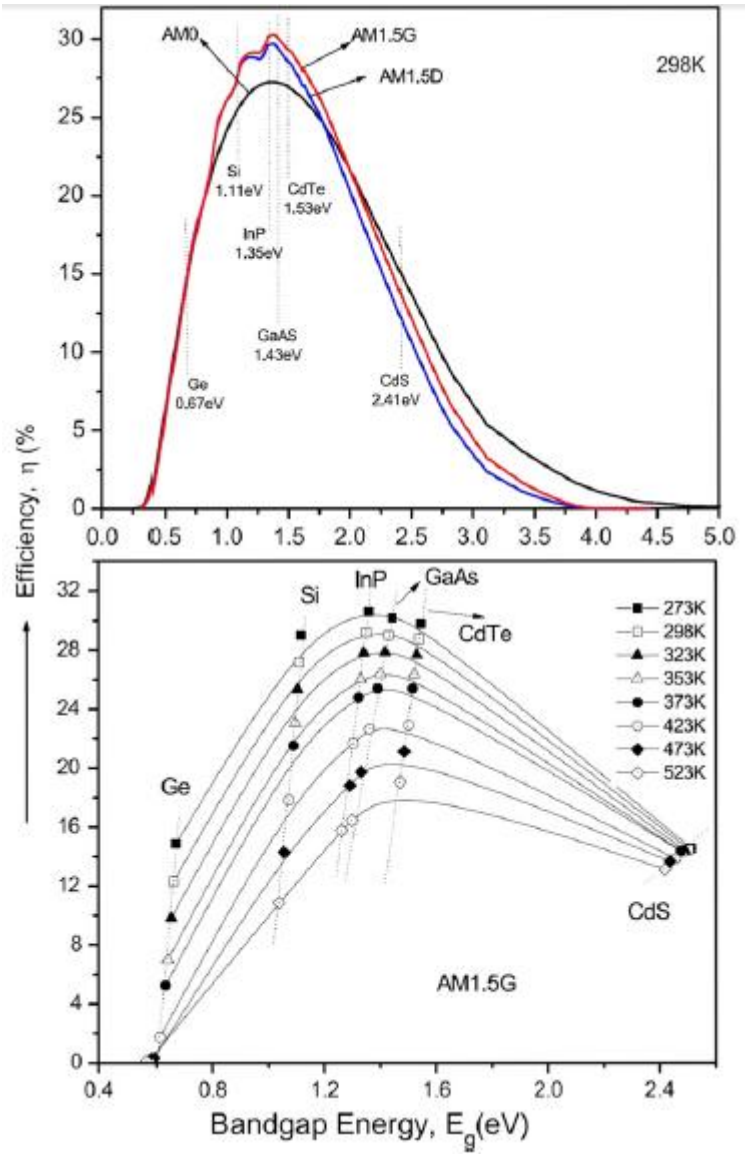

Figure 73: Dependency of the band gap, temperature and efficiency, [40]

1.1 Silicon Crystalline Structure

Having been the first generation of PV, crystalline structure hasn't however become obsolete. Instead it has been constantly developed in terms of capability and efficiency. Within this type of cell, the sub-divisions of mono- and poly-crystalline and emitter wrap through (EWT) will be further discussed.

1.1.1 Mono-Crystalline PV cells

The fact of being the most cost effective cell, naturally leads to being the most commonly used system in the market with an 80% share, nowadays. Yet, its efficiency development finds great limitation due to the fact that with its material (silicon), energy produced decreases with higher wave lengths. Furthermore, radiation with higher wave length leads to decreased efficiency caused by greater thermal dissipation and resulting heating. A efficiency of 20,4% for a module of this type of cells has been recently determined by the National Renewable Energy Laboratory (NREL).

1.1.2 Poly-Crystalline PV cells

This technology is becoming more attractive due to its manufacturing cost, despite having a lower efficiency (15%) than mono-crystalline. Another advantage of producing multi-silicon is to decrease the flaws in metal contamination and crystal structure.

1.2 Thin film technology

This type of technology consists of applying thin layers of semiconductor material to a solid backing material, such as glass or stainless steel substrate. That allows great savings in the amount of semiconductor material required for each cell when compared to silicon wafers, thus lowering the cost of production of PV cells. Common material used in thin-film cells are Gallium arsenide ($GaAs$), copper, cadmium telluride ($CdTe$), indium diselenide ($CuInSe_2$) and titanium dioxide (TiO_2). As a result of light trapping and black surface passivation with optimum silicon thickness, this technology is said to achieve 19% efficiency. One can distinguish four types within Thin-film cells, which are: amorphous silicon cell, thin poly-crystalline silicon on a low cost substrate, the copper indium diselenide/cadmium sulphide hetero-junction cell, and the cadmium telluride/cadmium suplhide hetero-junction cell.

1.2.1 Amorphous silicon

Unlike crystalline silicon, the silicon atoms in this technology are randomly located from each other, leading to a higher band-gap (1,7 eV) than crystalline silicon (1,1 eV). The larger band -gap allows a-Si cells to absorb the visible part of the solar spectrum more strongly than the infrared portion of the spectrum. There are several variations in this technology where substrates can be glass or flexible stainless steel, tandem junction, double and triple junctions, and each one has a different performance.

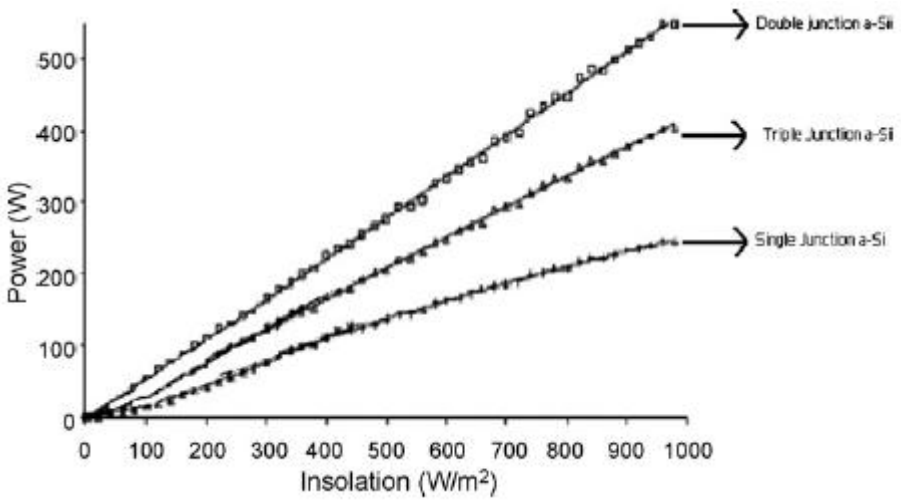

Figure 74: Variation of output with insulation for representative sub-arrays, [39]

1.2.2 Cadmium telluride or cadmium sulphide/cadmium telluride

According to *Review of Photovoltaic technologies*, Cadmium telluride ($CdTe$) has long been known to have the ideal band-gap (1,45 eV) with a high direct absorption coefficient for a solar absorber material and recognized as a promising photovoltaic material for thin-film solar cells. Furthermore, recent developments in their manufacturing process have lead to capability to reduce manufacturing cost and have made this technology extremely competitive. An issue

that needs further development regarding this PV cell is the toxicity of cadmium and related environmental issues.

1.3 Concentrator

This type of PV cell focus sunlight onto a small area of photovoltaic cells and it does so by using a large area of lenses or mirrors.

1.4 Compound Semi-conductor

This type comprises a stack of crystalline layers with different band gaps that are tailored to absorb most of the solar radiation, i.e., the various cells, each one with different band-gaps, are tuned to use the full spectrum, leading to increased efficiency.

Gallium arsenide ($GaAs$)/indium gallium phosphide ($InGaP$) multi-junction devices have reached the highest efficiency of 39% with NREL recently announcing a record 40,8% from a metamorphic triple-junction solar cell. A schematic is shown in Figure 75.

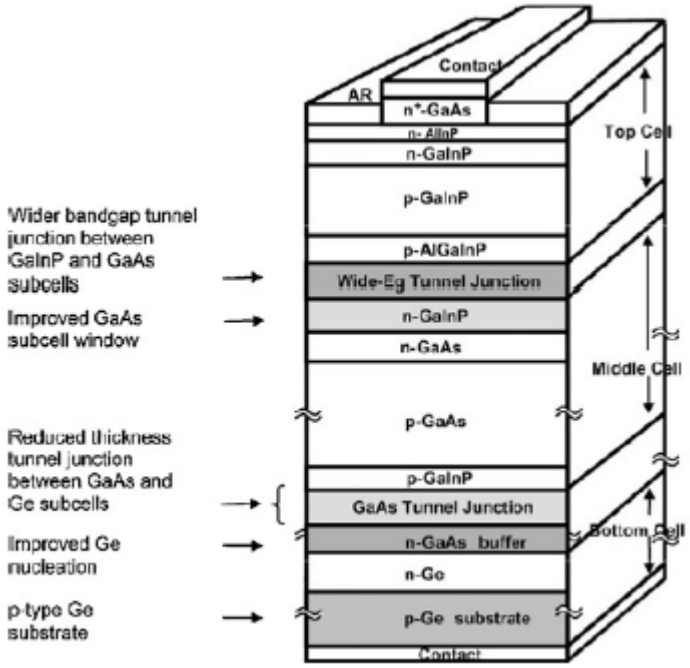

Figure 75: Epitaxial stacks of multi-junction solar cells, [39]

1.5 Nanotechnology

The introduction of nanoscale components can lessen limitations seen in other PV technologies, thanks to their ability to control the energy band-gap, providing flexibility and inter-changeability in addition to enhancing the probability of charge recombination. Devices such as nanotubes, quantum dots and hot carrier solar cells are types of nanotechnology structures that can be used for increased efficiency in solar cells.

Type	**Efficiency (%)**
Crystalline silicon (single-crystal) PV cell/module	20
Crystalline silicon (cast) PV	14

Crystalline silicon (ribbon)	13
Thin film (amorphous silicon)	8
Thin film other (special material CdTe and CIGS)	12
Concentrator PV (photovoltaic)	38

Table 50: Efficiency of the different types of PV

2. Kinetic Energy Systems

Flywheels are devices capable of storing kinetic energy through a rotating mass (rotor). The stored energy is dependent upon the mass, inertia and rotational speed of the rotor. Energy is transferred to the flywheel by applying an accelerating torque to it, increasing rotational speed. In contrast, energy is released from the device by applying a decelerating torque to a mechanical load.

2.1 Stored Energy Equation

Equation E.1 shows the way to determine the stored energy of a spinning flywheel with ω angular velocity and polar moment of inertia, J.

$$E = \frac{1}{2} \times J \times \omega^2$$ Equation E.1

$$J = \int x^2 dm_x$$ Equation E.2

$$J = m \times r^2$$ Equation E.3

$$E = \frac{1}{2} \times m \times r^2 \times \omega^2$$ Equation E.4

As Equation E.4 demonstrates, higher stored energy can be more easily achieved through high angular velocity, rather than higher mass. Given that, Equation E.5 defines the maximum angular velocity the flywheel can take, according to its tensile strength for a flywheel with mass concentrated at the rim at radius, r.

$$\sigma = \rho\, r^2\, \omega^2$$ Equation E.5

With the maximum angular velocity, ω_{max}, for a maximum tensile strength, σ_{max}, being:

$$\omega_{max} = \sqrt{\frac{\sigma_{max}}{\rho\, r^2}}$$ Equation E.6

Thus defining the maximum the maximum stored energy, E_{max}, for a given material:

$$E_{max} = \frac{1}{2} \times m \times \frac{\sigma_{max}}{\rho}$$ Equation E.7

From the last expression, one concludes that a higher stored energy can be achieved through the use of materials which combine high tensile strength with low density. compares the previously mentioned parameters with the theoretical maximum specific energy of each and reaches the conclusion that composite materials are the most suitable for kinetic energy storage through high speeds.

Table 51: Specific strength of rotor materials, [29]

	Density (kg/m^3)	Strength (MN/m^2)	Theoretical maximum specific energy (Wh/kg)
Steel (AISI 4340)	7800	1800	32
Alloy (AlMnMg)	2700	600	31
Titanium (TiAl6Zr5)	4500	1200	37
GFRP Glass Fibre Reinforced Polymer (60% vol E-glass)	2000	1600	111
CFRP Carbon Fibre Reinforced Polymer (60% vol HT Carbon)	1500	2400	222

Taking into account that the specific energy per unit mass (Equation E.8), E_m, in J/kg is:

$$E_m = \frac{1}{2} \times r^2 \times \omega^2 \ [J/kg\ ]$$ Equation E.8

Or, as a function of tensile strength and density, one reaches the theoretical maximum specific energy, and in Wh/kg, as in Equation E.9:

$$E_m = \frac{1}{2} \times \frac{\sigma}{\rho} \times \frac{1}{3600}\ [Wh/kg]$$ Equation E.9

2.2 Rotor Bearing

Being a mechanical energy storage system, minimum losses and maintenance are fundamental to achieve greater stored energy, making rotor bearing design a key aspect in Kinetic Energy Storage systems. Some commonly used examples of high specification bearings are, [29]:

- Combination of ceramic ball bearings in a steel race, with magnetic lift to increase bearing life substantially;
- Low stiffness, self balancing concept. Bearing system consisting of a passive magnetic bearing at the top, and a low loss pivot bearing at the bottom of the vertical axis;
- High-temperature superconductor (HTS) bearing with extremely low rotational loss. These bearing can reach a reduction in rotational drag more than two orders of magnitude lower than that of mechanical bearings.

2.3 Power Interface

The power interface of a KES system includes the motor/generator, a variable-speed power electronics converter, and a power controller, [29]:

- A high speed permanent magnet machine, integrated with the rotor, is usually employed as the motor/generator, also usually known as integrated synchronous generator (ISG).
- A pulse width modulated (PWM) bi-directional converter using insulated-gate bipolar transistor (IGBT) technology is usually used for the power electronics interface. Depending on the application requirements, the converter may be single stage (flywheel ISG a.c. ⇔ d.c. bus), or double stage (flywheel ISG a.c. ⇔ d.c. bus ⇔ a.c. network), according to the application requirements.
- A power controller is also required to monitor the flywheel and control the power flow.

2.4 Final Specific Energy and Power

While the theoretical specific energies achieved for composite materials in are quite attractive when compared to other storage energy devices such as fuel cells and batteries, the calculation takes only into account the flywheel itself. The complete kinetic energy storage system, i.e., flywheel hub and all of the required electrical and mechanical parts can lead to at least factor of 10 reduction in the previously calculated specific energy, leading to a somewhat disappointing specific energy, especially when compared with the mentioned alternatives. As for power density, it depends mainly upon the flywheel hub, electrical machine and power electronic interface. Figures for specific power for these systems as high as $1600\ W/kg$ have been quoted.

2.5 Manufacturing Methods of Composite rotors

Two basic methods can be used for the manufacture of flywheels in composite materials: filament-winding as well as the resin transfer moulding process (RTM), the latter leading to inferior material properties, having however the possibility of cheap mass production. The description of both fabrication methods can be found in Section 0.

3. Basic Aeronautics

In any flight, fuel is used from the moment when the engines are first started until they are shut down finally after landing at the destination. The phases to be considered in a normal flight diversion are, [46]:

1. Start engines, taxi to end of runway and wait for take-off
2. Take-off and initial climb
3. Climb to height required for start of cruise.
4. Cruise.
5. Descend to height required for start of landing approach.
6. Decelerate to approach speed.
7. Approach and land.
8. Taxi from runway to unloading point.

3.1 Basic Equations

The simple energy flight equations for take-off and cruise flight (considering steady-state) will be discussed in this section.

3.1.1 Take-off

One can start by stating that the energy required to reach an altitude h is, in ideal conditions, equal to the potential energy of being at that particular altitude, as in Equation E.10.

$$E_{spent} = E_{potential} = mgh \qquad \text{Equation E.10}$$

Where m and g are the mass of the aircraft and gravitational acceleration, respectively.

Considering drag, it is possible to say that the drag work performed due to the air resistance force caused by the relative air flow speed, equals that force, i.e., the drag force, F_{drag}, multiplied by the displacement of the aircraft, as in Equation E.11.

$$W_{drag} = F_{drag} \times displacement \qquad \text{Equation E.11}$$

Since take-off is being considered, the $displacement$ of the aircraft comes as a function of the reached altitude, h, and the corresponding ground distance covered, d_{ground}, as in Equation E.12.

$$displacement = \sqrt{h^2 + d_{ground}^2} \qquad \text{Equation E.12}$$

Considering the dynamic pressure, $p_{dynamic}$, from the Bernoulli's equation, as in Equation E.13.

$$p_{dynamic} = \frac{1}{2}\rho\, v^2 \qquad \text{Equation E.13}$$

Where ρ and v are the aircrafts' mass density and velocity, respectively.

Multiplying $p_{dynamic}$ for the cross sectional area, S, and considering the drag coefficient, c_d, one obtains F_{drag}, as in Equation E.14.

$$F_{drag} = \frac{\rho\, v^2\, S}{2\, c_d} \qquad \text{Equation E.14}$$

An approximation for the necessary energy for the aircraft to reach altitude h comes by summing $E_{potential}$ with W_{drag}, as in Equation E.15.

$$E_{required} = E_{potential} + W_{drag} \quad \text{Equation E.15}$$

3.1.2 Achievable Range in Steady State (Cruise speed) - Breguet Equation

The achievable range of an aircraft is the maximum distance it can travel between take-off and landing. Merely considering cruise flight, i.e., steady state, a simple mathematical model of the physical system will be developed, with the aim of reaching the Breguet Range Equation. As it will be demonstrated, the range finds its limitations in three areas of study: Fluids, Propulsion and Structures & Materials.

As seen in Figure 76, the force balance in steady level flight is as follows in Equation E.16 and Equation E.17.

$$T = D \quad \text{Equation E.16}$$

$$L = W \quad \text{Equation E.17}$$

Where Thrust, T, equals Drag, D, and Lift, L, equals Weight, W.

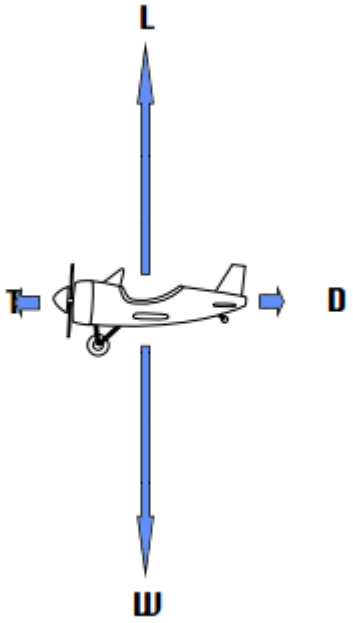

Figure 76: Force balance for an aircraft in steady level flight

From Equation E.16 and Equation E.17, one can further develop into Equation E.18:

$$W = L = D\frac{L}{D} = T\left(\frac{L}{D}\right) \quad \text{Equation E.18}$$

The variation of the aircraft's weight with time, $\frac{dW}{dt}$, is dependent upon the fuel that is burned throughout the flight as a negative relation, as seen in Equation E.19.

$$\frac{dW}{dt} = -\dot{m}_f \cdot g \quad \text{Equation E.19}$$

Where $\dot{m}_f$ is the variation of the weight of fuel with time.

Equation E.20 defines the overall propulsion system efficiency, $\eta_{overall}$, for the aircraft.

$$\eta_{overall} = \frac{propulsive\ power}{fuel\ power} \quad \text{Equation E.20}$$

Where:

$$propulsive\ power = T \cdot v\ (J/s) \quad \text{Equation E.21}$$

and

$$fuel\ power = \dot{m}_f \cdot h\ (J/s) \quad \text{Equation E.22}$$

Where v and h are the flight velocity the fuel energy per unit mass, respectively.

Thus,

$$\eta_{overall} = \frac{T \cdot v}{\dot{m}_f \cdot h} \quad \text{Equation E.23}$$

It is now possible to write the equation for the variation of Weight, in relation to the Lift-to-Drag ratio, $\left(\frac{L}{D}\right)$, and to the overall propulsion system efficiency, $\eta_{overall}$, as in Equation E.24:

$$\frac{dW}{dt} = -\dot{m}_f \cdot g = \frac{-W}{\left(\frac{L}{D}\right)\frac{T}{\dot{m}_f \cdot g}} = \frac{-W \cdot v}{\frac{h}{g}\left(\frac{L}{D}\right)\frac{T \cdot v}{\dot{m}_f \cdot h}} = \frac{-W \cdot v}{\frac{h}{g}\left(\frac{L}{D}\right)\eta_{overall}} \quad \text{Equation E.24}$$

Rewriting and integrating Equation E.24, one reaches Equation E.25:

$$\frac{dW}{W} = \frac{-v \cdot dt}{\frac{h}{g}\left(\frac{L}{D}\right)\eta_{overall}} \Rightarrow \ln W = constant - \frac{t \cdot v}{\frac{h}{g}\left(\frac{L}{D}\right)\eta_{overall}} \quad \text{Equation E.25}$$

In order to determine the $constant$ parameter, the initial conditions ($t = 0\ and\ W = W_{initial}$) are applied:

$$constant = \ln W_{initial} \quad \text{Equation E.26}$$

Resulting in the following expression for flight time (Equation E.27):

$$t = -\frac{L}{D}\eta_{overall}\frac{h}{g \cdot v}\ln\frac{W}{W_{initial}} \quad \text{Equation E.27}$$

The total flight time comes as a function of the final Weight, W_{final}, as in Equation E.28.

$$t = -\frac{L}{D}\eta_{overall}\frac{h}{g \cdot v}\ln\frac{W_{final}}{W_{initial}} \quad \text{Equation E.28}$$

The Breguet Range Equation (Equation E.29) is then reached by multiplying Equation E.28 by the flight velocity, v. This equation applies only for situations where overall efficiency, Lift-to-Drag ratio and flight velocity are constant over the flight.

$$Range = -\frac{L}{D}\eta_{overall}\frac{h}{g}\ln\frac{W_{final}}{W_{initial}} \quad \text{Equation E.29}$$

Where the $\frac{L}{D}$, $\eta_{overall}$, and $\ln\frac{W_{final}}{W_{initial}}$ parameters are dependent upon the study areas of Fluid Mechanics, Propulsion and Structures & Materials, as previously mentioned.

4. Fuel Cell

4.1 Types of Fuel Cell

Low Temperature fuel cell

Alkaline Electrolyte fuel cell

Having been the first practical fuel cell power plant, known as Bacon fuel cell after its British inventor, this type of fuel cell technology is one of the most developed. Its development was mainly done by NASA, in fact, this type of fuel cell was used in several space missions, including the Apollo Program and as the Space Shuttle's energy source.

The electrolyte is an aqueous solution of potassium hydroxide (KOH) suspended in an asbestos matrix. Depending on the necessary efficiency and durability of the intended application, the catalyst can be a relatively inexpensive nickel type or expensive noble metal platinum.

Even allowing inexpensive catalysts, the AFC faces many challenges regarding the complexity of the system and difficulties handling a liquid electrolyte. Perhaps the greatest limitation is the intolerance to non-pure reactants. Carbon monoxide, CO, and even carbon dioxide, CO_2, the latter considered inert in most fuel cells, will react with the electrolyte if in contact and permanently degrade its ionic conductivity. Therefore, atmospheric air cannot be used as an oxidant in this type of fuel cells for it has traces of the mentioned elements. Another important limitation is that water formation within the cathode. Its cause is related to the relatively low operating temperature. Even if this factor may be attractive depending on the application and by making the plant respond rapidly to step changes in power demand, water formation is a challenge that must be managed by the balance of the plant, since it may lead to dry-out or flooding of the electrolyte and, consequently, the destruction of the fuel cell.

Advantages

- Can potentially avoid the use of expensive catalysts (Platinum)
- Potentially more efficient than other systems
- Easy to carry and handle
- Can be direct fuelled
- Can accommodate a wider range of fuels, e.g. methanol, ethanol, hydrazine, glycerol, etc.

Disadvantages

- KOH being highly corrosive and hazardous leakage or inadvertent rupture of the system can be an issue
- Power density lower than PEM due to lower conductivity
- Water management difficult
- High ambient temperature (60℃) can cause failure of the membrane and hence increases in conductivity destroys FC but not thought to create a hazard
- Intolerance to impure reactants

Reactions:

Anode:

$$2H_2 + 4OH^- \rightarrow 4H_2O + 4e^-$$

Cathode:

$$O_2 + 4e^- + 2H_2O \rightarrow 4OH^-$$

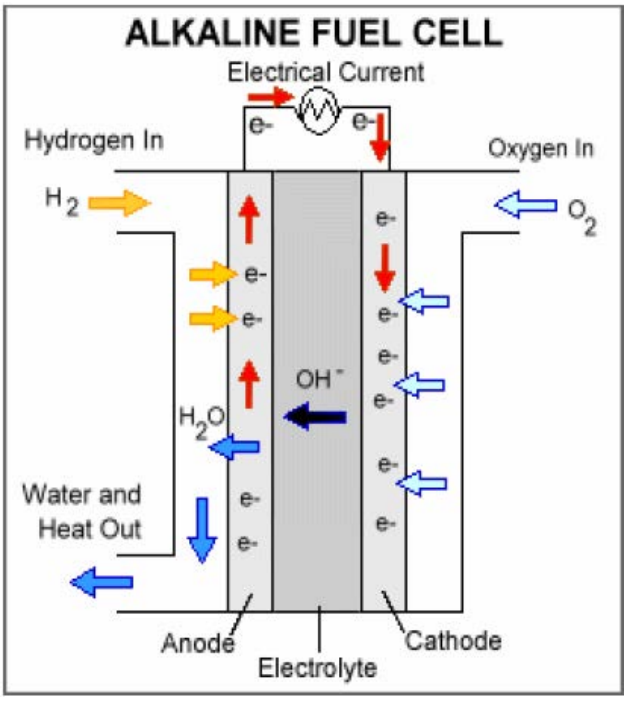

Figure 77: Schematic of an Alkaline fuel cell operation, [14]

Phosphoric Acid fuel cell (PAFC)

Having an operating temperature range of $150℃ - 200℃$ and using a relatively stable (when compared with other acids) electrolyte of phosphoric acid, H_3PO_4, the PAFC is only able to obtain a moderate current density when compared with the other two low temperature fuel cells (AFC and PEM). The PAFC share the AFC's intolerance to carbon monoxide, CO, poisoning, yet are tolerant regarding carbon dioxide, CO_2.

Pros

- Tolerant regarding CO_2
- Facilitated water management

Cons

- Moderate current density
- Intolerance to CO

Reactions:

Anode:

$$H_2 \rightarrow 2H^+ + 2e^-$$

Cathode:

$$1/2O_2 + 2H^+ + 2e^- \rightarrow H_2O$$

Direct Methanol fuel cell (DMFC)

Being a sub-category of the proton exchange membrane (PEM) fuel cells, their main advantage lies within the used fuel: methanol. It's not only relatively inexpensive, easily transportable and fairly energy-dense, but also a reasonable stable liquid in all environmental conditions.

Further disadvantages related with the usage of this type of fuel cell are the requirements of expensive catalysts (Platinum and Ruthenium), as well as the provision of water, which in the last case will affect negatively the energy density of the fuel. Table 52 contains the evolution of DMFC regarding Power and Energy Density for different models since 2003.

Table 52: SFC DMFC Development

Year	Power [W]	Energy density [Wh/kg]	Time [hr]	Model
2003/4	20	426	100	2003/4_C25
2004	20	422	500	2004_C20
2005	20	620	300	2005_FCPS
2007	25	629	300	2007_JENNY
2008	25	578	500	2007_JENNY_600s
2009	20	560	150	2009_M25

Pros

- Technical maturity
- High energy density
- Fuel and Fuel Handling
    - Easy handling and distribution
    - Replaceable tanks (cartridges)
- Fast start-up (<1 minute)
- Commercially available
- Easy to carry and handle
- Simple to use

Cons

- Toxic fuel
- Higher catalyst loading will lead to higher MEA costs. This may limit the opportunity for cost reduction compared to other fuel cell technologies
- Limited power density
- Higher moisture content of the exhaust system
- Non-logistic fuel

Reactions:

Anode:

$$CH_3OH + H_2O \rightarrow 6H^+ + 6e^- + CO_2$$

Cathode:

$$3/2O_2 + 6H^+ + 6e^- \rightarrow 3H_2O$$

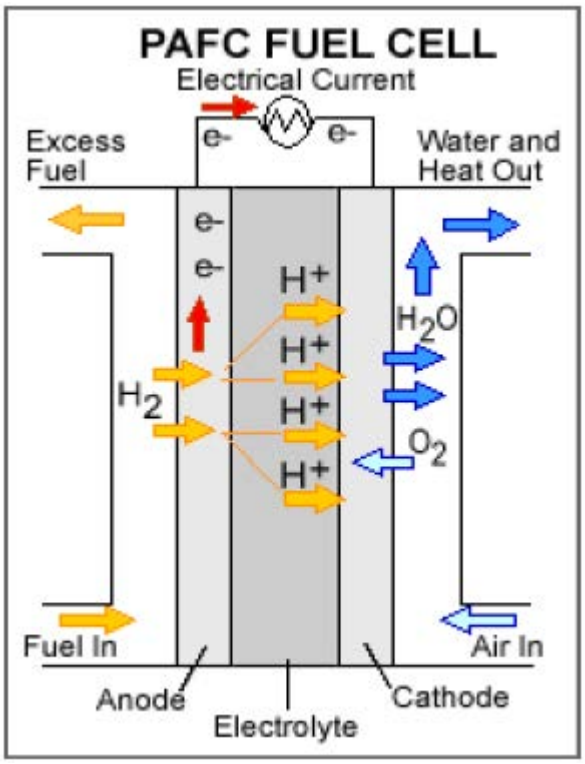

Figure 78: Schematic of PAFC operation, [14]

High Temperature fuel cell

Molten Carbonate fuel cell (MCFC)

As previously mentioned, MCFC are high-temperature fuel cells and their operating temperature range is $600℃ - 700℃$. The electrolyte used is a compound of molten carbonate salt mixture, suspended in a porous, chemically inert ceramic matrix of beta-alumina solid electrolyte (BASE). As a result of the high operating temperatures, non-precious metals can be used as catalysers for this type of fuel cell, leading to significant cost reduction.

Compared with PAFC, MCFC offer significantly higher efficiencies, especially when Combined Heat and Power (CHP) is used. To be more precise, MCFCs can reach efficiencies of near 60%, and as high as 85% when waste heat is captured and used, while PAFC don't overcome 42%.

Pros

- Inexpensive catalysers can be used
- Ability for CHP use
- High efficiencies (especially when CHP is used)

Cons

- High operating temperatures require resistant constructing material

Reactions:

Anode:

$$H_2 + CO_3^{2-} \rightarrow H_2O + CO_2 + 2e^-$$
$$CO + CO_3^{2-} \rightarrow 2CO_2 + 2e^-$$

Cathode:

$$1/2O_2 + CO_2 + 2e^- \rightarrow CO_3^{2-}$$

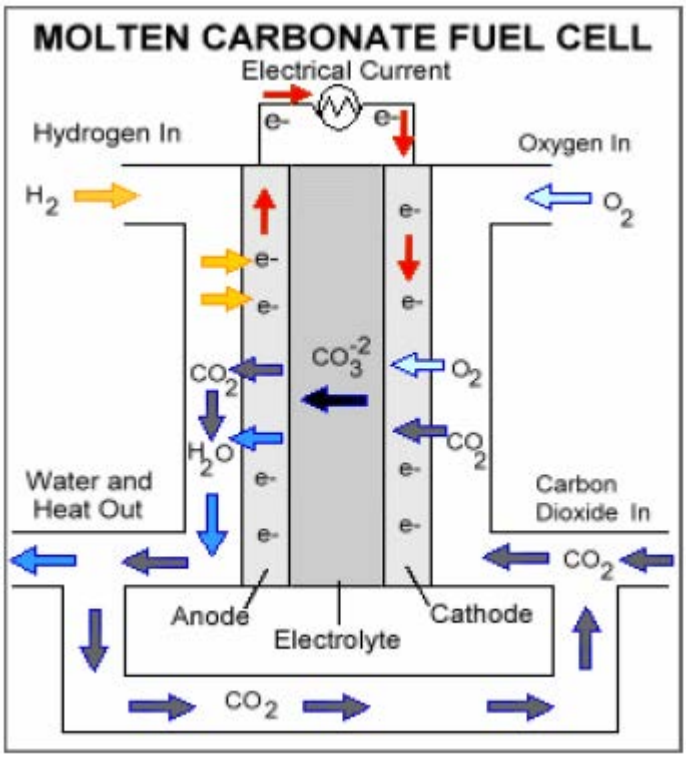

Figure 79: Schematic of MCFC operation, [14]

Solid Oxide fuel cell (SOFC)

Like the MCFC, the SOFC is a high-temperature fuel cell with a solid oxide or metal oxide ceramic electrolyte, often zirconia and yittria. The catalyst is a non-noble metal that is impregnated to the porous cermet electrolyte. The particularity of the electrolyte material is that it only becomes electrically and ionically active when subjected to high temperatures ranging from 500℃ to 1000℃. While having the advantage of not requiring expensive catalysts thanks to the high operating temperature, that same operating condition leads to longer start-up and shut-down times.

Not only are SOFC not contaminated by carbon monoxide, CO, but they actually can directly oxidize it at the anode. Even if the hydrogen oxidation reaction still predominates, that particularity means they can run on "dirty" reformate and that CO clean up in a fuel processor is not required. However, sulphur poisoning has been widely observed leading to the use of adsorbent beds or other means to remove the sulphur before entering the cell.

Another advantage created by the high operating temperatures is that it is possible to consider this FC in autothermal reforming, having the possibility to pack the fuel processor along with the stack leading to improvement in the cell's power output per unit mass (specific power).

Table 53: AMI Portable SOFC DevelopmentTable 53contains the evolution of Power and Energy density for SOFC since 2002.

Table 53: AMI Portable SOFC Development

Year	Power [W]	Energy density [Wh/kg]	Time [hr]
2002	20	375	50
2004	20	850	50
2006	25	550	300
2010	60	825	1000

Pros

- Easy to carry and handle
- Can be direct fuelled by utilizing commercially available gas (propane) provided additional filtering is used. Specific pure fuel systems are available
- Simple to use
- Potentially wider operating temperature

Cons

- Availability of rare earth materials for catalyst and electrolyte (reliant upon China)
- Cost of these materials add to the cost of the fuel cell
- Long start up and shut down times (30 minutes)
- Number of stop start cycles may be limited
- Robustness of construction may be an issue as the design relies upon ceramic materials.

Reactions:

Anode:

$$H_2 + O^{2-} \rightarrow H_2O + 2e^-$$

$$CO + O^{2-} \rightarrow CO_2 + 2e^-$$

$$CH_4 + 4O^{2-} \rightarrow 2H_2O + CO_2 + 8e^-$$

Cathode:

$$1/2O_2 + 2e^- \rightarrow O^{2-}$$

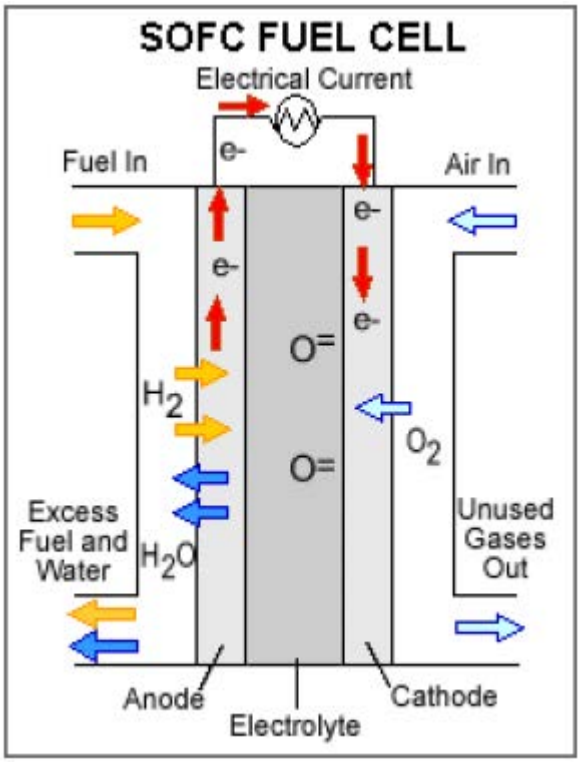

Figure 80: Schematic of a SOFC operation, [14]

5. Composite materials

5.1 Manufacturing Processes

There are several manufacturing processes available for composite components manufacture. A general comparison will be made, discussing their limitations, advantages, types of raw materials used, and mentioning the different criteria for process selection: rate, cost, strength, and size and shape requirements of the part. Manufacturing Processes of Composite Materials are usually divided in Thermoset and Thermoplastic. Typical applications of each process will be shortly addressed as well.

Table 54: Manufacturing Process selection criteria, [30]

Process		**Production Speed**	**Cost**	**Strength**	**Size**	**Shape**	**Raw Material**
Filament Winding		Slow to fast	Low to High	High	Small to large	Cylindrical and axisymetric	Continuous fibres with epoxy and polyester resins
In Pultrusion		Fast	Low to medium	High (along longitudinal direction)	No restriction on length; small to medium size cross-section	Constant cross-section	Continuous fibres, usually with polyester and vinylester resins
Hand-lay up		Slow	High	High	Small to large	Simple to complex	Prepreg and fabric with epoxy resin
	Wet lay-up	Slow	Medium	Medium to high	Medium to large	Simple to complex	Fabric/mat with polyester and epoxy resin
	Spray-up	Medium to fast	Low	Low	Small to medium	Simple to complex	Short fibre with catalyzed resin
RTM		Medium	Low to medium	Medium	Small to medium	Simple to complex	Preform and fabric with vinylester and epoxy
SRIM		Fast	Low	Medium	Small to medium	Simple to complex	Fabric or preform with polyisocyanurate resin
Compression Moulding		Fast	Low	Medium	Small to medium	Simple to complex	Moulded compound (e.g., SMC, BMC)
Stamping		Fast	Medium	Medium	Medium	Simple to contoured	Fabric impregnated with thermoplastic (tape)

Injection moulding	Fast	Low	Low to medium	Small	Complex	Pallets (shot fibre with thermoplastic)
Roll Wrapping	Medium to fast	Low to medium	High	Small to medium	Tubular	Prepreg

Wet lay-up Process

Wet lay-up consists of a simple, labour intensive, flexile, and low cost process. The process comprises the placement of each layer of resin and fibre onto the mould, followed by the use of a roller to impregnate the fibre with resin. This process repeats itself for the number of layers intended. Due to its simplicity, and little capital investment, this process is widely used in the making of prototype parts.

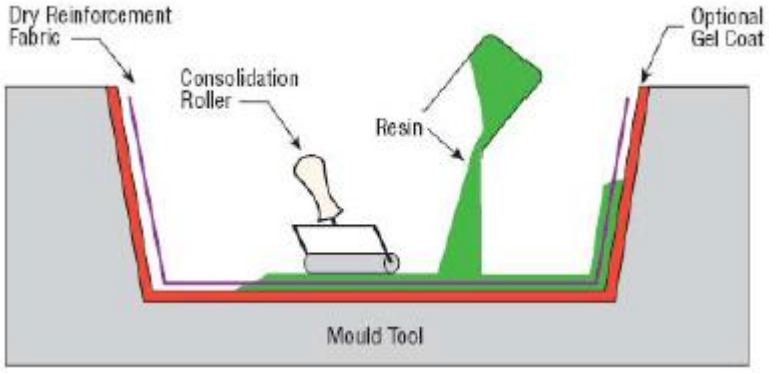

Figure 81: Wet lay-up Process, [30]

Spray-up Process

A similar process to hand lay-up, since reinforcement material and resin are applied manually onto the mould, resulting in a labour intensive process. Here, however, reinforcement and resin are applied continuously through a spray gun, resulting in a faster process than hand lay-up. This process is used in applications where the product's strength is not crucial.

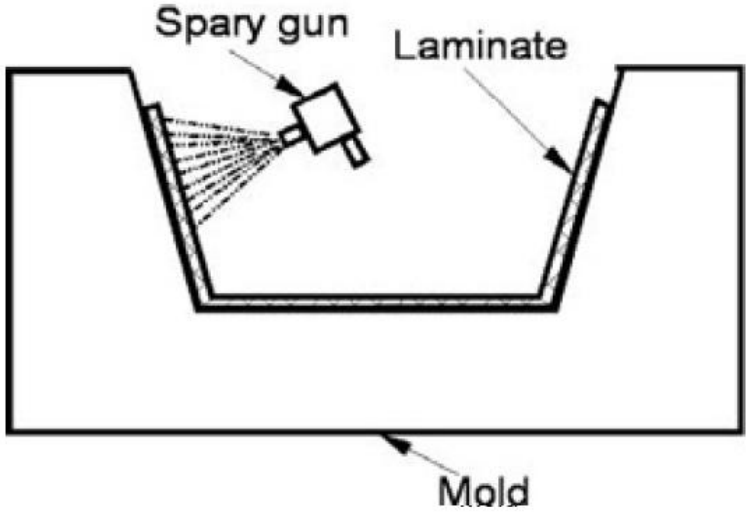

Figure 82: Schematic of the spray-up process, [30]

Filament Winding Process

Continuous process that can be automated for making high-volume parts in a cost-effective manner, especially suitable for the manufacture of tubular parts, or specialized structures such as pressure vessels. The process consists in wounding the resin-impregnated fibres back and forth through a carriage unit over a rotating mandrel at a desired angle, rotating mandrel velocity, and carriage unit translation velocity.

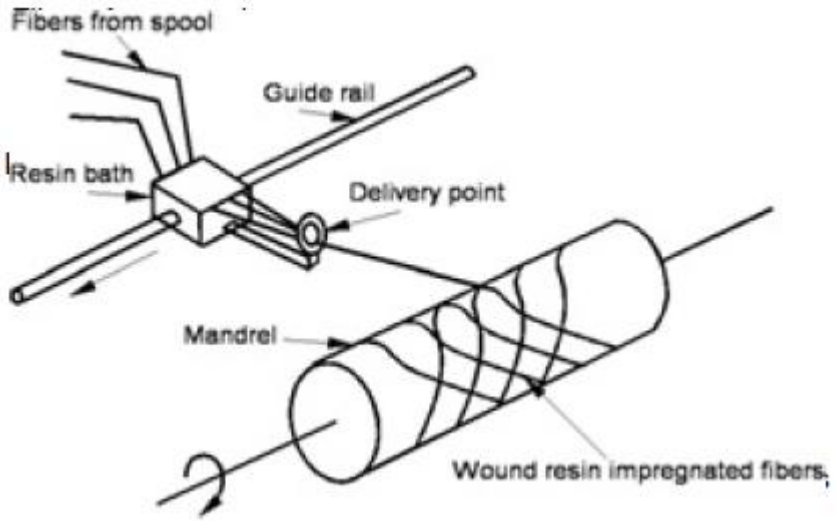

Figure 83: Schematic of the filament-winding process, [30]

Pultrusion Process

Pultrusion is continuous, low-cost, high-volume manufacturing process comprising a system where the fibres are pulled through a resin bath onto a heated metal die cavity of the desired cross section and shape, serving as a mould and a curing oven at the same time. In fact, the higher the temperature of the die, the higher the speed of pulling. Pultrusion can be used to fabricate a wide range of solid and hollow structures with constant cross sections.

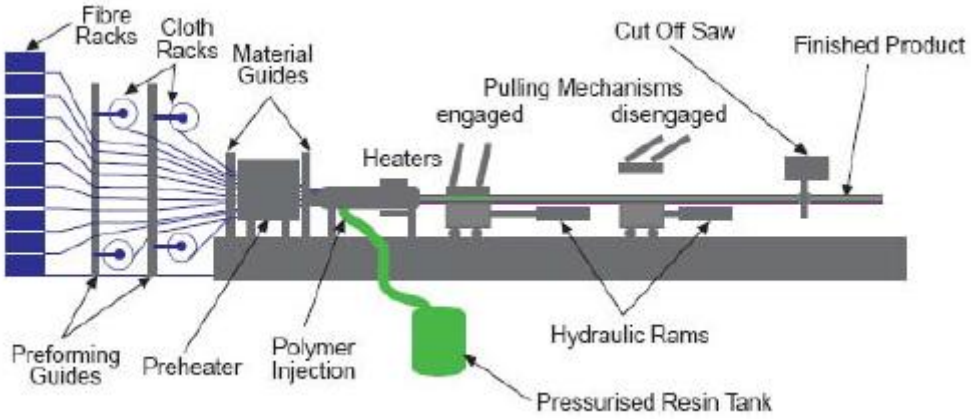

Figure 84: Pultrusion, [30]

Resin Transfer Moulding Process

This process comprises placing a preform into a mould cavity, followed by mating a matching mould half to the first and clamping both together. A pressurized mixture of thermoset resin is

pumped into the mould. After the cure is complete, the part is removed from the mould, resulting in good surface finish structural parts.

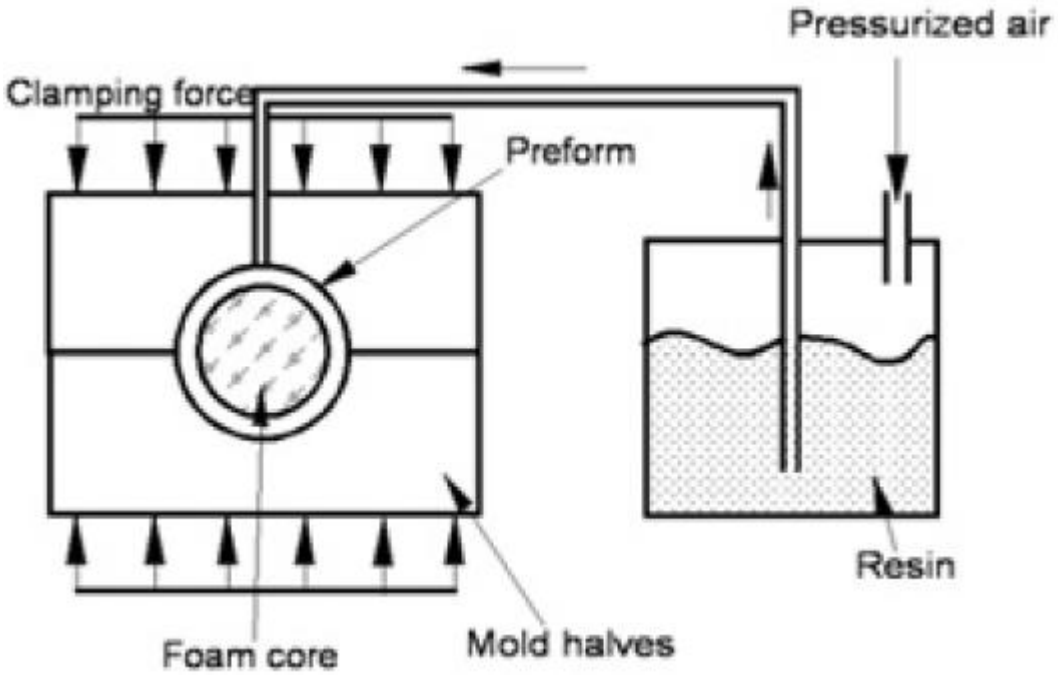

Figure 85: Schematics of the RTM process, [30]

Autoclave

A capital intensive process where whole composite or metal mould is sealed in a vacuum bag, after being treated with multiple release agent and loaded with layers of prepreg. The bag is then placed in an airtight heating chamber, or autoclave. The autoclave's doors are then shut, heat is applied and air withdrawn from the air, making air and excess resin to be expelled of the component. This composite cure equipment results in excellent quality (little defect and high fibre volume). Autoclave products are use in applications where quality and performance are of the upmost importance, such as aerospace, military and Formula 1.

6. UAV/UAS review

6.1 Top Performers

The following tables regarding top current performers were constructed from the data available from UVS international.

Endurance

UAS	Endurance (h)	MTOW (kg)
• General Atomics (US) Predator and Gnat families • IAI-Malat (Israel-IL) Heron	40	500 to 5000
• AAI (US) Aerosonde	24	15
• Elbit (IL) Hermes 450	20	450
• Insity (US) NightEagle and ScanEagle • IAI-Malat (IL) Searcher and Hunter • AAI (US) Shadow 600 • Aeronautics (IL) Aerostar • Selex Galileo (Italy - IT) Falco	12+	100 to 200

Range

UAS	Range (km)	MTOW (kg)
• General Atomics (US) Altus	5500	975
• General Atomics (US) Predator	3700	1000
• General Atomics (US) GNAT family • AAI (US) Aerosonde	2800	15 to 1000
• IAI-Malat (IL) Heron	1000	1100
• IAI-Malat (IL) Harpy	500	135

Maximum Speed

UAS	Maximum Speed (km/h)	MTOW (kg)
• General Atomics (US) Altair	400	3250
• General Atomics (US) GNAT 750	260	500
• IAI-Malat (IL) Harpy	250	135
• Sagem (France-FR) Sperwer • RUAG (Switzerland-CH) Ranger	240	280 to 350
• IAI-Malat (IL) Heron • General Atomics (US) I.GNAT • IAI-Malat (IL) Searcher II • AAI (US) Shadow 200	230	150 to 1100

Maximum Payload

UAS	Maximum Payload (kg)	MTOW (kg)
• General Atomics (US) Altair	300	3250
• IAI-Malat (IL) Heron	250	1100
• General Atomics (US) Predator • General Atomics (US) I.GNAT ER	200	1000
• Elbit (IL) Hermes 450 • General Atomics (US) Altus	150	450 to 975
• IAI-Malat (IL) Hunter	115	725
• IAI-Malat (IL) Searcher II	100	425
• General Atomics (US) I.GNAT	90	700

Significant to civilian UAV evolution is its military counterpart, since military gained experience and activities, such as maritime patrol or security for major events, are compatible and share advantages with some civilian applications. Therefore, military acquired knowledge can effectively contribute in features such as persistence, cost effectiveness and the ability to function in an environment hazardous to human occupants, [34].

Cultural and social issues have been a limiting factor in military UAVs, and they might be even more limiting when discussing civilian UAVs. Legislation and regulation have also posed as serious development constrains, and therefore require great progress. These issues are further discussed in Section 8.6.

Table 55: Applications by segment

Market segment		Application

Government	Civil-protection - Security	• Law enforcement, namely in urban scenarios:
		  o Urban patrolling
		  o Event security
		  o Crowd monitoring
		  o Support to operations (urban guerrilla, hostage rescue, sting or rapid intervention operations)
		• Harbour protection
		• Border security (including coastal patrol)
		• Maritime patrol (including protection of shipping routes)
		• Monitoring of critical infrastructures

	Civil-protection - non-Security	• Fire fighting • Disaster/Crisis management/Situational Awareness • Emergency rescue (support to SAR operations)

		• Land and Sea traffic monitoring • Nuclear Biological Chemical (NBC) detection
Commercial	Communications	• Communications relay • Ad hoc communications and broadcasting networks
	Environmental	• Climate monitoring • Weather monitoring • Pollution monitoring • Atmospheric research • Marine research • Land research
	Management of natural resources	• Forest inventory • Wildlife management • Monitoring of other resources
	Agriculture, Forestry and Fisheries	• Soil characterization • Crop dusting • Optimizing use of resources
	Energy	• Dam integrity assessment • Power line and pipeline inspection • Monitoring and protection of oil and electricity distribution infrastructures
	Other applications	• Infrastructure and equipment monitoring • Aerial photography and cartography • Special effects • Advertising • Private security • Satellite augmentation systems
	Transportation	• Cargo transportation • Passenger transportation

6.2 Product tree

A UAS can be decomposed in a few major systems:

- UAV
- Payload
- Communications
- Ground Control Station
- Launch and Recovery Equipment

- Training and Simulation systems
- Logistics support systems

Chart 4 describes the resulting subsystems.

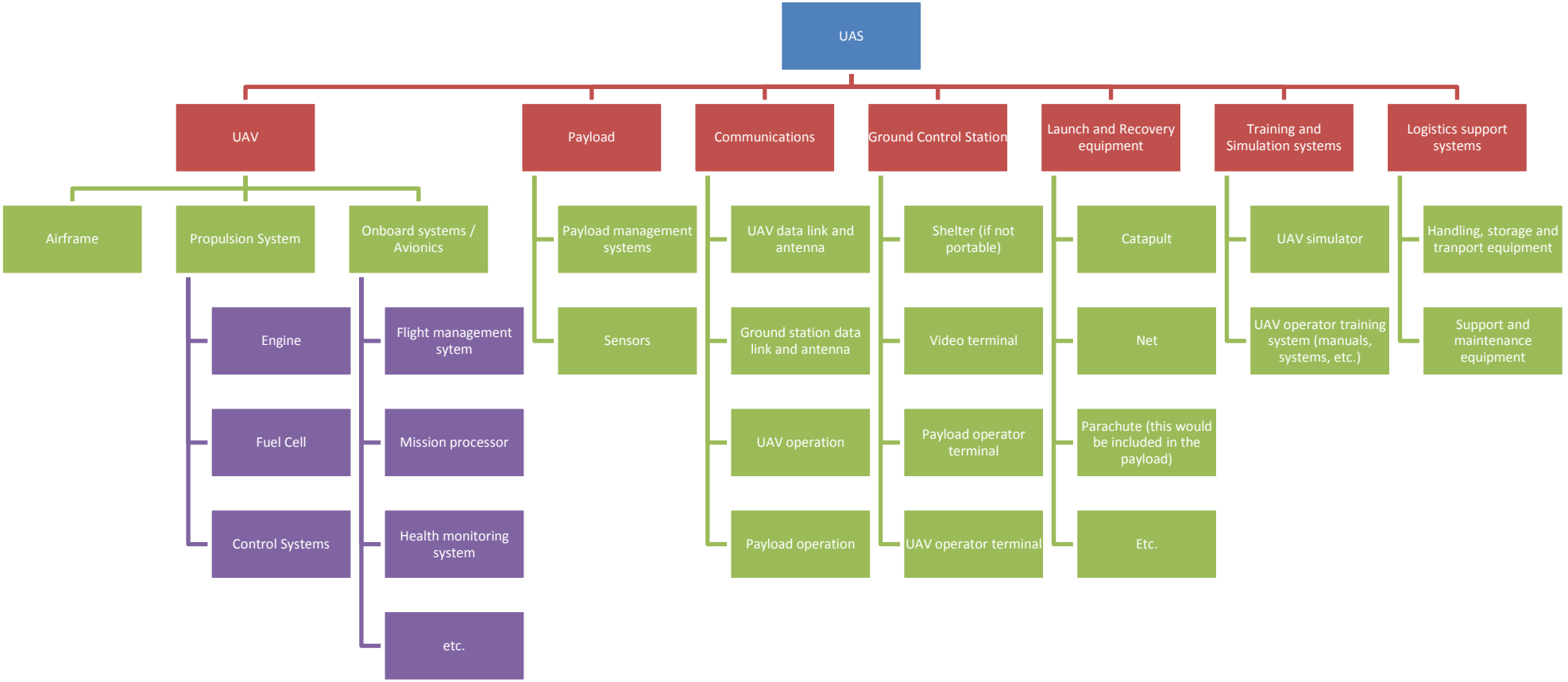

Chart 3: UAS Product Tree

6.3 Future Standards, Regulation and Procedure Requirements

When considering the implementation of UAS in regions of the world with considerable traffic density, the need for ensuring traffic and population safety thorough UAS regulation arises. Safety is the single, most important consideration that dominates the work on integration of UAS into controlled airspace, [34].

<table>
<tr><td colspan="2">Safety</td></tr>
<tr><td>Reliability
Military: Complete mission
Civilian: Complete mission without threat to life and property
Powerplant
Airframe
Avionics, navigation, communications (including GCS)
Crew training
Payload</td><td>Security
Secure Command, Control and Communications (C3) and datalinks (UAS equivalent to locked cockpit)
No physical danger to public (e.g. from impact, accidental or deliberate)
Legitimacy of purpose (denial of access for criminal or terrorist use)</td></tr>
</table>

6.4 Regulation

Regarding regulation, two aspects must be considered: aircraft's airworthiness and its operation. Airworthiness, the aircraft's suitability for safe flight, is related with the aircraft's development and production processes, performance and operational envelope. The operation certification, besides being impacted by the airworthiness' characteristics, is also related with the pilots, insurances, communications, integration with manned aircraft, as well all other implications that arise from sharing airspace with manned and other unmanned platforms.

Considering European airspace, the entity responsible for regulation and aviation safety, and to which all EU national civil aviation authorities in the EU is the European Aviation Safety Agency (EASA).

According to EASA, "it is first necessary to demonstrate that the "machine" can safely move in the air, in controllable conditions (i.e. airworthiness) and without unduly endangering over-flown population." For "determining the acceptable level of airworthiness", EASA is using "the principle of safety equivalence with manned aircraft as a driving factor".

EASA's development of Implementing Rules for the operation of UAS (air operations, licensing, and maintenance) is currently predicted to occur from 2013-2016. EASA, however, leaves the responsibility of certification of aircrafts with MTOWs below 150kg to national civil authorities. The Italian Selex Galileo's Falco was the first UAS in Europe to obtain a civil permit to fly in June 2005. The Portuguese Civil Aviation Authority, the Instituto Nacional de Aviação Civil (INAC), has shown no sign of interest in developping a certification for small UAS ahead of EASA.

Given the current difficulties in obtaining a flying certification for a civilian UAV, some alternatives are suggested:

- Certification by a military aviation authority
- Certification by a foreign civil aviation authority
- Avoid or simplify certification

- Use a certified UAV (airframe)

TECHNICAL DATA SHEET
No. CFA-014

TORAYCA®

M40J DATA SHEET

MJ type high modulus fiber with enhanced tensile and compressive strength over *M* series fibers. Mainly used for premium sporting goods, aerospace, and industrial applications.

FIBER PROPERTIES

		English	Metric	Test Method
Tensile Strength		640 ksi	4,410 MPa	TY-030B-01
Tensile Modulus		54.7 Msi	377 GPa	TY-030B-01
Strain		1.2 %	1.2 %	TY-030B-01
Density		0.064 lbs/in^3	1.77 g/cm^3	TY-030B-02
Filament Diameter		2.0E-04 in.	5 µm	
Yield	3K	13,181 ft/lbs	113 g/1000m	TY-030B-03
	6K	6,620 ft/lbs	225 g/1000m	TY-030B-03
	12K	3,310 ft/lbs	450 g/1000m	TY-030B-03
Sizing Type & Amount	50A, 50B	1.0 %		TY-030B-05
Twist		Twisted, Untwisted		

FUNCTIONAL PROPERTIES

CTE	-0.83 $\alpha \cdot 10^{-6}$/˚C
Specific Heat	0.17 Cal/g·˚C
Thermal Conductivity	0.164 Cal/cm·s·˚C
Electric Resistivity	1.0 x 10^{-3} Ω·cm
Chemical Composition: Carbon	>99 %
Na + K	<50 ppm

COMPOSITE PROPERTIES*

Tensile Strength	360 ksi	2,450 MPa	ASTM D-3039
Tensile Modulus	33.5 Msi	230 GPa	ASTM D-3039
Tensile Strain	1.1 %	1.1 %	ASTM D-3039
Compressive Strength	185 ksi	1,270 MPa	ASTM D-695
Flexural Strength	220 ksi	1,520 MPa	ASTM D-790
Flexural Modulus	28.5 Msi	195 GPa	ASTM D-790
ILSS	13.0 ksi	9 kgf/mm^2	ASTM D-2344
90˚ Tensile Strength	7.5 ksi	53 MPa	ASTM D-3039

* Toray 250˚F Epoxy Resin. Normalized to 60% fiber volume.

PROTON MOTOR
Proton Power Systems plc Group

more than just fuel cells

PM 200
Hydrogen Fuel Cell

The certified PM 200 Stack is designed for industrial applications and can be used in maritime, stationary and mobile applications.
Nominal electrical power output range from 2.0 kW to 8.0 kW dependent on number of cells.
The PM 200 stack is a proprietary development of Proton Motor and is used in all our systems and products.
Further configurations of the stack are available on demand.

Features and Benefits:

- ***Environmental***
  - No emissions
  - High efficiency
- ***Maintainability***
  - Cell voltage monitoring possible
  - Easy maintenance
  - Long lifetime
- ***Flexibility***
  - Easy system integration of OEM specific applications
  - Costumer specific adaptations possible
  - Multi stack operation possible
  - No external humidification needed
- ***Reliability & Safety***
  - TÜV certified based on:
  - VDE 0130-201 und DIN EN / IEC 62282-2

Proton Motor Fuel Cell GmbH
Benzstraße 7
D-82178 Puchheim
Germany

Phone +49 (0) 89 1276265 – 11
Fax +49 (0) 89 1276265 – 99
Email sales@proton-motor.de
Website www.proton-motor.de

PROTON MOTOR
Proton Power Systems plc Group

more than just fuel cells

Type	LT-PEM Fuel Cell (Low Temperature Polymer Electrolyte Membrane)		
Cells	24	48	96
Power (Rated/Peak)	2.0/2.2 kW	4.0/4.4 kW	8.0/8.8 kW
Current (Rated/Peak)	130/150 A		
DC Voltage	14…28 V	27…55 V	53…110 V
Efficiency	> 52 %		
Hydrogen quality	ISO 14687-2 / SAE J2719		
Operating pressure H_2	400…600 $mbar_g$		
Pressure process air*	600 $mbar_g$		
Coolant	DI-water/ glycol		
Storage temperature	-20°C…+50°C		
Start up temperature	>0°C		
Max. stack temperature	Up to +65°C		
Width x height x length (Overall Dimensions)	246 x 136 x 155 mm	246 x 136 x 247 mm	246 x 136 x 432 mm
Mass	6.5 kg	9.2 kg	14.6 kg
Operating Lifetime	Up to 5000 h		

* Operation at lowered pressure possible with decreased efficiency

Further configurations available on demand

Note: Specifications are subject to change without notifications

Please contact us for product availability and pricing

more than just fuel cells

Proton Motor Fuel Cell GmbH
Benzstraße 7
D-82178 Puchheim
Germany

Phone +49 (0) 89 1276265 – 11
Fax +49 (0) 89 1276265 – 99
Email sales@proton-motor.de
Website www.proton-motor.de

M40J

COMPOSITE PROPERTIES**

Tensile Strength	330 ksi	2,250 MPa	ASTM D-3039
Tensile Modulus	31.5 Msi	215 GPa	ASTM D-3039
Tensile Strain	1.0 %	1.0 %	ASTM D-3039
Compressive Strength	155 ksi	1,080 MPa	ASTM D-695
Compressive Modulus	30.0 Msi	205 GPa	ASTM D-695
In-Plane Shear Strength	8.5 ksi	59 MPa	ASTM D-3518
ILSS	13.0 ksi	9 kgf/mm^2	ASTM D-2344
90˚ Tensile Strength	7.0 ksi	50 MPa	ASTM D-3039

** Toray Semi-Toughened 350˚F Epoxy Resin. Normalized to 60% fiber volume.

See Section 4 for Safety & Handling information. The above properties do not constitute any warranty or guarantee of values. These values are for material selection purposes only. For applications requiring guaranteed values, contact our sales and technical team to establish a material specification document.

PACKAGING

The table below summarizes the tow sizes, twists, sizing types, and packaging available for standard material. Other bobbin sizes may be available on a limited basis.

Tow Sizes	Twist[1]	Sizing	Bobbin Net Weight (kg)	Bobbin Type[2]	Bobbin Size (mm) a	b	c	d	e	Spools per Case	Case Net Weight (kg)
3K	B	50B	0.5	II	76	82	192	107	156	20	10
6K	A	50A	1.0	II	76	82	192	126	156	16	16
	B	50B	1.0	II	76	82	192	126	156	16	16
12K	A	50A	2.0	II	76	82	192	157	156	12	24
	B	50B	2.0	II	76	82	192	157	156	12	24

1 **Twist** A: Twisted yarn B: Untwisted yarn made from a twisted yarn through an untwisting process C: Never twisted yarn

2 **Bobbin Type** See Diagram below

TYPE I

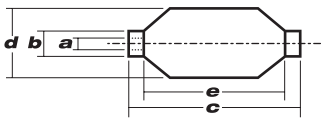

TYPE II

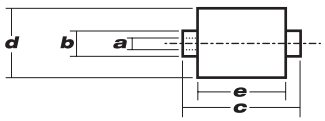

TYPE III

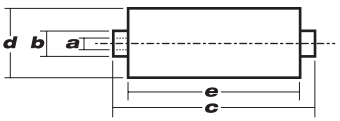

TORAY CARBON FIBERS AMERICA, INC.
6 Hutton Centre Drive, Suite #1270, Santa Ana, CA 92707 TEL: (714) 431-2320 FAX: (714) 424-0750
Sales@Toraycfa.com Technical@Toraycfa.com www.torayusa.com

Horizon
Fuel Cell Technologies

5000W Fuel Cell Stack
User Manual

Updated 24 Jun. 2013

Model No.: FCS-C5000

Manual_FCS-C5000_V1.1_EN

Disclaimer

This manual incorporates safety guidelines and recommendations. However, it is not intended to cover all situations. It is the responsibility of the customer to meet all local safety requirements and to ensure safety during operation, maintenance and storage of the H-5000 stack.

Although all efforts have been made to ensure the accuracy and completeness of the information contained in this document, Horizon reserves the right to change the information at any time and assumes no liability for its accuracy.

Actions that will void the fuel cell and controller warranty:

- Attempt, under any circumstance, to disassemble or inappropriately tamper with the fuel cell.
- Operate the fuel cell with a controller not designed and built by Horizon for the specific fuel cell.
- Operate the fuel cell with valves and blowers, that are not provided by Horizon for the specified fuel cell and controller.
- Disassemble the fuel cell.
- Disassemble the controller.
- Operating the fuel cell and controller that is not in the setup and/or specified in the user manual provide for the specific product.
- Operate the fuel cell stack without the controller produced by Horizon or with the controller not produced by Horizon.

Do not attempt, under any circumstance, to disassemble or inappropriately tamper with the fuel cell. There will be no returns, refunds or exchanges should disassembly or tampering occur. If you have questions or need help with regards to the fuel cell and its technology contact: support@horizonfuelcell.com

IMPORTANT

In order for the warranty to come into effect the stack must be registered on the Horizon Warranty Page at: www.horizonfuelcell.com/warranty.htm

Table of Contents

1. Safety

Please read all instructions carefully prior to product use and keep this manual for future reference.

The safety guidelines included here may not cover every situation. Use common sense.

1.1 General information

For this unit to generate electrical power, a supply of hydrogen fuel is necessary. It is important for any operator to be aware of, understand, and follow all local safety requirements related to the handling of hydrogen and compressed gases. Ensure that your facility conforms to all local regulatory requirements, including building codes and recommendations.

The fuel cell system has built-in safeguards and is designed to shut down automatically if any out-of-range operating condition occurs. Possible situations include low cell voltage, high current, high temperature, low fuel pressure.

- Do not operate the stack on a grade of more than 65℃.
- Do not connect or disconnect power cables when the fuel cell stack is energised.
- Do not dismantle the system. Contact Horizon if you have any concerns about operation.

1.2 Using Hydrogen

WARNING! FIRE OR EXPLOSION

Keep all sources of ignition away from hydrogen.

This unit uses hydrogen fuel. Hydrogen is a colourless, odourless and flammable substance. It is highly combustible in the presence of oxygen and burns with a colourless flame.

Leaking gas may be hot and pose a burn danger. Stop the flow of gas – if you are not in danger – and use water to cool the area. If fire occurs, do not attempt to extinguish flames, allow the fire to burn out.

Prevent overexposure to hydrogen. Hydrogen is non-toxic but can act as a simple asphyxiant by displacing the oxygen in the air. There are no warnings before unconsciousness results. When operating the stack in an enclosure:

- Ensure ventilation slots are clear and unobstructed at all times during operation.
- Operate within the temperatures limits stated in the manual.
- Never operate if an alarm condition exists.

Note: We highly recommend customer use a hydrogen sensor(not provided) to detect the hydrogen leakage.

1.3 Handling Compressed Gas Cylinders

WARNING
Do not handle compressed hydrogen gas cylinders without training or experience.

• Use a pressure regulator to control the fuel inlet pressure to the system.
• Do not alter the fitting on a regulator. Ask experienced personnel for help.
• Do not attempt to force gas cylinder threads.
• Never transport a gas cylinder with regulators attached. Ensure cylinder caps are in place. Always use a cylinder cart with a safety strap or chain.
• Secure a high-pressure cylinder to a bench, post, or fixed object to avoid accidental contact.
• Avoid unnecessary contact with On/Off valves. They can easily move to “On” by accident.

1.4 Hydrogen Leakage

Hydrogen is colourless, odourless and tasteless. Hydrogen is non-toxic but can act as a simple asphyxiant by displacing the oxygen in the air. There are no warning symptoms before unconsciousness results.

WARNING
Inhaling hydrogen can lead to unconsciousness and asphyxiation. Hydrogen molecules are smaller than any other gas, making hydrogen more difficult to contain. It can diffuse through many materials considered airtight. Fuel lines, non-welded connections, and non-metal seals such as gaskets, O-rings, pipe thread compounds and packings present potential leakage or permeation sites. Furthermore, hydrogen’s small molecule size results in high buoyancy and diffusivity, so leaked hydrogen will rise and become diluted quickly.

Constant exposure to hydrogen causes hydrogen embrittlement in many materials. The mechanisms that cause hydrogen embrittlement effects are not well defined. Factors known to influence the rate and severity of hydrogen embrittlement include hydrogen concentration, hydrogen pressure, temperature, hydrogen purity, type of impurity, stress level, stress rate, metal composition, metal tensile strength, grain size, microstructure and heat treatment history. Moisture content in the hydrogen gas may lead to metal embrittlement through the acceleration of the formation of fatigue cracks. Hydrogen embrittlement can lead to leakage or catastrophic failures in metal and non-metallic components.

As a preventative measure, the stack must be operated in a well-ventilated area in order to inhibit potential hydrogen accumulation.

WARNING!

Always operate the stack in a well-ventilated area and ensure that ventilation slots are unobstructed.

1.5 Flammability and volatility

Hydrogen is flammable over concentrations of 4 – 75% by volume in air, and is explosive over concentrations of 15 – 59%. As a result, even small leaks of hydrogen have the potential to burn or explode. Leaked hydrogen can concentrate in an enclosed environment, thereby increasing the risk of combustion and explosion.

Hydrogen flames are pale blue and are almost invisible in daylight due to the absence of soot. Due to its high buoyancy and diffusivity, burning hydrogen rises unlike gasoline, which spreads laterally.

A flammable or explosive hydrogen mixture is easily ignited by a spark or even a hot surface. The auto-ignition temperature of hydrogen is 500 °C (932 °F). The energy of a hydrogen gas explosion is 2.4 times that of gasoline or methane for an equal volume. Hydrogen gas explosions are therefore more destructive and carry further.

WARNING!

A mixture of hydrogen and air is potentially flammable and explosive and can be ignited by a spark or a hot surface.

As in the presence of any fuel, all sources of ignition, including smoking, are not permitted in the vicinity of the stack.

WARNING!

Keep all sources of ignition away. Smoking is not permitted in the vicinity of the stack.

1.6 Oxygen Depletion

Oxygen is a colourless, odourless, non-toxic and tasteless gas. Oxygen is essential for life in appropriate concentrations.

Ambient air contains up to 21% oxygen. Oxygen levels below 19.5% are biologically inactive and may act as simple asphyxiants. Effects of oxygen deficiency may include: rapid breathing, diminished mental alertness, impaired muscular coordination, faulty judgement, depression of all sensations, emotional instability, and fatigue. As asphyxiation progresses, nausea, vomiting, prostration, and loss of consciousness may result, eventually leading to convulsions, coma, and death. At concentrations below 12%, immediate unconsciousness may occur with no prior warning symptoms.

WARNING!

Lack of oxygen can lead to unconsciousness and asphyxiation.

As a preventative measure, the stack must be operated in a well-ventilated area in order to compensate for the oxygen used within the fuel cells.

WARNING!

Always operate the stack in a well-ventilated area.

1.7 Electrical Safety

WARNING!

Avoid contact with an exposed fuel cell stack. Electrical shock can cause personal injury or death.

• Do not touch fuel cell plates or any electrical components at any time. A running fuel cell stack is a potential electrical hazard that can cause burns or electrical shock.
• Do not wear metallic jewellery – rings, bracelets, watchbands, or necklaces – when you are close to an exposed fuel cell stack.
• Minimise static discharge. If possible, ground all equipment.
• Minimise conductivity. Avoid contact with surfaces that are in contact with water or gases. Do not operate or store in wet or damp conditions.
• Never use damaged extension cords.

The stack generates up to 120 VDC (open circuit voltage). This voltage decreases as current is drawn from the stack. The stack produces 72V at maximum power. This voltage is exposed at the output power connections. These low voltages may constitute a shock hazard and can damage electronic components if shorted. Therefore, do not touch individual fuel cells, cell voltage monitoring equipment or electrical components.

WARNING!

Do not touch fuel cells, cell voltage monitoring equipment or electrical components. Electronic components can also be damaged as the result of static discharge. To minimise this, ground all equipment in contact with the stack. Never use damaged extension cords. Minimise conductivity by avoiding surfaces in contact with water; hands and clothes must be dry. Do not operate or store the stack in wet or damp conditions.

WARNING!

Minimise static discharge. Ground all equipment. Residual reactants within the stack can develop a charge in a matter of minutes when turned off. A reading of zero volts across the entire stack does not guarantee that all fuel cells are uncharged.

WARNING!

Always assume that the fuel cell stack is charged. Jewellery (such as rings, necklaces, bracelets and watches) may concentrate an electric current when it comes into contact with charged components, or when a shock passes through the human body. Accordingly, no jewellery should be worn near the stack.

WARNING!

Do not wear jewellery near the stack.
No pungent odor, paint and perfume are allowed around stack.

1.8 High Temperature

The fuel cell stack is designed to operate at 65ºC. At this operating temperature, the air exhaust stream temperature can reach 55ºC and the cooling air stream can reach 17ºC above ambient conditions. These temperatures are sufficient to cause burns or severe discomfort. Accordingly, avoid contact with the fuel cell stack, or components that convey process or cooling air.

WARNING!

Avoid contact with the fuel cell stack or components that convey process or cooling air.

2. Terminology

PEM fuel cell:
A PEM (Proton Exchange Membrane) fuel cell is a device that converts hydrogen and oxygen into water and electricity.

A fuel cell stack:
It includes a plurality of plate-like fuel cells arranged along an axis generally parallel to cell thickness with electrically conductive separator plates between each pair of cells.

Reactants:
Reactant is a material used to start a chemical reaction. In the fuel cell the reactants are air and hydrogen by which the electricity will be generated.

Humidification:
A process to humidify the proton exchange membranes for optimal performance.

Blower:
Fans attached to fuel cell stack to supply cooling air and process air.

Purging valve:
Excess water and hydrogen will be dispelled from the fuel cell flow channels via purge valve.

SCU:
Short circuit unit – the short circuit will be controlled for good performance of the stack.

Mass flow per minute:
The amount of hydrogen consumed to run the fuel cell at a certain power.

HFCT:
Horizon Fuel Cell Technologies

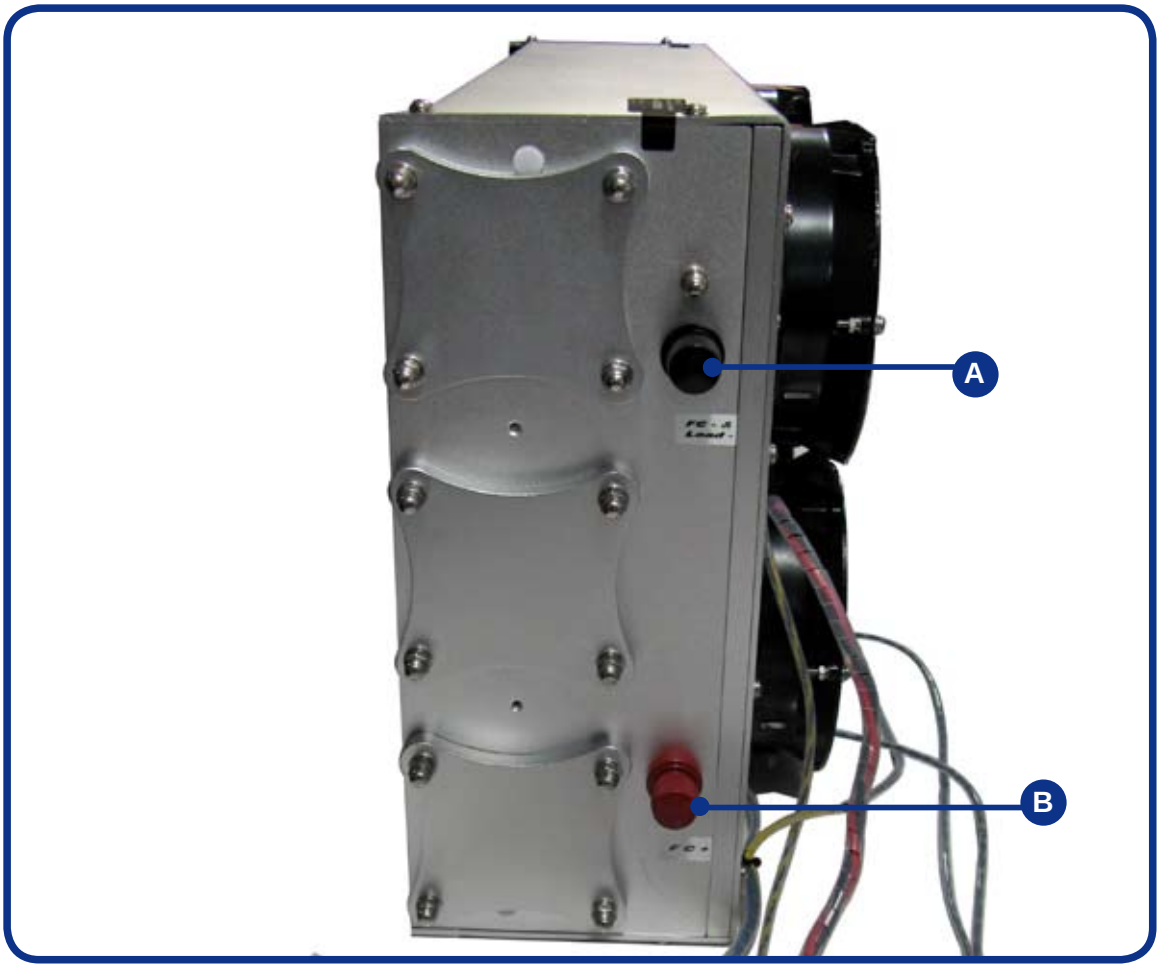

A: FC- and Load- connector

B: FC+ connector

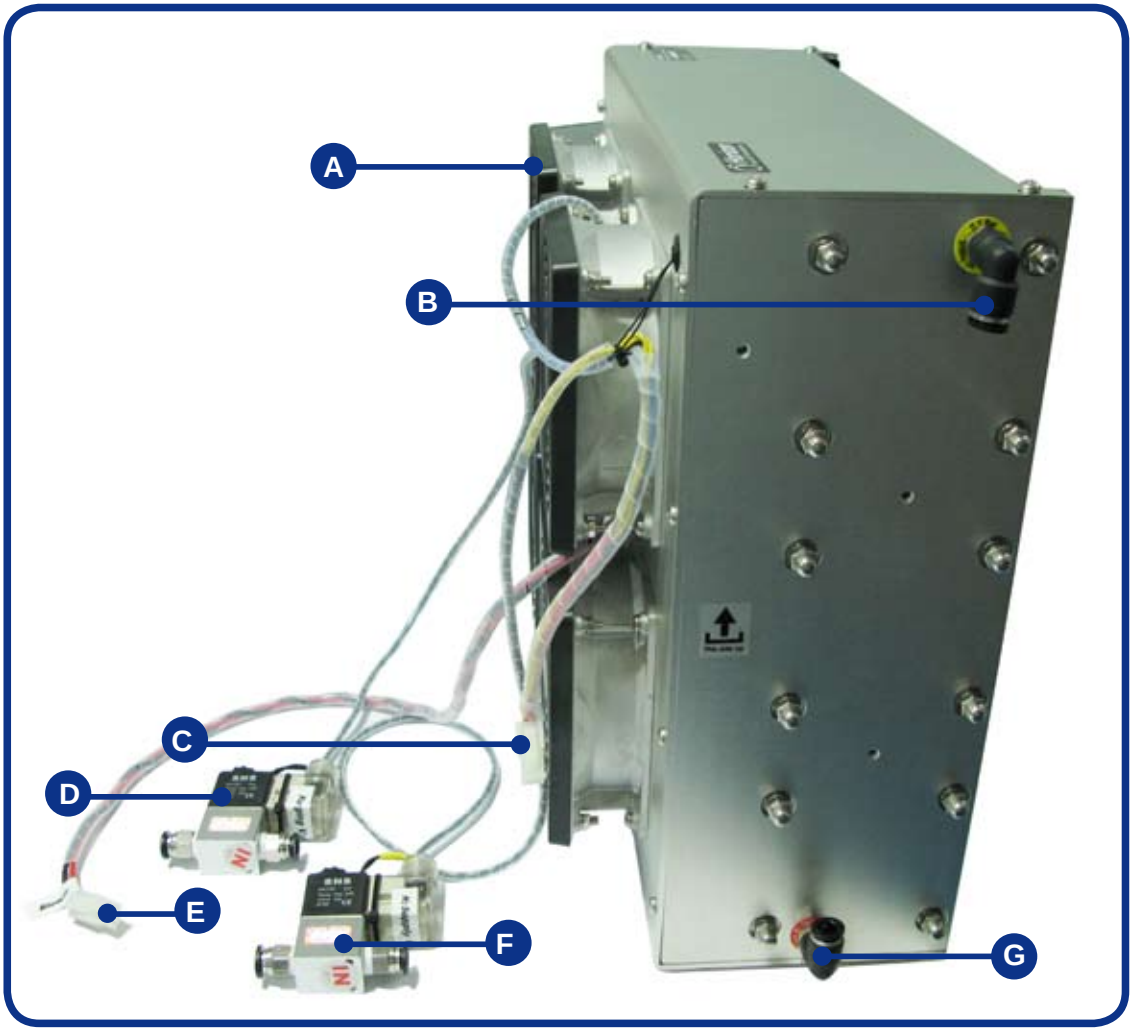

A: Blowers
B: Hydrogen Inlet connector
C: Fuel cell connect plug
D: Hydrogen supply valve
E: Blower connector
F: Hydrogen purge valve
G: Hydrogen outlet connector

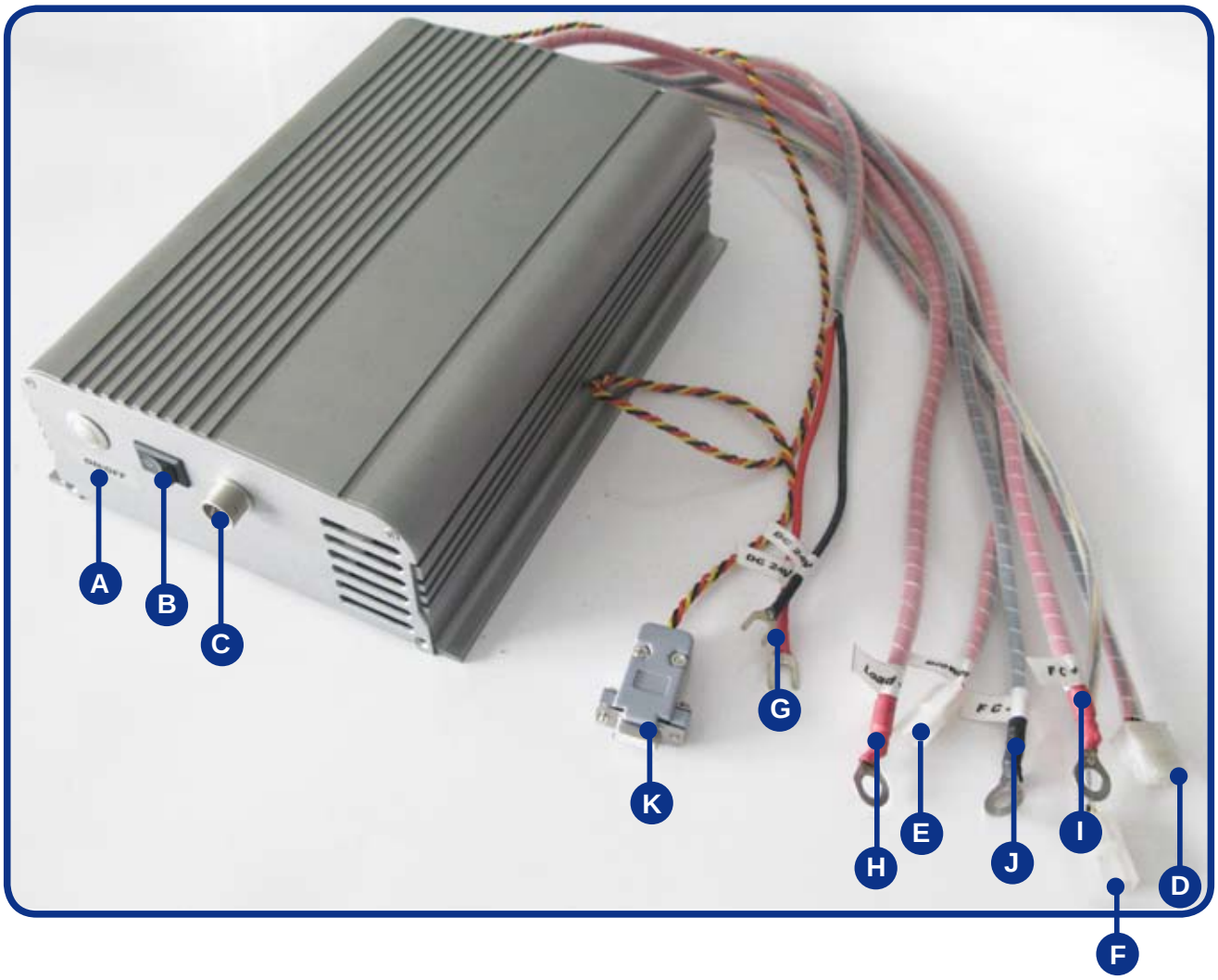

A: ON/OFF button

B: SCU(short circuit units) switch

C: LCD connector

D: Fuel cell connect plug

E: Blower power plug

F: Blower signal plug

G: Controller power supply DC 24V+ and DC 24v-

H: Connect to Load+

I: Connect to FC+

J: Connect to FC-

K: 232 connector

3. Stack and System Component Information

1. Stack

Is made up of plate-like cells with air channels to allow the flow of air across the membrane. The membrane facilitates the flow of Hydrogen creating the release of electrons. Electrically conductive separator plates between each pair of cells enable the flow of electrons. The stack aspect is that they are all placed on top of each other and held together by epoxy endplates.

2. H2 Supply and purging valves

The supply valve controls the H2 input. When the controller turns on, also the H2 supply valve does. When system turns off, it is in the off position for preventing hydrogen leakage.
The purging valve purges out the water and air gas redundant in the fuel cells.

3. Short Circuit Unit

The short circuit unit can be turned on or off depending on what application the stack is to be used in. When the short circuit unit turns on, it can enhance performance of the stack in applications where the stack is turned off for prolonged periods.

4. On/Off Switch

It is the switch of the controller. Hold it for 2 seconds for either on or off.

5. blowers

Supply air to the fuel cells and meanwhile decrease the temperature in the stack.

6. LCD

Show the Current and Voltage of the stack.

7. Controller

It controls the stack temperature, blowers, hydrogen input, purging and short circuiting of the stack.

8. Hydrogen Output

Hydrogen output: connect the tube shown in 11 below.

9. Hydrogen Input

Hydrogen input: connect the tube shown in 11 below with the hydrogen pressure between 0.45-0.55Bar.

10. Fuel cell +/Fuel cell-&Load- Connectors

FC+ of the controller is connected to the fuel cell positive pole.
FC- of the controller is connected to the fuel cell negative pole.

11. Tube for H2 Input and Output

The tube with 8mm outer diameter and 5mm inner diameter is connected to the H2 IN and the input valve of the hydrogen source and H2 OUTPUT to the output valve.

12. Grounding cable

Make stack grounded for safety (already connected on the stack).

13 . Fittings

For connecting the load.

4. Technical Specifications

Control electronics included:

Type of fuel cell	PEM
Number of cells	120
Rated Power	5000W
Performance	72V @ 70A
H2 Supply valve voltage	12V
Purging valve voltage	12V
Blower voltage	24V
Reactants	Hydrogen and Air
External temperature	5 to 30ºC
Max stack temperature	65ºC
H2 Pressure	0.45-0.55bar
Hydrogen purity	≧99.995％ dry H2
Humidification	self-humidified
Cooling	Air (integrated cooling fan)
Weight (with fan & casing)	30kg (±200g)
Controller	2.5kg (±100g)
Dimension	65cm x 35cm x 21.2cm
Flow rate at max output*	65 L/min
Start up time	≦30S at ambient temperature
Efficiency of stack	40% @ 72V
Low voltage shut down	60V
Over current shut down	90A
Over temperature shut down	65℃
External power supply**	24V(±1V), 8A~12A

**** The flow rate may change with the power output***
***** System electronics need external power supply***
****** The Specification is subject to change without notice.***

5. System Set-Up

⚠ *PLEASE READ CAREFULLY BEFORE STARTING*

WARNINGS:

1. The tube between the hydrogen pressure regulator and the fuel cell gas input is required to be less than 30cm. The inner diameter of the hydrogen supply tube is required to be more than 3mm. The input pressure to the stack is required to be 0.45-0.55Bar .
2. Disconnect the hydrogen tube from the hydrogen inlets immediately after the fuel cell stack is shut down. Since hydrogen gas can leak into the fuel cell and destroy the stack.
3. The stack must be standing on the clear plastic feet.
4. Make sure the dry Hydrogen gas to be used must be ≥99.995% purity.
5. Make sure you have purged the water out of the stack as much as possible if you injected water into the stack. Using the fuel cell stack with too much water inside can irreparably damage it!
6. Do not vibrate the stack when it is in operation.
7. Keep the stack in ventilation when it is in operation.
8. The external power voltage is required to be 24V(±1V).
9. Keep the SCU always on. Only when it causes your load operating in difficulty, turn off the SCU.
10. The tube between stack output and purging valve is required to be less than 20cm. The tube connected to the purging valve output is required to be less than 30cm. The inner diameter of the tube is required to be more than 3mm.

STEP 1:

Connect the connectors of the controller to the stack (1A), the temperature sensor, the hydrogen supply valve and the purge valve under control. The finished connection is shown in 1B.
Connect the stack blower power cable to the controller blower power cable (see picture 1C).
Connect the stack blower signal cable to the controller blower signal cable (see picture 1D & 1E).

1A

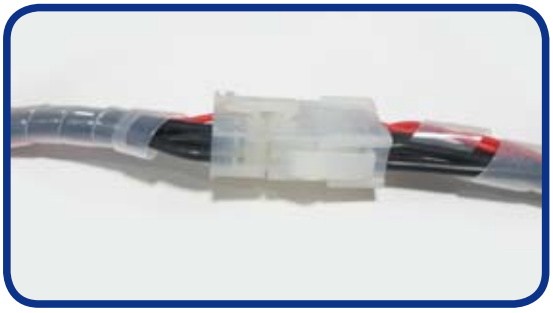

1B

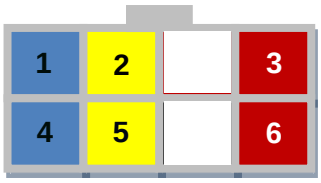

Controller connector

Wire colours	Connector pin #	Periferals controlled
Blue	#1 & #4	Hydrogen purge valve
Yellow	#2 & #5	Hydrogen supply valve
Red	#3 & #6	Temperature Sensor

1C

Blowers power connector

Wire colours	Connector pin #	Periferals controlled
Red	#7	Blowers power
Black	#8	

1D

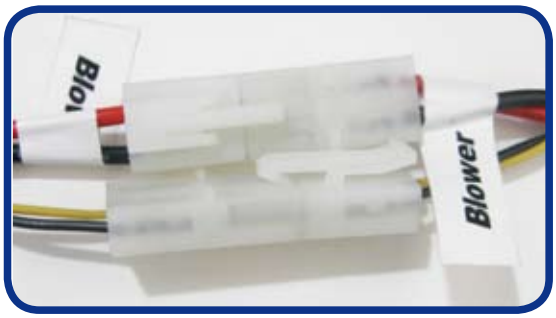

1E

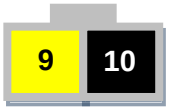

Blowers signal connector

Wire colours	Connector pin #	Periferals controlled
Yellow	#9	**Blowers signal**
Black	#10	

STEP 2:

Connect controller "FC+" to the stack "FC+" and controller "FC-" to stack "FC-&Load-". And also connect the grounding cable to the stack. The finished connection is shown in 2E.

2A

2B

2C

2D

2E

Note: After the fuel cell stack is finished using, disconnect the grounding cable from the stack. Every time you operate the stack, connect the grounding cable to it.

STEP 3:

Connect the controller to a stable power supply through the “DC 24V” connectors (3A), and the voltage of the power supply should be between 24V and 25V.

3A

STEP 4:

Lay the Hydrogen supply valve and the purge valve at the side of blowers in case stack damage caused by the Hydrogen purge.

STEP 5:

Keep the SCU (Short Circuit Unit) switch ON at “-” for usual use.

Warning: *Some home appliances may not be suitable for this activation process. It may cause damaging. You can shut off the short circuit by switching it to "O", but it will cause at least 20% performance loss.*

5A

STEP 6:

Connect the Hydrogen supply valve to the stack. The Hydrogen supply valve will prevent damage from the Hydrogen while the stack is off. Pay attention to the direction of the connection of the Hydrogen supply valve. ***The letter "IN" refers to the hydrogen input.*** The finished connection is shown in 6E.

WARNING:

The tube between the hydrogen pressure regulator and the fuel cell gas input is required to be less than 30cm.The inner diameter of the tube is required to be more than 3mm. The input pressure to the stack is required to be 0.45-0.55Bar.

6A

6B

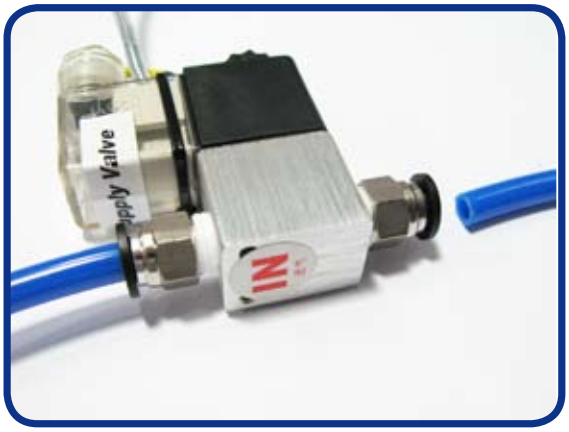

6C

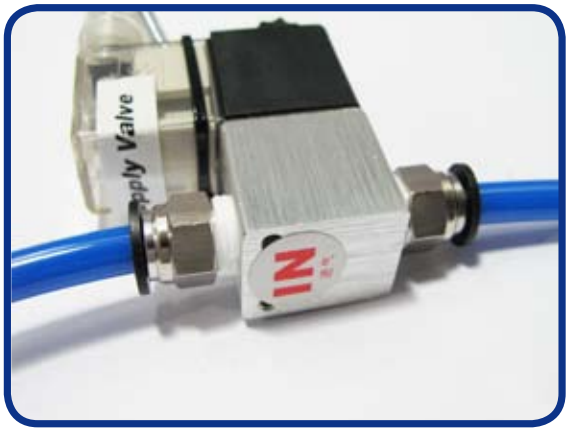

6D

6E

STEP 7:

Connect the stack to the purge valve. ***The letter "IN" refers to the hydrogen input.*** The finished connection is shown in 7D. Keep the output of the purge valve to a place away from the stack in case of the damage caused by purged hydrogen. See the pictures below.

7A

7B

7C

7D

Note: The tube between stack output and purging valve is required to be less than 20cm. The tube connected to the purging valve output is required to be less than 30cm. The inner diameter of the tube is required to be more than 3mm.

STEP 8:

Check all the connection first and connect the load to the system as shown in 8A. Load + is connected to “load+” of the controller, load – connected to the “FC- and load –” of the stack.

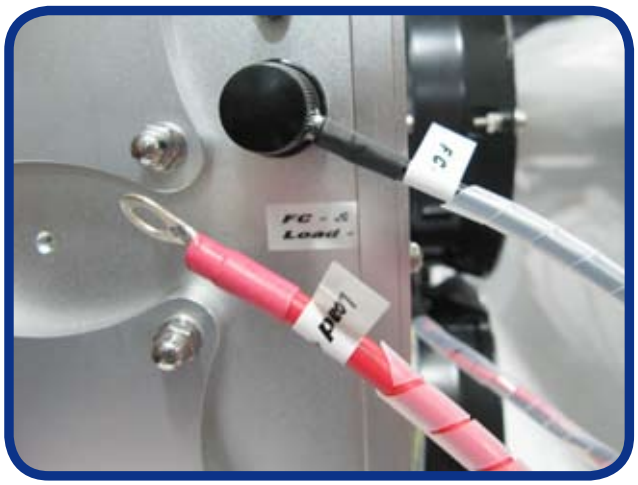

8A

STEP 9:

Connect LCD to the controller as shown in 9A. Provide hydrogen and turn on external power supply, then press the ON/OFF(9B) switch for more than 2 seconds to start the system. If you want to switch off the system, press the ON/OFF(9B) switch for 2 seconds.

9B

9A

STEP 10: Check the following steps before starting the system:

1. The connection between hydrogen pressure and hydrogen supply valve.
2. The connection between hydrogen supply valve and the stack input.
3. The connection between stack output and purging valve.
4. The output tube of the purging valve is kept away from the stack.
5. The connections between stack and controller.
6. The input hydrogen pressure is 0.45-0.55Bar.
7. The external power supply is 24V(±1V), 8A-12A.
8. The load is below 5000W.

The System is now setup and ready to be used.

6. Notes for the set-up

Note: The pictures below are only for reference.

Stack should be placed like this position.

The voltage of external power supply is 24V(±1V) for 5000W, the current range is different based on the different stack.

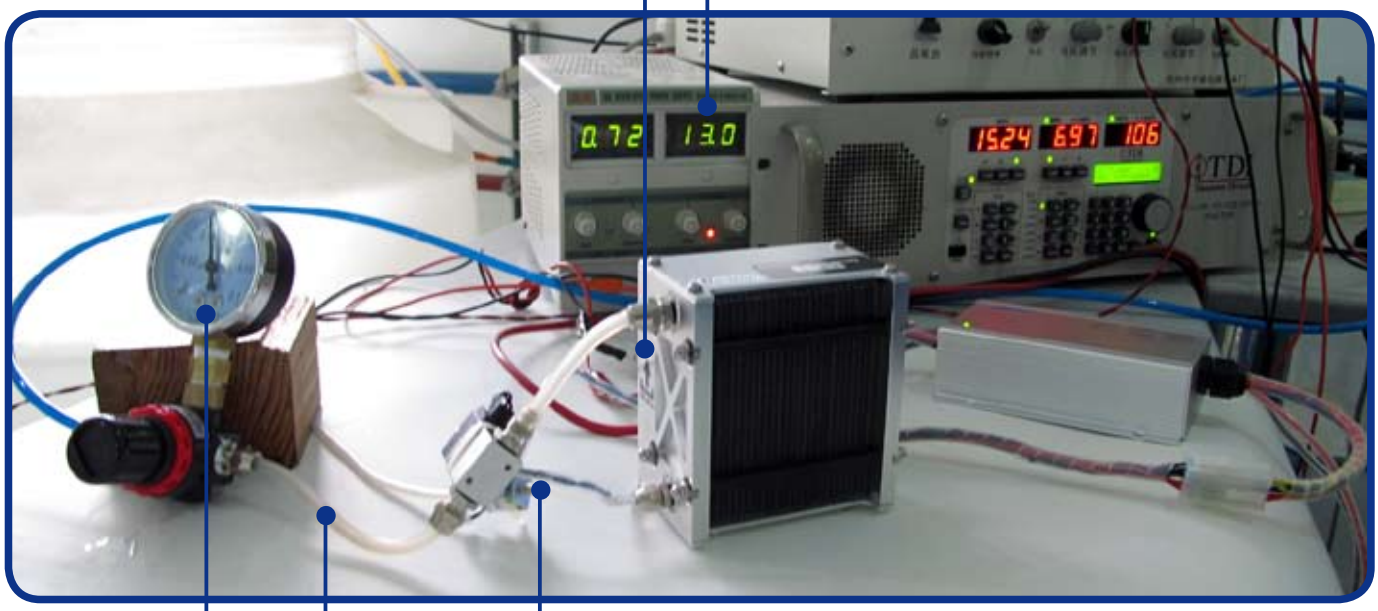

The tube is required to be less than 20cm between stack output and purging valve. The tube connected to the purging valve output is required to be less than 30cm. The inner diameter of the tube is required to be more than 3mm.

Warning: The tube between the hydrogen pressure regulator and the fuel cell gas input is required to be less than 30cm.

The pressure of the hydrogen is between 0.45--0.55Bar.

The load connecter, load+, is connected to the "load +"in the controller. The load- is connected to "FC- & Load-" in the stack.

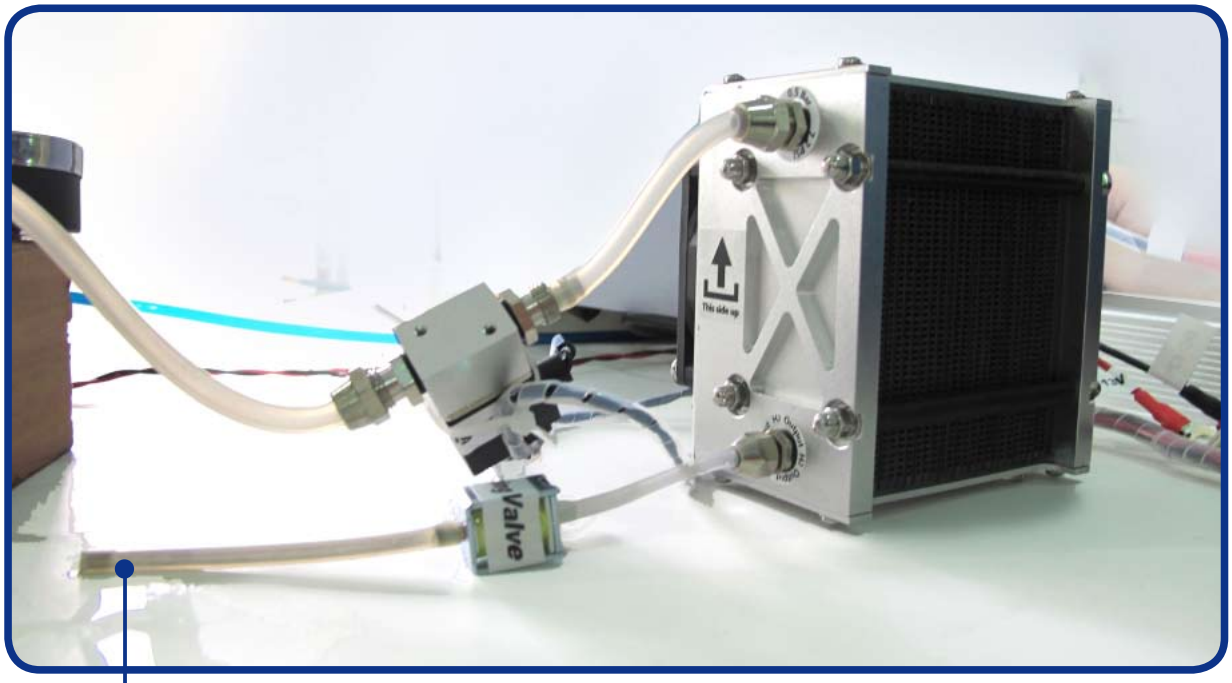

The outlet of the purge valve should be far away from the stack. Don't let the hydrogen from purge valve flow back to the stack, otherwise it would damage the stack.

Note: The tube between stack output and purging valve is required to be less than 20cm. The tube connected to the purging valve output is required to be less than 30cm. The inner diameter of the tube is required to be more than 3mm.

7. System setup diagram

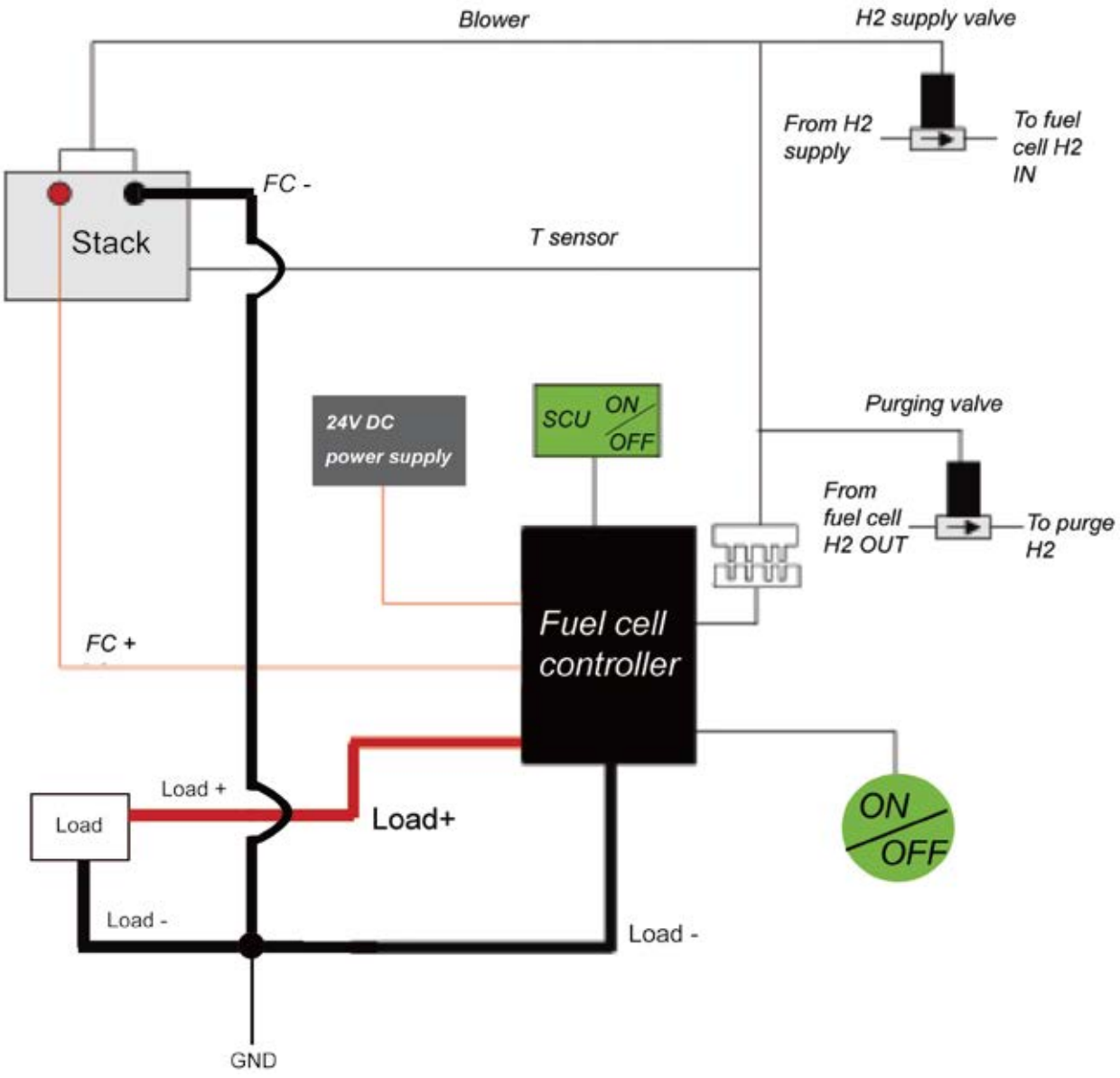

SCU: Short Circuit Unit
GND: Grounding

8. Polarization curves

Performance characteristics of the stack are presented. All performance data is given for baseline operating conditions, defined at sea-level and room ambient temperature.

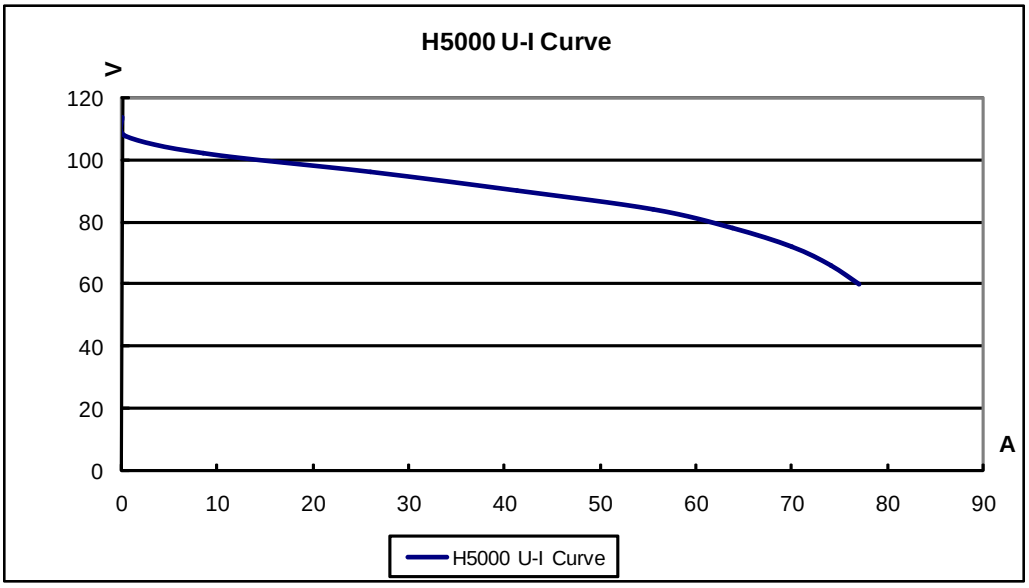

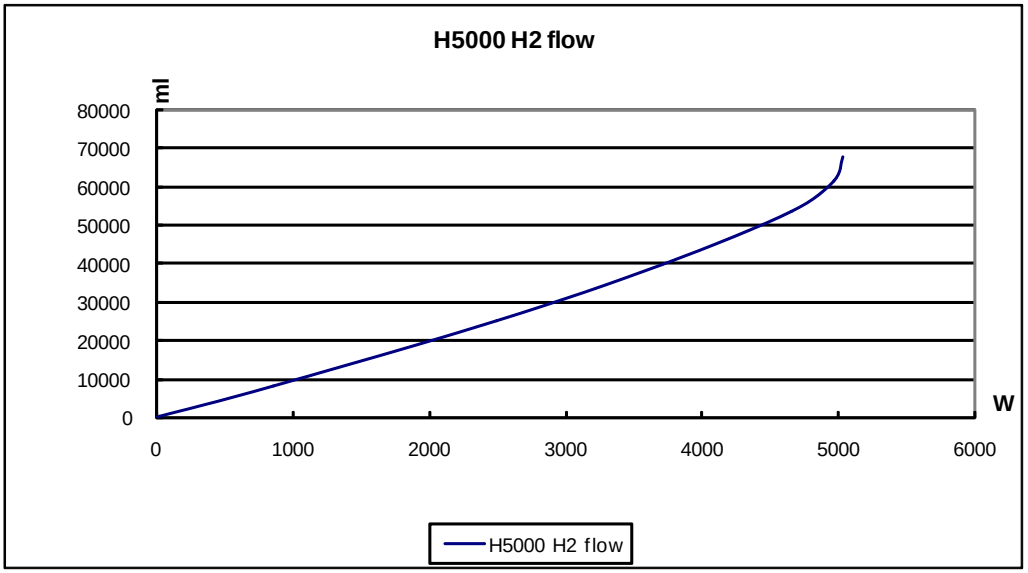

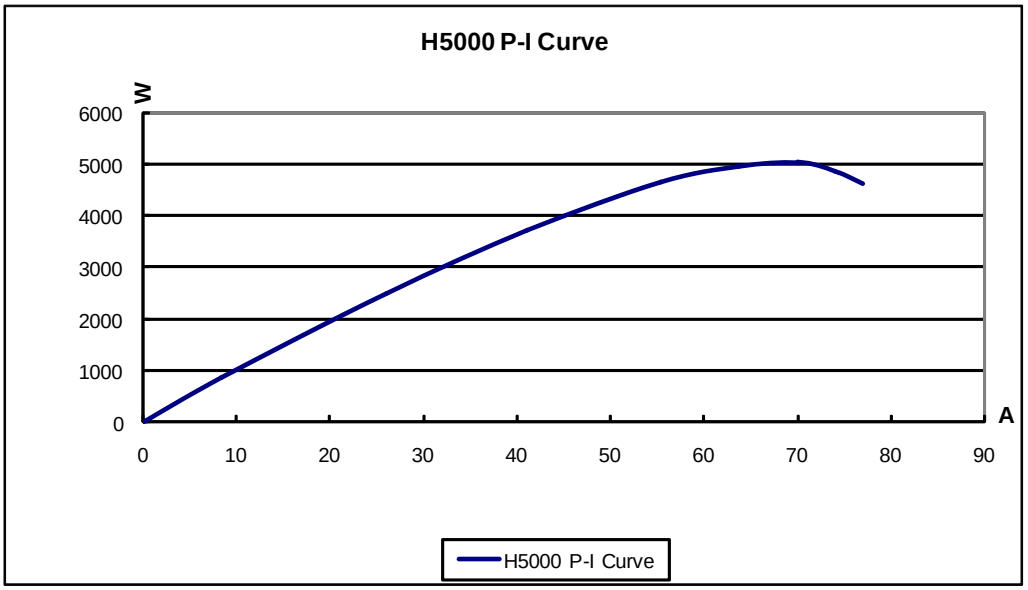

9. Operating instructions

STARTUP PROCEDURE

Make sure both the stack and the ambient temperature are less than 45℃. Otherwise the system will not start up successfully.
Hold the ON/OFF button down for 2 seconds and then release it to start the system; you will hear one beep, which means the system has started.

RUNNING PROCEDURE

After system has started, depending on your setup and application you can change your load to get the power you need within the specified power range for this fuel cell.

Don’t connect up a load that will demand power more than 5000W which can permanently damage the fuel cell.

During the operation, monitor the Hydrogen flow and pressure to consistently supply hydrogen at 0.45-0.55Bar.

Monitor the voltage of the external power is 24V(±1V).

Direct the outlet tubing of the purge valve away the fuel cell. Do not let the purged hydrogen go back towards the fuel cell stack, it will damage the fuel cell.

Pay attention to the purge, take care of the performance during the purge, If after each purge, the performance is increased about 10%, it means you need to increase the pressure of hydrogen a small amount. The fuel cell is flooding and so you need to use the pressure to push extra water out.

During the operation, you need to keep the SCU ON at "-", it will condition the fuel cell for rated power and keep it conditioned for long performance lifetimes.

- Short circuit will happen every 10 seconds and last for 100ms everytime.
- If the load does not operate well with the short circuit on we recommend that you run the fuel cell for 10 minutes prior to switching the load on.
- There will be a slight decrease in the power provided to the load with the short circuit off.

SHUTDOWN PROCEDURE

To shut down the fuel cell system down, please follow these steps:

1. Turn off the load.

2. Hold the ON/OFF button down for 2 seconds to stop the system, you will hear one long beep, which means the system is shutting down.

Note: When you turn off the on/off switch connected to the control box at the temperature of the fuel cell stack higher than 45˚C the stack will not stop working immediately. Only when the stack temperature goes down below 45˚C, the whole system will stop operation in order to protect the stack. So in order to make it work well, the fuel cell stack must be maintained lower than 45˚C before operate the on/off switch.

3. Turn the hydrogen supply off.
4. Disconnect the hydrogen supply tube from the hydrogen inlets as shown in the picture below.

WARNING:

Disconnect the hydrogen tube from the hydrogen inlets immediately after the fuel cell stack is shut down. Since hydrogen gas can leak into the fuel cell and destroy the stack.

If the fuel cell is not in use, please follow these final steps.

Disconnect the external power supply from the controller.
Completely disconnect the fuel cell system from the load.
Completely disconnect the fuel cell system from the controller.

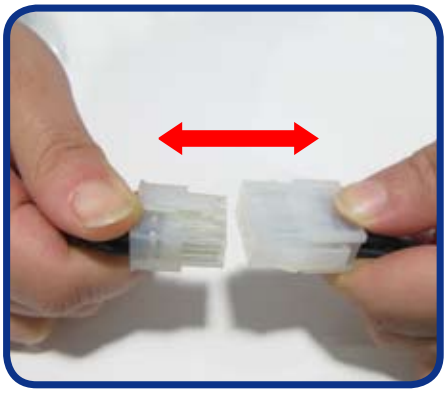

Let the fuel cell cool down before placing it into an air tight container. This will help maintaining its performance particularly during long periods of storage.

10. Storage and Re-Use

When finished operating the stack, place it in an enclosed area for storage to keep the stack from getting too dry. The stack should be stored at room temperature.

If the stack is un-used for a long period of time (more than 4 weeks) and it's performance goes down 50% to the rated power at 72V after 30 minutes operation, we recommend do the following steps.

Note: Generally, injecting water into the stack it is not recommended. Only if the performance of the stack decreases 50% is it recommended to inject water into the stack to activate the stack before operation.

Rejuvenate by injecting water into the stack:

1. Connect a tube to the “H2 input” port.
2. Fill a syringe (not provided) with distilled or purified water (see picture A). Make sure there is no air in the syringe. And then connect it to the tube.
3. Inject distilled or purified water into the stack until you see water coming out of the “H2 output” ports. Keep the water inside the stack for about 2 minutes. Now disconnect the syringe with the tube.
4. Purged water out of the stack.
   Connect the H2 supply (0.45-0.55Bar) to the stack through the tube without a load attached (see picture B), to purge water out of the stack as much as possible (i.e. letting hydrogen flow through the stack to remove water and other contaminants) (see picture C). Using the fuel cell stack with too much water inside can irreparably damage it!

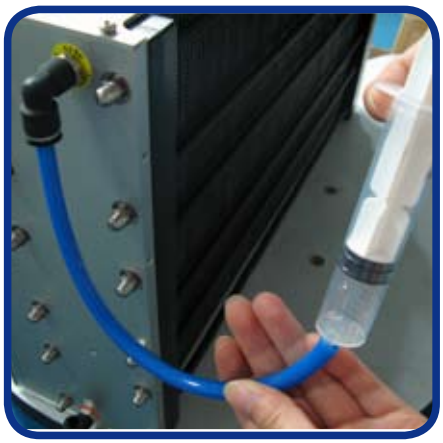

A

B

C

WARNING:

1. Make sure the hydrogen supply pressure is 0.45-0.55Bar.

2. Please make sure you have purged the water out of the stack as much as possible before use if you injected water into the stack. Using the fuel cell stack with too much water inside can irreparably damage it!

3. The tube between the hydrogen pressure regulator and the fuel cell gas input is required to be less than 30cm.

11. Trouble Shooting

If the stack is not used for a long time (months), it will take a little time to get the rated power, it needs 5-30 minutes.
Only it's performance goes down 50% to the rated power at 72V after 30 minutes operation we recommend to inject water into the stack to activate the stack before operation. Please see the detailed information in Storage and Re-Use.

If the system shuts down by itself check the following details:

1. Make sure you have connected all wires according to the System Setup Diagram.
2. Make sure the external power supply is 24V(±1V), 8A-12A.
3. Make sure the input hydrogen pressure is 0.45-0.55Bar.
4. Make sure the load is below 5000W, because the controller will protect the stack from drawing too much current.
5. Check whether the fuel cell temperature is below 65°C, the system will shut off if it is above 65°C.

Do not attempt, under any circumstance, to disassemble or inappropriately tamper with the fuel cell. There will be no returns, refunds or exchanges should disassembly or tampering occur. If you have questions or need help with regards to the fuel cell and its technology contact: support@horizonfuelcell.com

12. FAQ

What is the SCU?

This is the Short Circuit Unit, it helps to condition the fuel cell for long term good performance.

What is the Hydrogen pressure supplied to the fuel cell stack?

The pressure is required to be 0.45-0.55Bar.

What is the maintenance of the stacks?

1. When the stack finishes operation, disconnect the hydrogen input and output tube from the stack and also disconnect the power output. Use a tube to connect the hydrogen input to the hydrogen output of the stack.

2. Store the stack in ambient temperature and in a closed space. Keep it away from toxic gas, such as So2, H2S, Co.

3. Operate the stack for 2-3 hours every 2 weeks or at least one month in order to maintain the stability of the stack performance.

4. If the stack has not been used for more than 2 months, the stack power maybe get a little bit down when you use it again. We suggest at the beginning not to have full load to the stack, try to have half power for the starting. And then step by step increase to full load, try to increase 5% every 10 minutes. After this activation process, the stack can reach the rated power within 1-2 hours.

5. If the stack has not been used for more than 2 months and your load could be set to constant voltage, try to operate the stack under 0.6V/cell. Under this operation mode, the stack can reach the rated performance within 1-2 hours.

LAUNCHPOINT MOTORS

Launchpoint Technologies 6” Dual Halbach Air-core Motor

Rated 7 HP continuous output at 8400 rpm, 95% efficient

Parameter[1]	**Units**	**Value**
Max rated bus voltage	**Vdc**	120
Continuous Torque (Stall)	**N-m**	2
Continuous Torque @ Max rated speed	**N-m**	8
Continuous Current (Stall)	**A_{rms}**	8.5
Continuous Current @ Max rated speed[2]	**A_{rms}**	51
Max Rated Speed	**rpm**	8400
Torque Constant	**N-m/A_{rms}**	.17
Back EMF Constant (line-line, wye)	**V_{pk}/k_{rpm}**	14.6
Resistance (line-line, Wye terminated)[3]	**Ohm**	.176
Inductance (line-line, Wye terminated)	**uH**	3.8
Inertia	**kg-cm^2**	
Weight	**kg**	.72
Static Friction	**N-m**	.036
Drag torque at max rated speed	**N-m**	.095
Thermal Time Constant (stall/max rated speed)	**seconds**	523 / 6.2
Thermal Resistance (stall/max rated speed)	**Deg C/W**	14.6 / .18
Pole Pairs		25

[1] All parameters assume sinusoidal motor currents
[2] Coil at 150 C, 25 deg C ambient air
[3] Coil at 25 C

Predicted performance:

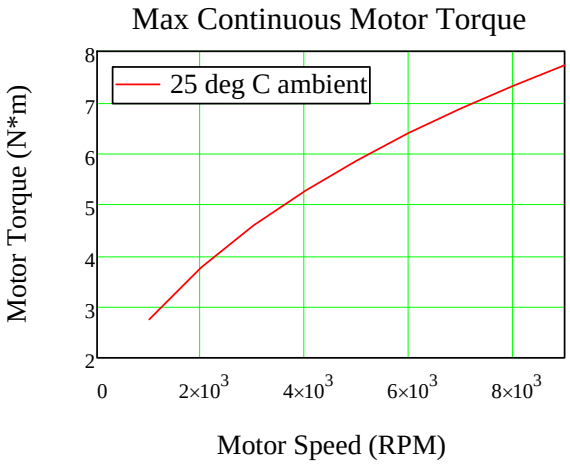

The Launchpoint Technologies Dual Halbach motor is air cooled with an integrated fan. Thus the allowable torque and current in the stator go up as the motor spins faster and has more available cooling. More torque would be available at low speeds if external cooling were added.

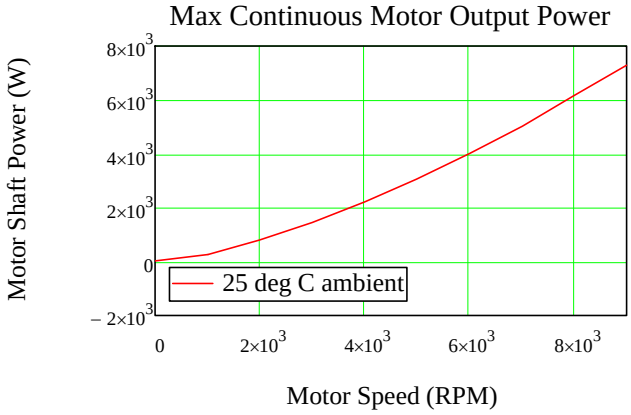

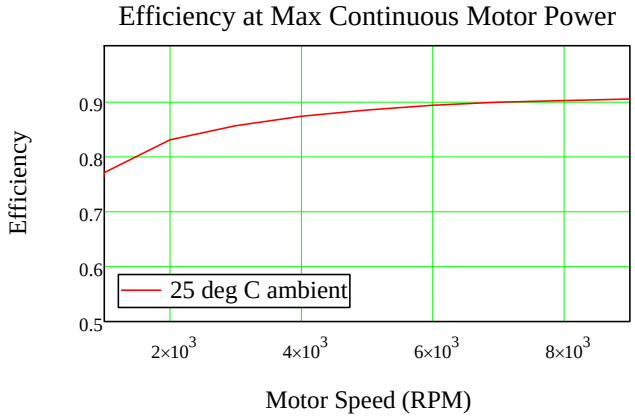

Measured Motor Loss Data

Experimental Data: